HIGH TEMPERATURE ULTRASONIC GAS FLOW SENSOR BASED ON LEAD FREE PIEZOELECTRIC MATERIAL

Dalibor Krsmanovic

Darwin College

University of Cambridge

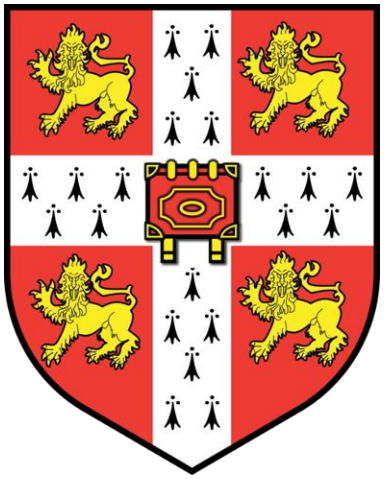

A dissertation submitted for the degree of Doctor of Philosophy at the University of Cambridge

November 2009

Academic Supervisor: Dr R. V. Kumar

Industrial Supervisor: W. Averdieck

Declaration of Originality

I am submitting this dissertation for the degree of Doctor of Philosophy at the University of Cambridge. The said thesis contains work I carried out between October 2006 and November 2009 at the Department of Materials Science and Metallurgy, University of Cambridge, under the academic supervision of Dr. R. V. Kumar. I state that, except where indicated, the work described is to the best of my knowledge, original and my own work. This dissertation does not exceed the word limit of 60,000 words.

Dalibor Krsmanovic
Darwin College, Cambridge

Abstract

The review of current technologies for measurement of gas velocity in stack flow applications is undertaken and it is shown that the ultrasonic time-of-flight method is the most suitable and offers a number of advantages over alternatives. Weakness of current piezoelectric based transducers are identified as the inability to operate at temperatures above 400 °C due to limitation of piezoelectric materials used, and a case for development of an alternative high temperature material is put forward.

A novel and highly enhanced, lead free piezoelectric material, suitable for continuous operation at temperatures above 400 °C has been engineered for ultrasonic gas velocity sensor applications. Structural modification of pure bismuth titanate ($Bi_4Ti_3O_{12}$) or BIT compound, through multi-doping at the Ti-site, has been found to enhance piezoelectric properties accompanied with a mild reduction in Curie temperature, T_c. Initially, compounds doped with tungsten and chromium were found to increase the piezoelectric coefficient (d_{33}) from around 5 pC N^{-1} in pure bismuth titanate, to above 20 pC N^{-1} in doped compounds. This increase is attributed to lower conductivity and improved poling conditions. Further increases in d_{33} (up to 35 pC N^{-1}) were then realised through controlled grain growth and reduction in conductivity for niobium, tantalum and antimony doped compounds. The Curie temperature of the material with best properties is found to be 667 °C, which is a slight reduction from 675 °C for pure bismuth titanate ceramic. The enhancements in modified bismuth titanate achieved in present work allow the material to be considered as suitable for high temperature ultrasonic transducer applications.

Integration of bismuth titanate material into a working high temperature transducer is then considered and the investigation of suitable, high temperature bonding method is undertaken. It is shown that reactivity of bismuth titanate with the titanium based fillers makes brazing unsuitable as a bonding method between piezo-ceramics and stainless steel. A novel assembly method, using liquid gallium as an electrically conductive bond, and a mechanical restraint for the piezo actuator is then presented as an alternative with the potential to reduce the negative effects of differences in thermal expansion coefficients between constituents of the transducer assembly.

Acknowledgements

I would like to thank my academic supervisor, Dr R. Vasant Kumar, for his guidance and support throughout the project. I would also like to thank my industrial supervisors Mr William Averdieck, who initiated, part-financed and facilitated this project through PCME ltd, and Dr Roger Millington for his support and advice.
A special thanks goes to Mr Jungang Hou and Mr Rahul Vaish for their help with evaluation of dielectric properties, synthesis and helpful general discussion.
I am extremely grateful to Dr Amir Shirzadi (Mr Bond) for his help and guidance with joining of materials, to Dr Carsten Schwandt for his kind help and direction around the labs, to Mr Robert Stern and Mr Kevin Roberts for help with preparation of experiments, to Davit Unitt, Mike Rigby and Bruce Greetham for helpful discussions.

I would also like to express my gratitude to Prof. Mike Reece and his team for kindly supporting and facilitating the SPS trials for enhancements of BIT at QMUL laboratories.

I would also like to thank EPSRC for providing funds for this project and continuing their support through EPSRC PhD plus funding made available to me in order to continue this research.

Special thanks goes to my wife Irene and children, Samuel and Natasha, for their ultimate understanding, support and encouragement.

Publications

J. Hou, Y. Qu, R. Vaish, D. Krsmanovic, and R.V. Kumar, *Effect of Sb Substitution on the Structural and Electrical Properties of Bi4Ti3−2xNbxTaxO12 Ceramics.* Journal of the American Ceramic Society, 2011:

J. Hou, Y. Qu, D. Krsmanovic, C. Ducati, D. Eder, and R.V. Kumar, *Hierarchical assemblies of bismuth titanate complex architectures and their visible-light photocatalytic activities.* Journal of Materials Chemistry, 2010. **20**:

J. Hou, Y. Qu, D. Krsmanovic, and R. Kumar, *Peroxide-based route assisted with inverse microemulsion process to well-dispersed $Bi_4Ti_3O_{12}$ nanocrystals.* Journal of Nanoparticle Research, 2010. **12**(5):

J. Hou, Y. Qu, R. Vaish, K.B.R. Varma, D. Krsmanovic, and R.V. Kumar, *Crystallographic Evolution, Dielectric, and Piezoelectric Properties of Bi4Ti3O12:W/Cr Ceramics.* Journal of the American Ceramic Society, 2010. **93**(5):

J. Hou, R. Vaish, Y. Qu, D. Krsmanovic, K.B.R. Varma, and R.V. Kumar, *Dielectric, pyroelectric and ferroelectric properties of Bi4Ti2.98Nb0.01Ta0.01O12 ceramics.* Materials Chemistry and Physics, 2010. **121**(1-2):

J. Hou, R. Vaish, Y. Qu, D. Krsmanovic, K.B.R. Varma, and R.V. Kumar, *Dielectric relaxation and electrical conductivity in Bi5NbO10 oxygen ion conductors prepared by a modified sol-gel process.* Journal of Power Sources, 2010. **195**(9):

J. Hou, R.V. Kumar, Y. Qu, and D. Krsmanovic, *Controlled synthesis of photoluminescent Bi4Ti3O12 nanoparticles from metal-organic polymeric precursor.* Journal of Nanoparticle Research, 2009:

J. Hou, R.V. Kumar, Y. Qu, and D. Krsmanovic, *B-site doping effect on electrical properties of Bi4Ti3-2xNbxTaxO12 ceramics.* Scripta Materialia, 2009. **61**(6):

J.G. Hou, R.V. Kumar, Y.F. Qu, and D. Krsmanovic, *Crystallization kinetics and densification of YAG nanoparticles from various chelating agents.* Materials Research Bulletin, 2009. **44**(8):

Table of Contents

Chapter 1 Introduction

The measurement of flue gas velocity in industrial chimney stacks presents a number of challenges to the technologies typically used in gas flow applications. Presence of extremes of environment, such as high temperature, large pressure variations, contamination from dust and chemical species and the presence of acids, makes successful measurement of gas velocity a very complex task. However, with more reliable solutions coming on the market, this is fast becoming a major growth area within a fairly mature industry of continuous emission monitoring (CEM) equipment. This growth is partly due to commercial drivers such as plant efficiency; however, public and legislative pressures play a very important role in imposing a range of measures to limit the environmental impact of industrial plant, introducing the need for a much better quality of volumetric flue gas analysis.

Increased social awareness of the environmental damage and its consequences for future generations caused by industry, is putting pressure on governments and international governing bodies to impose strict legislation to limit the emissions from industrial sources. Examples of such initiatives are the European Union Emissions Trading Scheme and the Acid Rain Program in the United States [1]. A number of such schemes are implemented around the world and cater for pollutants in gas, water or the solid phase. An example of local legislation is the Clean Air Act 1993 [2] in the United Kingdom. Generally, industrial plant are required to continuously monitor the mass flow rates of pollutants in exhaust flue gas against given limits, and to periodically report the readings to the administrative body. The limits are set appropriately low and the plant operator is forced to put in place measures to ensure that the set limits are not breached. As filtration and process technologies improve, the emission limits tend to fall, forcing demand for higher quality instrumentation, with an appropriate range of resolution. Mass flow in kilograms per hour is generally used as a principal measure of dust and grit within flue gas, but particulate continuous emissions monitoring (CEM) equipment more commonly measures concentration of

solids in $mg \cdot m^{-3}$. To convert concentration data into mass flow, the measurement of flue gas velocity is required, which highlights the requirement for suitable gas velocity instruments in all relevant applications.

Taking the operating environment inside the smoke stack into consideration, it is evident that measurement technologies such as thermal mass or pitot tubes are not suitable for continuous operation due to the requirement for the sensing elements to be in the main flow path of the contaminated flue gas. This makes the sensing head vulnerable to rapid deposition of particulates and hence deterioration in measurement accuracy and ultimate failure. Having said that, these technologies are successfully deployed in certain very low particulate level applications where there is no demand for a measurement which takes into account turbulent flow. The ultrasonic Time-of-Flight (TOF) gas velocity measurement method is emerging as a dominant technique typically deployed on industrial smoke stack applications. The main reason for this can be attributed to the general construction of TOF instruments, which will be discussed in the following chapter and their proven track record in immunity against contaminants in gas, liquid and solid form.

The main limitation of current ultrasonic technology is the low continuous operating temperature, which makes it unsuitable for applications beyond 250 °C without air purge cooling.

The most popular piezoelectric material used for manufacture of ultrasonic transducers is lead zirconate titanate or PZT. It has very good electromechanical properties but is compromised by having a relatively low Curie temperature (T_c). Various manufacturers have made attempts to improve the operating temperature range of their instruments by supplying purge air on the surfaces of the transducer in order to cool down the piezoelectric element, but this has obvious disadvantages as it is costly and it affects the performance of the instrument. Using alternative piezoelectric materials to PZT, such as lithium niobate and bismuth titanate, which have a higher T_c, has not proved popular or reliable due to the inherent low electromechanical and piezoelectric coefficients of such materials. There are

currently no suitable high temperature ultrasonic air transducers available for wetted[1] type gas flow applications that operate without air purge above 250°C.

The general aim of this research is to develop materials and assembly methods that will enable the subsequent design of a rugged ultrasonic transducer, able to operate at temperatures up to 400°C, without the air purge system. Bismuth titanate is identified as a good piezo-ceramic base material. It has recently generated significant scientific interest due to its high dielectric permittivity, high Curie temperature (T_c) and low dissipation factor. Development is focused on improving the piezoelectric properties of bismuth titanate by the addition of doping elements whilst retaining the high Curie temperature. For the transducer body, stainless steel 316L has proved reliable in the field over a number of years, particularly in the optical dust monitoring product range [3], and it is selected as the material of choice, having good abrasion resistance, desirable anti-corrosion properties and is cost effective for present application.

This thesis begins with a broad literature review of current gas flow measurement technologies, materials and devices being used within the CEM industry. The overview of piezoelectric materials is given in chapter 2 and is followed by a description of experimental methods utilised in present work as well as the detailed description of techniques used for manufacture of bismuth titanate ceramics.
Results and discussion on development of modified bismuth titanate is offered in Chapter 5, and the work is presented to emphasise the incremental enhancements achieved in various compositions. Chapter 6 is devoted to development of bonding methods suitable for high temperature transducer fabrication starting with description of experimental procedures, followed by results and discussion. The thesis ends with a conclusion and a suggestion for future work, taking into consideration EPSRC PhD Plus programme funding, made available to aid development of a functional high temperature transducer, based on lead free piezoelectric material.

[1] In this case, the transducer is in full contact with the flue gas rather then buffered or recessed.

Chapter 2 Flow Metering Methods and Technologies

2.1. CEM flow measurement

The history of the use of ultrasound goes back a long way. Clay potters and other craftsmen often used sound to gauge the quality of their finished work and Glen Wade [4] suggests that even though the ultrasound frequency range is beyond the range of human hearing, there are examples of humans being aware of it and using wolves for hunting, exploiting their acute hearing at ultrasound frequencies. Other animals use ultrasound for different purposes. Bats, dolphins and other species generate and detect high frequency acoustic waves to see and communicate, and this principle has been studied and applied in the ultrasonic technology used today. It is generally considered that ultrasound is any sound beyond the top range of human hearing i.e. over 20 kHz. Early experiments to measure the speed of sound in air date back to 1600s [5] and in water, experiments were conducted 200 years or so later. Given the nature, breadth and the timescales of the subject, it is more fitting to present the recent history of ultrasonics in terms of significant milestones - those which have marked significant developments in the technology.

The sinking of the Titanic in 1912 generated significant interest in developing the means for preventing that kind of catastrophe in the future. Several prominent scientific figures put forward proposals and literature suggesting the use of ultrasound sonar devices as a means of detection of underwater obstacles. However, it was a French scientist Paul Langevin who first implemented a practical device for making measurements using acoustic ultrasound transducers based on the vibration of piezoelectric materials. During World War I, Langevin realised that a reflected acoustic wave could be used for the detection of German submarines, and although

his device was not implemented during the war, the foundation was laid for the use of piezoelectric transducers in other measurement fields. In the period between the First and the Second World Wars, research into the use of ultrasonic technology for military purposes intensified. Underwater sonar was further developed not only for detection of submarines, but also for marine navigation. During the 1920s it was realised that acoustic attenuation in bulk material could be investigated using ultrasonic waves, and this became known as Non-Destructive-Testing or NDT. Russian scientist Sergei Y. Sokolov, often perceived as the father of NDT, suggested that by analyzing both the phase and the amplitude of the received echo signal, acoustic impedance mismatches caused by faults in the structure of the bulk material could be detected. This work was a precursor for the post-WWII development of ultrasound imaging in medicine, being led mainly in United States and Japan independently.

It was in the late 1940s and early 1950s that the idea of measuring the flow of liquids through a pipe was developed. In 1952, Kalmus [6] filed an application for a patent regarding an apparatus for the measurement of fluid flow in a pipe by means of a contra-propagating ultrasonic signal, essentially describing the operation of a modern time-of-flight measurement based system. Interestingly, Kalmus also made a number of statements regarding the prior art, which gave a good insight into the challenges faced by the process engineers of that time, in terms of the measurement of velocity in custody transfer applications for example, using measurement technologies other than ultrasonic. Two years prior to Kalmus' application for a patent, Ora G. Blocher also submitted an application for a patent on an apparatus for the measurement of fluid flow [7]. This patent also made a loose claim that the apparatus was able to measure the flow of gas as well as that of fluid. Both of the above patents were granted in 1955, which is generally perceived as the birth year of the modern ultrasonic flow measurement system. In 1955 Jack Kritz made an application for a patent on an electroacoustic flowmeter [8], which shows a diagram of the ultrasonic measurement system commonly seen on instruments employed today. A significant paper on the history of ultrasonic flow meters was published by an engineer and the veteran of ultrasonic flow meter development, Lawrence C. Lynnworth [9]. Lynnworth noted that, following the initial success of so called wetted transducer type instruments, practical clamp-on instruments started to appear from 1964 and these were aimed at

measuring water flow in large pipes and open channels. Current trends for high accuracy applications are satisfied by flow meters with multiple ultrasonic measurement paths, typically supplied as a spool piece and used in custody transfer applications such as natural gas pipelines. With respect to flow metering in general, a substantial and key body of work by Richard W. Miller [10] has been published on the subject of different flow metering technologies. The author gives a very detailed mathematical overview of the relevant properties and challenges presented by flow media such as liquid or gas, to the flow measurement efforts. This is also reinforced by a more practical review of the field by Roger C. Baker [11], which gives an insight into general issues involving the use and installation of flow measurement instruments. These early concepts have crystallised the fundamentals of ultrasonic flow metering and over the past 6 decades or so, improvements in digital processing technology as well as the availability of advanced materials have contributed to the increasing success of ultrasonics in this field. For gas velocity measurements in large diameter smoke stacks in particular, literature identifies a small choice of technologies that are suitable [1, 12], and in broad terms they can be described as the traverse pitot tube, differential pressure (sometimes in the form of the pitot tube), thermal mass, optical scintillation and ultrasonic time-of-flight methods. That said, pitot tube, thermal mass and ultrasonic methods are the most common and will be discussed further.

2.1.1. The Pitot Tube Method

Flue gas velocity measurements have traditionally been conducted using traverse pitot tube measurements [12], which are typically averaged by sampling at a number of positions depending on the diameter and shape of the flue duct, to remove the effects of turbulence. This measurement technique is still dominant for routine and non-continuous measurements such as iso-kinetic sampling[2]. It is relatively inexpensive, simple to set up and the user has a good choice of vendors for suitable equipment. Figure 2-1 shows a typical segmentation of square and round duct cross-sections, as described by Hawksley et al. [12]. The number of sampling points is increased with larger cross-sections and where the required accuracy is higher.

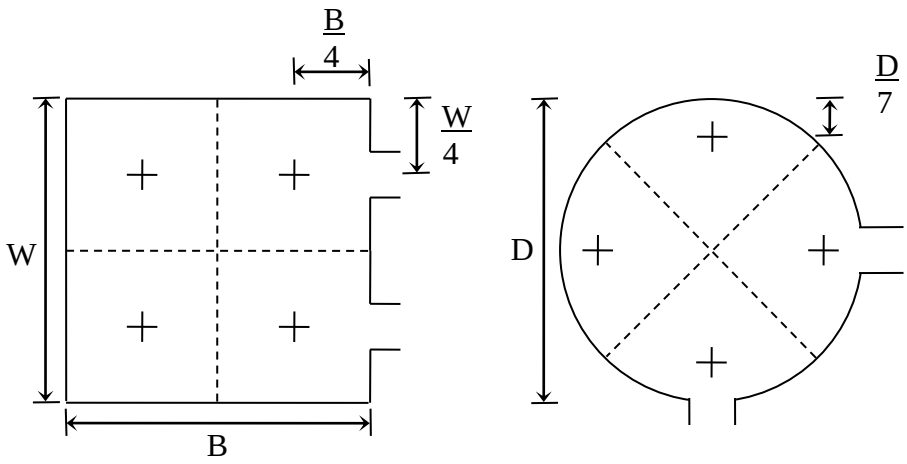

Figure 2-1 Typical segmentation of the flue duct cross-section into number of sampling points during isokinetic sampling tests [12]. The number of sampling points can be increased for larger cross section ducts in order to account for variations in flow velocity and turbulence.

[2] A standard method for collecting airborne particles where the sampling is occurring at the speed and in the direction of the gas stream just ahead of the sampling port. It is typically used to periodically verify emission levels and calibration for regulatory purposes.

However, this type of technology is less commonly used for the continuous measurement of flow. The main limitation of the pitot tube method for continuous flow monitoring is that it is inherently a single point velocity sensor [13], and it was recognised very early on that the flow pattern inside the duct is seldom uniform and that taking a single point measurement does not provide for good accuracy in turbulent flows. Furthermore, the pressure ports tend to block with any solid contaminants that may be present in the flue gas. Miller [10] points out that pitot tubes are rarely used in long term industrial applications because of vibrations, the delicate nature of the tube's construction and the fact that a number of points need to be measured in order to achieve adequate accuracy. However, multiport or averaging pitots are used frequently, particularly in clean gas applications. An early example of an averaging pitot tube is given in a US patent 1,250,238 [14]. The inventor identifies the detrimental influence of flow gradient on the average velocity measurement, and applies a weighted mean calculation to pressure measurements by paired sets of ports, related to different diameters of the cross section.

Figure 2-2 shows the measurement principle of the averaging pitot tube. A set of pressure sampling ports are facing into the flow, and are measuring total pressure; another set of pressure sampling ports are facing away from the flow, measuring the static pressure component. The equation for converting the differential pressure from the pitot measurement into the actual velocity is the Bernoulli equation.

$$p_t = p_s + \frac{\rho V^2}{2} \qquad \textbf{Eq.2-1} \text{ [12]}$$

Where p_t is the total pressure (dynamic component), p_s is the static pressure, ρ is the gas density and V is the velocity. Rearranging the equation for velocity;

$$V = \sqrt{2 \times \frac{p_t - p_s}{\rho}} \qquad \textbf{Eq. 2-2}$$

Currently, there are several vendors on the market offering averaging pitot tube solutions for gas velocity measurement in large diameter stacks. Some improvements over the years have been implemented, particularly with respect to the profile of the

probe such that it causes less turbulence in the stream flow and therefore allows for much more stable pressure measurement. However, the fundamental problem of probe contamination in applications where effluent gas carries solid or semi-solid particles still remains.

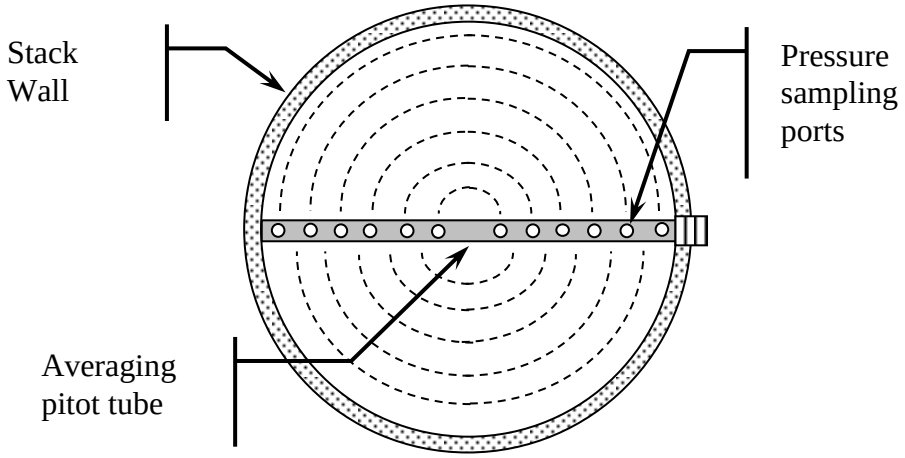

Figure 2-2 Typical averaging pitot tube installation (looking parallel to the flow direction and along the stack). A double skinned tube is placed across the full diameter of the stack. The outer bore of the tube is connected to the holes facing the flow, and the inner bore is connected to the holes facing away from the flow. With this arrangement it is possible to measure the total pressure due to the flow and to use Bernoulli's equation to calculate the actual gas velocity.

2.1.2. The Thermal Mass Method

Due to their construction and operating principles, thermal mass flow meters typically suffer from the same disadvantages as pitot tube type meters. There are two main categories of thermal mass flow meters; capillary and insertion. Both types are commonly used for gas flow metering, although in flue stack applications, only insertion type flow meters (ITFM) are found. Figure 2-3 shows the measurement principle of simplified ITFM. The heater is typically a resistive winding, the temperature of which is closely controlled using a local temperature sensor as feedback. The heat from the winding is transferred into the surrounding gas volume and if there is gas flow, some of the heat will be transferred downstream to the second temperature sensor. The two temperature measurements are then used to deduce the gas velocity and hence mass flow using mass flow equation;

$$q_m = \frac{Q_h}{K \times C_p \times \Delta T} \qquad \textbf{Eq. 2-3 [11]}$$

where q_m is the calculated mass flow rate in $kg \cdot s^{-1}$, Q_h is the heating energy in $J \cdot s^{-1}$, K is a constant, C_p is the specific heat at constant pressure in Joules per kilogram Kelvin and ΔT is the differential temperature. The disadvantages of thermal mass flow meters are discussed at length by Baker [11] and Miller [10]. The response of the instrument to changes in flow velocity is typically slow due to the thermal inertia of the components and at very low flows, the effects of convection flow become very significant. The exposed heater and sensor probes are particularly vulnerable to contamination build up, resulting in the deterioration of measurement quality or complete instrument failure. Another disadvantage of the typical ITFM is that it provides a single point measurement; however, recent developments in this field have resulted in a sensor arrangement similar to that of averaging pitot tube [15]. Multi-point flow meters are commercially available for limited applications, improving their acceptance in the market, competing mainly with averaging pitot tube instruments [16]. However, the presence of contamination in stack flow applications makes this technology a difficult choice for the user.

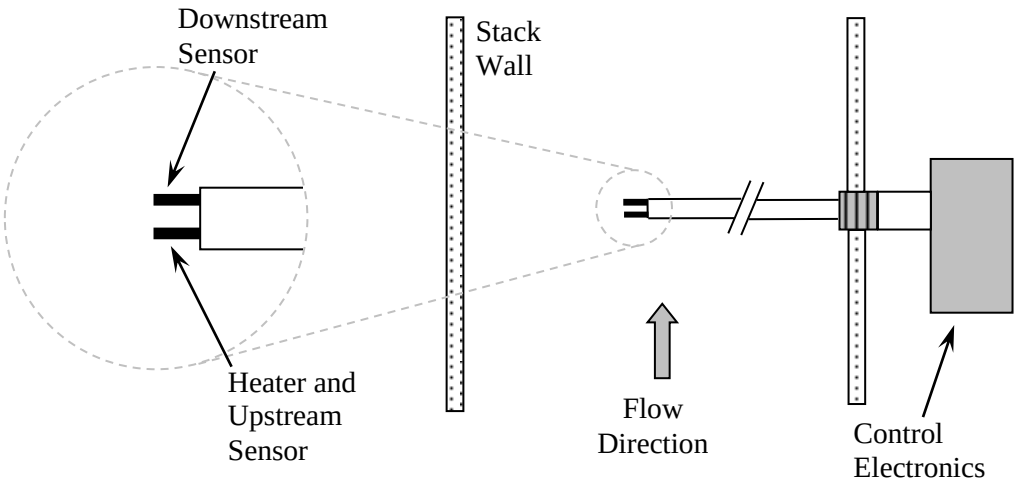

Figure 2-3 An insertion type thermal mass flowmeter in a stack flow application. The diagram shows the heater and sensor arrangement typically found on commercially available instruments.

2.1.3. The Ultrasonic Method

The ultrasonic flow meter is the most common type of instrument currently deployed in stack flow applications [1]. A number of vendors on the market offer ultrasonic solutions which do not suffer from the issues identified with pitot and thermal mass flow meters.

During the period between 2002 and 2008, the size of the ultrasonic flow meter market has almost doubled from $255 to $440 million [17], which demonstrates the pace of acceptance of this technology. The ultrasonic flow measurement principle has been successfully applied in liquid flow applications for many years, and is recently showing a stronger presence in the gas flow market. This is particularly the case in the so called 'custody transfer' market, measuring natural gas or other process gasses.

For smoke stack gas flows, instruments are available in three main topologies; insertion probe, clamp-on and cross-stack. These can be further defined into single point, line average and area average measurement methods, aimed to address different flow conditions in the stack. Flow conditions in a smoke stack are seldom constant across the diameter, which introduces a significant amount of error for a single point measurement. A line average measurement offers a significant improvement in accuracy, as it removes some of the effect of swirl or turbulence in the velocity profile, moving from the stack wall towards the centre. However, a cross-stack arrangement with several measurement paths, takes into account multi-dimensional real time changes in the flow profile, which can significantly affect the measured gas flow.

One way to visualise the effects of turbulence is given by Down and Lehr [1], where the stack is capped with a cyclone trapped inside. Due to swirl, the single path line average instrument may still detect flow even though no gas is exiting the stack. In this case, a multipath instrument will produce a superior measurement. Figure 2-4 shows a typical ultrasonic insertion gas velocity probe.

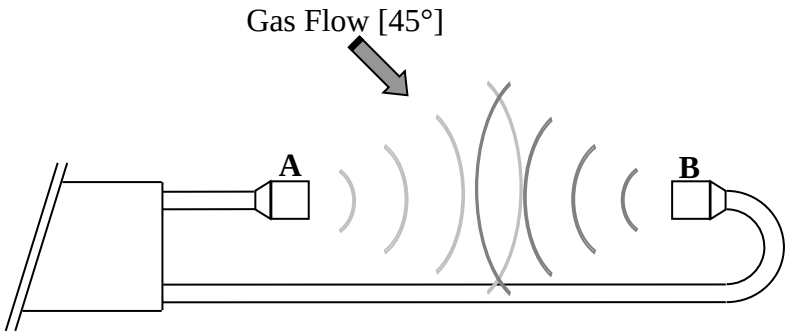

Figure 2-4 Typical construction for an ultrasonic insertion gas velocity probe head. Both transceivers, A and B, are able to transmit and receive ultrasonic pressure waves

This probe has a fixed distance between the two transducers (A and B), and offers a big advantage in that the installation can be carried out from a single measurement port, mounted at a 45° angle to the direction of flow. As will be shown later, using a single port is important to the end user, since it offers significant cost savings in

comparison to the cross-stack solution, both in terms of installation and the need for regular maintenance. However, that is not to say that this type of instrument is suitable for all applications.

As can be seen from the diagram in Figure 2-4, the transducers are typically in full contact with the flue gas, and in this case they are referred to as 'wetted transducers'. This means that they are exposed to fluctuations in flue gas temperatures. For low Curie temperature lead zirconium titanate based transducers, this has particular implications since a large number of stacks contain flue gases at 120 °C and above. Furthermore, field experience with triboelectric dust concentration instruments (PCME Ltd) suggests that the probe construction such as that shown in Figure 2-4 is likely to experience contamination issues, although this is dependent on the type of dust or grit and also the moisture content in the flue.

Another significant point to note about this type of instrument is that the fixed distance between transducers is usually relatively small; typically 300 to 500 mm. The distance has to be kept short to avoid the influence of vibration, which causes a decrease in signal to noise ratio. On large diameter stacks of perhaps 1.5 m or more, this method almost equates to a single point measurement, typical of pitot tube or thermal mass flow methods; this renders the insertion velocity probe unsuitable. However, these instruments are available on the market and clearly find their use in clean, low temperature and small diameter stacks.

Clamp-on flow meters for gases have been available since late 1960s [18] and there are several vendors on the market offering solutions for custody transfer applications in particular. The installation is generally non-invasive, which is important on high pressure lines for example, and transducers can be kept cool and clean, increasing reliability and reducing the maintenance burden on the end user. Non-wetted transducer design, typically found on clamp-on flow meters, is discussed extensively in the literature [10, 11, 19-21]. It is highlighted that this type of transducer configuration particularly suffers from poor acoustic coupling through the duct lining and poor signal to noise ratio. Figures of 3 % measurement uncertainty are common for clamp-on products in liquids, although values as poor as 5 to 10 % have been reported [11]. It is apparent from the design, that the quality of installation for clamp-

on flowmeters is critical to achieving optimum accuracy, whilst the on-going maintenance effort has to be focused on keeping the transducer interfaces in prime condition. Market literature supports this statement [22, 23], and for this type of gas flow metering product, there is a practical limit to the maximum diameter of the duct - up to 750 mm typically. This is an important limitation, since a large proportion of industrial smoke stacks fall outside this category.

Cross-stack flowmeters, which almost exclusively use wetted transducers [11], are the most common types of flowmeter currently used for stack gas flow applications, although less common and less accurate doppler velocity meters are available. Typically they employ the Time-of-Flight (TOF) or 'transit time' principle to measure speed of sound upstream and downstream, using the time delay caused by the gas flow, to calculate flow velocity. The measurement uncertainty for cross stack flowmeters is quoted as low as a fraction of a percent [11], and by averaging the sound velocity across the whole diameter of the stack, the effects of flow profile can be reduced.

It is interesting to note that most commercially available products utilise wetted transducer topology, allowing for high signal to noise ratio, even though these products are more vulnerable to thermal fluctuations and contaminants. However, transducers are usually recessed into the sampling port so as not to directly interfere with the gas flow. In this arrangement, it is common for transducers to be purged with clean instrument air to avoid contamination build up and to provide a thermal buffer around the transducer. Without purge air, operating in flue gas temperatures of 200 °C or so is common, and a significant proportion of the market is covered by such instruments. With purge air however, flue gas temperatures of up to 450 °C can be tolerated.

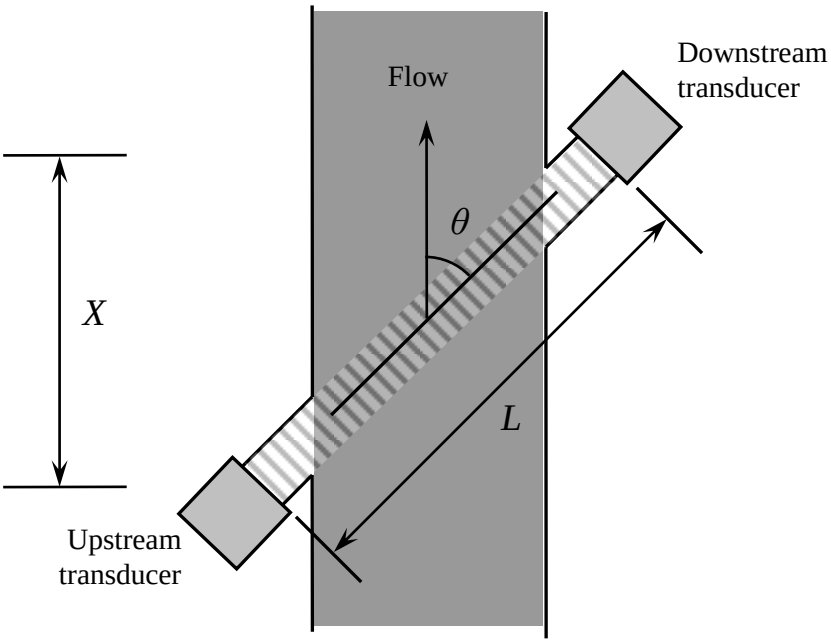

Figure 2-5 Ultrasonic, cross-stack gas velocity monitor installation topology. Two transceiver heads are positioned on opposite sides of the stack and at $\theta = 45°$ angle to the direction of flue gas flow and at distance L from each other. Contrapropagating ultrasonic bursts are transmitted and received in sequence by the two transducers, the electronics evaluates the Time-of-Flight difference caused by the flow.

The measurement principle can be better explained using Figure 2-5, where gas flow velocity *V* can be calculated by;

$$\textbf{Upstream}\ t_{up} = \frac{d \cdot Cosec\theta}{C + Vf \cdot Cos\theta}\ ;\ t_{dn} = \frac{d \cdot Cosec\theta}{C - Vf \cdot Cos\theta}\ \textbf{Downstream}$$

$$t_{up} \cdot (C + Vf \cdot Cos\theta) = d \cdot Cosec\theta \quad ; \quad t_{dn} \cdot (C - Vf \cdot Cos\theta) = d \cdot Cosec\theta$$

$$C + Vf \cdot Cos\theta = \frac{d \cdot Cosec\theta}{t_{up}} \quad ; \quad C - Vf \cdot Cos\theta = \frac{d \cdot Cosec\theta}{t_{dn}}$$

$$C - C = 0\ ;\ Vf \cdot Cos\theta - (-Vf \cdot Cos\theta) = 2Vf \cdot Cos\theta$$

$$\frac{d \cdot Cosec\theta}{t_{up}} - \frac{d \cdot Cosec\theta}{t_{dn}} = \frac{d}{Sin\theta} \cdot \frac{1}{t_{up}} - \frac{d}{Sin\theta} \cdot \frac{1}{t_{dn}} = \frac{d}{Sin\theta}\left(\frac{1}{t_{up}} - \frac{1}{t_{dn}}\right) = \frac{d}{Sin\theta} \cdot \frac{t_{dn} - t_{up}}{t_{up} \cdot t_{dn}}$$

$$= \frac{d}{Sin\theta} \cdot \frac{\Delta t}{t_{up} \cdot t_{dn}} \qquad \therefore\ 2Vf \cdot Cos\theta = \frac{d}{Sin\theta} \cdot \frac{\Delta t}{t_{up} \cdot t_{dn}}\ ;$$

$$Vf = \frac{1}{2} \cdot \frac{d}{Sin\theta \cdot Cos\theta} \cdot \frac{\Delta t}{t_{up} \cdot t_{dn}} = \frac{1}{2} \cdot \left(d \cdot \frac{L}{d} \cdot \frac{L}{X}\right) \cdot \frac{\Delta t}{t_{up} \cdot t_{dn}} = \boldsymbol{\frac{L^2 \cdot \Delta t}{2 \cdot X \cdot t_{up} \cdot t_{dn}}}$$

Eq. 2-4 [11]

Where *L* is the line distance between transducer faces, *X* is the flow-axial distance between transducers, *d* is the stack diameter, *c* is the sound velocity, θ is the installation angle, *V* is the gas velocity and t_{up} and t_{dn} are upstream and downstream transit times respectively. The evaluation of transit-time across the path length has the effect of averaging out non-linear components in the flow profile, which is a strong technical advantage of this technology. The installation geometry tends to be relatively constant with minimal thermal drift relative to path length and measurement angles, particularly on larger stacks. This results in a very stable measurement platform. According to Kocis and Figura [21], sound velocity in air can be approximated by;

$$c_{air} \approx \left(331.3 + \frac{T}{0.606\,^{\circ}\mathrm{C}}\right) \quad \mathrm{m \cdot s^{-1}} \qquad \textbf{Eq. 2-5 [21]}$$

Here, 331.3 $m \cdot s^{-1}$ is the speed of sound in air at 0 °C and *T* is the temperature in degrees Celsius.

A more general equation for the speed of sound in gas is given by Lynnworth [24];

$$c = \sqrt{\frac{\gamma \cdot R \cdot T}{M}} \quad \mathrm{m \cdot s^{-1}} \qquad \textbf{Eq. 2-6 [24]}$$

Where γ is the adiabatic index or heat capacity ratio, R is the ideal gas constant, T is the absolute temperature and M is the average molecular weight.

The limitations of TOF ultrasonic flowmeters are relatively few in comparison with the other technologies discussed earlier. Turbulence does present a problem in certain installations, but generally this can be resolved by installing a second measurement path over the same measurement volume.

One issue that needs to be mentioned concerns larger stacks, is the elevation distance between upstream and downstream ports, where the transceivers have to be installed at a 45° angle relative to the flow. On a 7m diameter stack, this equates to around 10m height difference, which means that two work platforms have to be installed. This adds significantly to the installation costs and is generally perceived as an unavoidable nuisance.

Transducer contamination is another factor which influences the instruments long term reliability. Build-up of contamination on the transducer face tends to have an attenuating effect on the transmitted signal due to acoustic impedance mismatch and the level of attenuation is relative to the level and type of the contamination. Figure 2-6 shows the effect of contamination (both inside and outside of the stack) on a typical insertion type instrument for measurement of particulate concentration (PCME Ltd), deployed at a wood and pulp plant for three months.

(a)

(b)

Figure 2-6 Levels of particulate contamination in certain applications can be extremely high. Image (a) shows a prototype instrument with contamination accumulated during 3 months of deployment at the wood and pulp plant. The image (b) shows the contamination build-up on a triboelectric dust concentration probe after 3 months of operation.

2.2. Ultrasonic Transducers for High Temperature

As the range of applications for the use of sound at ultrasonic frequencies grows, so does the choice of transducer types available on the market. Ultrasonic transducers, based on piezoelectric materials, have been in active development for several decades now, but have recently enjoyed a boost in popularity due to heavy uptake in automotive applications such as reverse parking sensors and distance measurement. This has had a knock-on effect in dramatically reducing the cost of devices as is often seen in high volume manufacture. The most common ultrasonic air transducers have PZT material as their core, which limits their operating temperature range to well below 200°C. However, the temperature limitation is not exclusively related to the piezoelectric material's Curie point and for successful design, all materials used in the construction of a device need to be considered. For example, at higher temperatures, transducer delamination ensues due to strains caused by differential thermal expansion. This leads to degradation of performance and ultimate device failure. Design techniques for high temperature, non-destructive testing (NDT) devices is discussed at length in various literature sources [25-30], however, there is a distinct shortage of references for high temperature air coupled transducers. A common solution for high temperature ultrasonic transducers is to mount the piezoelectric element onto the end of a buffer rod of appropriate acoustic properties. This kind of arrangement is typically suitable for non-destructive testing applications where acoustic impedance mismatch between the transducer and the material under test is small. Such a NDT device fabricated with the combination of PZT and $LiNbO_3$ as a composite piezoelectric material was successfully tested by Kobayashi et al. at temperatures > 800 °C [26]. The authors used the sol gel spray method to produce thick (> 40 μm) films directly onto stainless steel or titanium buffer rods. The effectiveness of buffer rods at high temperatures is discussed by Jen *et al.* [31] and it is shown that materials with low acoustic impedance can be successfully used to manufacture ultrasonic buffer rods up to 1 m in length. A similar approach was patented by Lynnworth [32] in 1988, for transmitting or receiving ultrasonic waves into solid materials. This approach was intended for use as a clamp-on transducer for

liquid flow metering. The schematic drawing of such a transducer is reproduced in Figure 2-7.

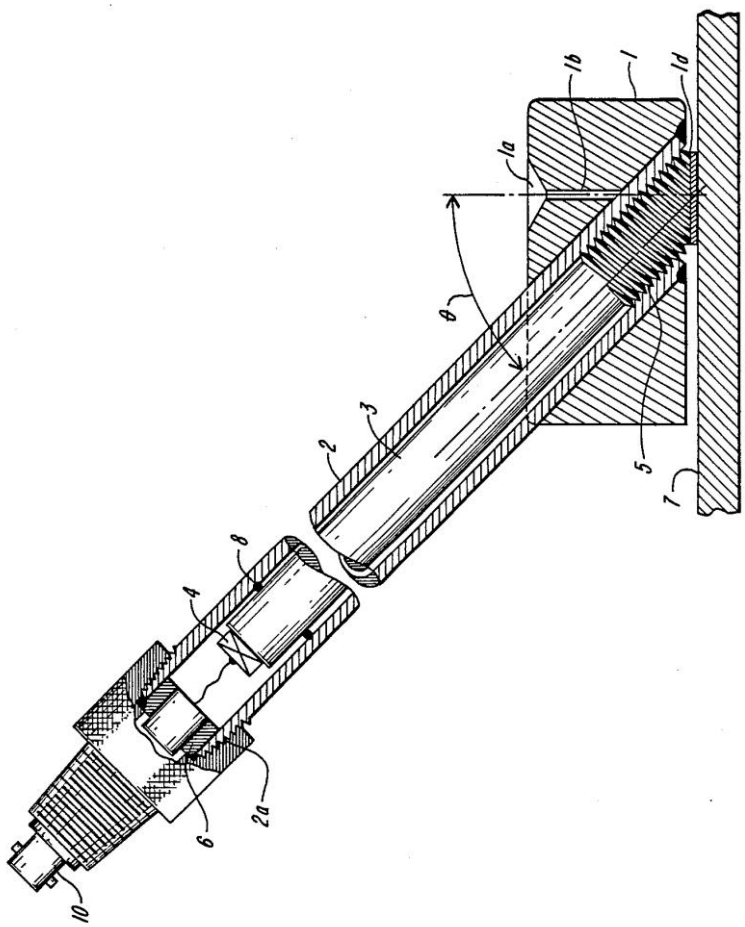

Figure 2-7 Image showing a buffered ultrasound transducer for clamp on liquid flow metering, as presented in a patent [32] by Lawrence C. Lynnworth in 1988. The image shows a buffer rod (3), piezoelectric element (4), pipe wall (7) and electrical connector (10) amongst other components.

An alternative method of high temperature NDT transducer assembly is discussed by Muto and Atsuta [33], where aluminium and magnesium alloy is used as a brazing filler for successfully joining lithium niobate and stainless steel, which also acts as a heat resistant electrode. The authors report successful long term operation at temperatures up to 550 °C and as low as -269 °C in liquid helium. The fundamental structure of the transducer described by Muto and Atsuta is very similar to that typically seen on air coupled transducers, with a thin faceplate and a piezoelectric element bonded directly to it, without any matching layers. Other literature sources discuss similar transducer designs employing braze joining of piezoelectric material and the steel envelope [25, 27-29, 34]. It was found that literature sources did not offer coherent long term service reliability data of these types of joints when used in continuously varying temperatures, but generally relied on fixed temperature tests. This method of transducer assembly appears to have two major problems which need to be solved simultaneously; integrity of the bond and the acoustic performance of the assembly. Shirzadi *et al.* [34] tackle the integrity of the bond and highlight the effects of differences in thermal expansion of the components to be joined. Shirzadi *et al.* argue that even with the optimum brazing bond, the thermal mismatch between ceramic and stainless steel for example is an intrinsic feature and can not be avoided. An alternative method is then proposed where some of the thermal expansion coefficient mismatch is buffered by an intermediate layer constructed with metallic foam. Using this method Shirzadi *et al.* report significant improvements in joint resilience to thermal stresses. However, there is presently no literature available on the use of this technique in the construction of ultrasonic transducers for high temperature applications and it is an area that will be explored further in later sections.

A variation on the ceramic-to-metal brazing assembly method is the use of adhesives and epoxies for mechanical coupling between different components within the transducer. For low temperature applications, particularly those below 120 °C, this is by far the most favoured assembly method as it is relatively simple to apply in volume manufacture and there is a good choice of vendors and solutions available for adhesives and epoxies to cover most acoustic and electronic requirements.

A common method for fabrication of ultrasonic transducers is to use the transducer envelope as an electrical ground connection for the excitation signal. The envelope is then directly coupled to one of the piezoelectric element (PE) electrodes through a

high conductivity adhesive bond. An example of this type of transducer construction is shown in the Figure 2-8. Commercially, this is a very popular design as it is inexpensive. However, it is completely unsuitable for temperatures even as high as 120°C. A good study of bonding and brazing methods for use in high temperature ultrasonic devices was conducted by Butler et al. [27]. The study compared the suitability of solder, ceramic and gold-indium as joining materials for ceramic and steel at high temperatures and the results suggested that gold-indium braze is the most reliable method for temperatures up to 400°C. However, Krause [35] reports that high pressures of up to 345 MPa are required for a successful bond. This would make this method unsuitable for thin ceramic disks due to the high probability of fracture of the ceramic.

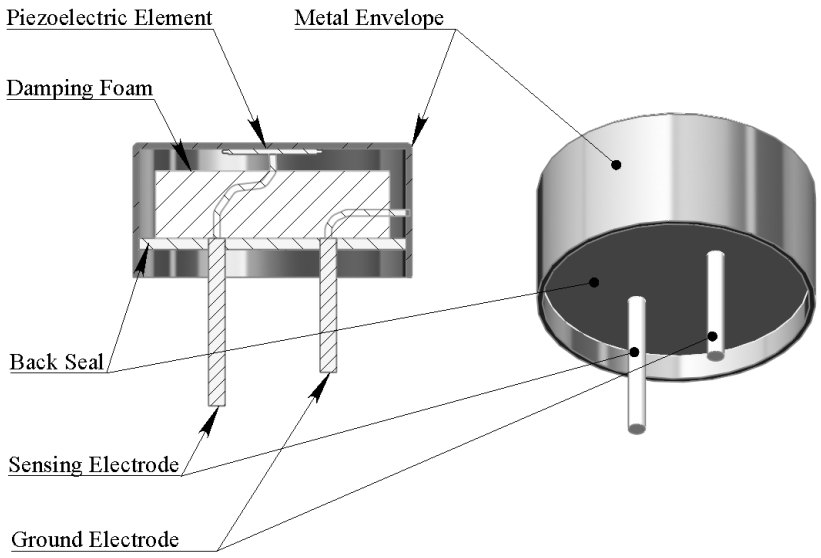

Figure 2-8 Cross-section of a typical low temperature, ultrasonic air transducer assembly. This particular design uses electrically conductive adhesive to bond the piezoelectric element to the aluminium can, which is then used as a ground (reference) terminal.

McNab *et al.* [25] and a number of other authors [32, 36-38], present an alternative assembly method which does not rely on brazing or adhesive bonding of materials. A spring or some other 'entrapped' loading method is used to hold the assembly under compression, and some form of liquid (e.g. glass solder) or dry (intimate, polished contact) coupling is used. A practical example of such an assembly is shown in Figure 2-9. This particular example is designed for NDT applications where acoustic mismatch between the protective face of the transducer and the material under test (usually a solid) is relatively small.

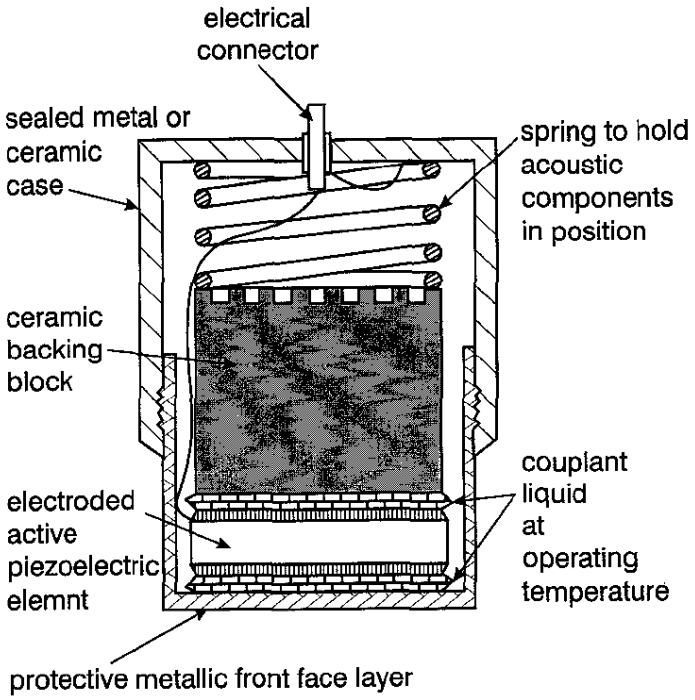

Figure 2-9 Reproduced schematic diagram of a high temperature ultrasonic transducer as proposed by McNab [25]. It shows the piezo-ceramic disk held under compression against the faceplate of the transducer by the spring.

This type of transducer arrangement is typically less efficient than the transducer assembled with the adhesive, epoxy or brazing methods described previously. This is due to the large mechanical mass of the device, which requires a significant proportion of the energy to keep it moving at resonant frequency. However, the advantage of this technique is the reduced risk of delamination of materials at higher temperature. Thermal expansion coefficient mismatch simply does not cause the catastrophic failure exhibited by the other adhesive or brazing methods.

One common factor between all transducer assembly methods is the use of a metallic envelope or casing to house the piezoelectric element and other components sensitive to contamination. Second only to the piezoelectric material itself, the envelope is the most important item in the assembly as it forms a protective barrier against the environmental influences of temperature, dust, corrosive gasses and liquids as well as protecting against mechanical damage. The complexity of the envelope construction and of the materials used is generally dependent on the intended use, and materials such as ABS thermoplastic, for example, have been successfully used in certain applications, such us automotive parking sensors. Based on industrial experience over a number of years in sampling and measurement inside industrial smoke stacks, stainless steel 316 (SS316) comes out as a pragmatic choice of material for use as the sensor envelope. This is not to say that this is an ideal material, but it is a reasonable compromise based on costs and physical properties. Other materials commonly used in aggressive environments at high temperature are superalloys such as Inconel and Hastelloy or titanium. However, material costs are significantly higher and there are also added complexities when it comes to fabrication of delicate transducer parts, mainly due to work hardening.

2.2.1. Energy Loss Mechanisms in Ultrasound Applications

By definition, a transducer is a device that converts one form of energy into another. The process of energy conversion always exhibits losses, which are cumulative in nature and may be caused by different mechanisms. In general terms load and source impedances need to be suitably matched in order to maximise the efficiency of the conversion system. In addition to electrical losses occurring during conversion from electrical stimuli into mechanical motion in an acoustic source, second order losses result at interfaces between two adjacent materials; if the two materials are of equal acoustic impedance and are in intimate contact, then losses are negligible. An ultrasound air transducer is typically made up as a stack of engineering materials bonded together, which transfer mechanical vibrations from the piezoelectric source into air or a gas medium. In this case source and load impedances can not be matched and the objective is to make impedances work in concert to achieve maximum power transfer efficiency. The means of quantifying the quality of the impedance match between different layers are transmission and reflection coefficients as described in Figure 2-10.

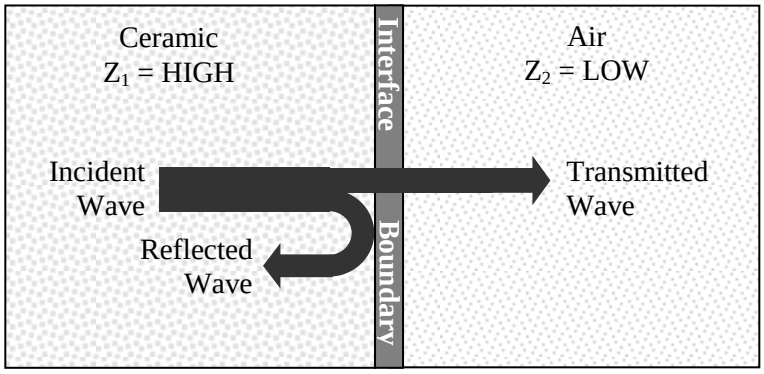

Figure 2-10 Reflection and transmission components of the longitudinal incident acoustic wave at the material boundary layer between a high impedance material such as ceramic and a low impedance material such as air.

Other than on the magnitude of the power output of a transducer, transmission and reflection coefficients have a broad influence on other properties such as frequency bandwidth and ringing [24], making impedance matching a very important aspect of acoustic transducer design. The acoustic impedance, *Z*, of a material is given by

$$Z = \rho \cdot c \qquad \textbf{Eq. 2-7 [39]}$$

where ρ is the material density and c is the speed of sound in the material. It can therefore be said that for two dissimilar materials, which are intimately bonded as shown in Figure 2-10, the reflection coefficient is given by

$$R = \frac{Z_2 - Z_1}{Z_2 + Z_1} \qquad \textbf{Eq. 2-8 [36, 39]}$$

And the transmission coefficient is given by

$$T = \frac{2 \cdot Z_2}{Z_2 + Z_1} \qquad \textbf{Eq. 2-9 [39]}$$

where Z_1 and Z_2 are the source and load impedances respectively. Lynnworth [24] proposes that two materials of dissimilar characteristic impedances Z_S and Z_L can be matched at the fundamental frequency *f* or its odd harmonics *3f, 5f, 7f* etc., by the introduction of a quarterwave impedance matching layer Z_m with an acoustic impedance of

$$Z_m = (Z_S \cdot Z_L)^{\frac{1}{2}} \qquad \textbf{Eq. 2-10}$$

where Z_L and Z_S are load and source impedances respectively. It is also suggested that broader bandwidth can be achieved by using two or more matching layers, although devices with more than two matching layers are seldom found in use. This approach was successfully applied by Desilets *et al.* [40] in applying transmission line theory as an optimisation technique for matched ultrasonic transducer design. It is demonstrated that two or more acoustic matching layers, having monotonically

changing acoustic impedance from Z_L to Z_S, can be used to maximise efficiency of the transducer. In the paper, Desilets *et al* emphasise the importance of taking into account the thickness of the piezoelectric material as well as the need for strict control over the thickness of the quarterwave matching layers and inter-layer bonding. Sensitivity to thickness tolerance as low as 10 μm is apparent, making it difficult to manufacture reliable transducers.

Desilets *et al*. have used a range of epoxy based matching materials in experiments such as Dow Epoxy Resin 332. As a first approximation for selection of suitable matching layer materials, the authors give guidance values as shown in the table below;

Impedance	$\mathbf{Z_S}$	$\mathbf{Z_2}$	$\mathbf{Z_3}$	$\mathbf{Z_L}$
One Section	Z_S^2 / Z_L			Z_L
Two Sections	$Z_S^{4/3} / Z_L^{1/3}$	$Z_S^{2/3} / Z_L^{1/3}$		$Z_S^{2/3} / Z_L^{1/3}$
Three Sections	$Z_S^{8/7} / Z_L^{1/7}$	$Z_S^{3/7} / Z_L^{4/7}$	$Z_S^{6/7} / Z_L^{1/7}$	$Z_S^{6/7} / Z_L^{1/7}$

Table 2-1 Starting basis for transducer design and selection of impedance matching materials according to Desilets et al. [40]. This approximation is based on transmission line model where Z_S is the source impedance and Z_L is the terminating load impedance of the transmission line. Z_2 and Z_3 are the intermediate layers.

The impedance matching layer is also used to alter or damp the frequency response and resonant properties of the transducer. This application is discussed in more detail by Silk [41], who proposes the relationship

$$W = \frac{(Z_D - Z_A)\cdot(Z_D - Z_B)}{(Z_D + Z_A)\cdot(Z_D + Z_B)} \qquad \textbf{Eq. 2-11 [24, 41]}$$

where W is the square root of the trapped energy after one oscillation, Z_D is the acoustic impedance of the piezoelectric disk, Z_A is the acoustic impedance of the matching layer (also the layer exposed to the load), and Z_B is the acoustic impedance of the backing layer. In general terms, $W > 0.75$ suggests prolonged ringing in the ceramic disk, W of around 0.3 presents a condition adequate for most ultrasonic transducer work, whilst, $W < 0.1$ indicates broadband transducer response.

A simplified transducer construction as described by Eq. 2-11 suggests that the matching layer (Z_A) is in direct contact with external medium and therefore needs to have adequate mechanical, thermal and chemical resistance. For this reason, the best material is usually a compromise between an appropriate acoustic impedance match and a suitably rugged material which will protect the integrity of the transducer.
According to Lynnworth *et al.* [42], this compromise can be achieved by using a metallic window. The thickness of the window is suggested as 50 μm for stainless steel and 250 μm for titanium. The authors argue that at ultrasonic frequencies below 100 kHz, the thickness of the window is relatively small in comparison to the wavelength and therefore the acoustic losses are also small. This is in agreement with general market trends for air transducers operating at frequencies of around 40 kHz, where simplified construction allows for low cost devices with adequate efficiency without additional matching layers.

The role of the backing material is to absorb the acoustic energy generated within the transducer itself and prevent it from interfering destructively with the vibration of the piezoelectric element. On low temperature transducers without matching layers, open cell foam is typically found fulfilling this role, whilst more complex, matched transducers generally have an intimately coupled rubber like backing material. For the latter construction, Asher [36] considers the bond between the backing material

and the piezoelectric element, and the influence it has on energy absorption. It has been observed that a particularly intimate contact is required and that gaps of few μm are enough to result in reflection rather than transmission at the interface between the two materials. As a general rule, Asher [36] suggests plastics and rubber as useful backing materials; they can also be mixed with lead, tungsten, copper and other metals in order to tune their performance. A suitable bonding method for ultrasonic applications is discussed in detail by Papadakis [43] and the method has been experimentally applied by Desilets [40]. A range of materials relevant to the field of ultrasonic transducer development is discussed by Ristic [39]. Ristic highlights some of the material properties and covers boundary conditions between different materials as a critical aspect to be considered during design. Some relevant materials and their properties are listed in Table 2-2.

Material	Mass Density $kg.m^{-3}$	Longitudinal Velocity, $m.s^{-1}$	Acoustic Impedance, $\times 10^6\ kg.m^{-2}\cdot s^{-1}$	Ref.
Air (20°C)	1.21	340	411×10^{-6}	[39]
Teflon	2160	1340	3	
Epoxy resin	1100-1250	2400-2900	2.7-3.6	
Silicon rubber	1010	1030	1.04	
Aluminium	2695	6350	17.1	
Brass	8100	4430	35.9	
Titanium	4500	6071	27.3	
Stainless steel	8090	5610	45.4	
Lithium niobate (Z cut)	4640	7330	34	
Lead metaniobate (K81)*	6200	3323	20.6	
Bismuth titanate (K12)*	7000	4620	32	[44]
Bismuth titanate (K15)*	7100	4000	28	
PZT (K180)*	7700	4130	32	
PZT (K270)*	7600	3980	30	

* *Commercial product code*

Table 2-2 Characteristics of some piezoelectric and some non-piezoelectric materials as given by Ristic [39]. The author points out that the values should be considered as an average and for piezoelectric materials, the value is measured along the poling axis, unless otherwise stated.

Ultrasound air transducers are generally constructed with a range of different materials and an example of a commercially available transducer for use in low temperature smoke stacks is shown as a cross-section model in Figure 2-11.

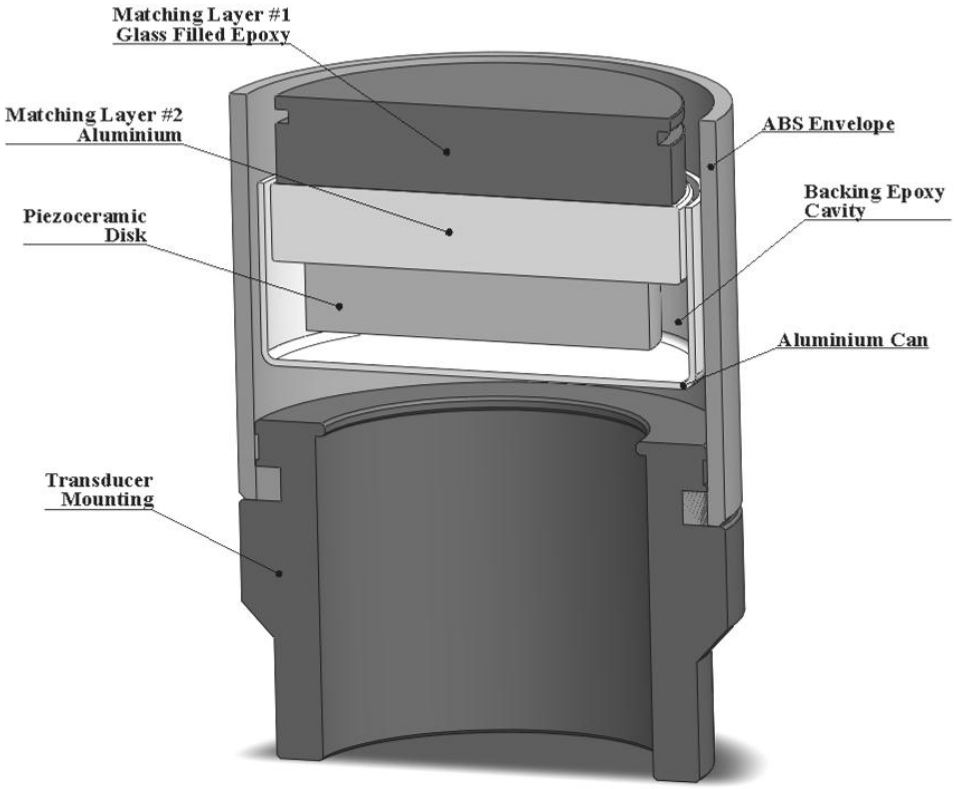

Figure 2-11 Cross-section model of a typical, commercially available ultrasonic transducer suitable for use in low temperature smoke stacks and other gas applications.

Chapter 3 Piezoelectric Ceramics and Their Development

Since the discovery of the piezoelectric phenomenon around 130 years ago, the commercial interest in related materials has grown steadily. Commercial demand for materials exhibiting the piezoelectric effect has resulted in significant amounts of investment, over a relatively long period of time, with the science continuously advancing in terms of material properties and introduction into new applications.

This chapter is a literature review of some historical milestones and current developments in the field of high temperature, lead-free piezoelectric materials as well as the overview of some of their characteristic properties.

3.1. Historical Perspective

The piezoelectric phenomenon was first discovered by brothers Jacques and Pierre Curie [38, 45, 46], as a property of certain crystals to develop an electric potential in response to a directly applied mechanical stress. This is generally referred to as direct effect, and was first documented in 1880. The discovery was in part the result of study conducted by the Curie brothers on the relationship between the pyroelectric effect and crystal symmetry [47]. After the publication of several papers on the subject and after expanding their research to include a number of other materials, the Curie brothers generated a significant amount of scientific interest in this new phenomenon, including that of W. G. Hankel. Hankel, based partly on his own research on pyroelectricity, proposed that this new phenomenon obeyed special laws of its own and suggested the name "piezoelectricity" [47], which was readily accepted by the scientific community. Within a year of the publication of the Curies' paper on

the direct effect of piezoelectricity, Gabriel Lippmann mathematically proved the existence of the converse effect, whereby the material will change its physical dimensions in response to an applied electric field, and this was experimentally confirmed by Jacques and Pierre Curie in 1881. Their subsequent paper on the converse effect demonstrates that the piezoelectric coefficient of quartz has the same value for both the converse and the direct effects [47].

The onset of World War I and the ingenuity of French scientist Paul Langevin ensured the scientific focus on piezoelectricity remained. By defining a new type of application which would stand the test of time even to this day, Langevin's pioneering work on using piezoelectric materials to generate and detect ultrasound, in this case for detection of German submarines, has formed the foundation on which the scientific community has been building for decades. Even though the sonar device was not successfully deployed prior to the end of World War I, this work has led to countless applications in the field of ultrasound and other applications. A detailed review of applications for piezoelectric materials has been published by Moseley and Crocker [48].

The surge in interest after discovery of the phenomenon, centred on the thermodynamic mechanisms of piezoelectricity, brought forth significant advances in the methods of study of crystallography and a substantial body of work was brought forward by Woldermar Voigt in 1894 in his book "*Lehrbuch der Kristallphysik*" (Textbook on Crystal Physics). According to Caddy [47], by examining the symmetry of the 32 known crystal classes, Voigt defined in which of the classes there is a potential for piezoelectric effect. This is in agreement with later works by other researchers and the significance of this classification in terms of the present research is that certain crystal structures empirically imply absence of piezoelectric effect [38, 47]. The most basic requirement for the piezoelectric effect in a material is a non-centrosymmetric crystal structure. However, even with this condition met, there is no guarantee that the piezoelectric effect will be present, as the geometry of the unit cell may alter in response to external stimuli such as temperature change, electric field or mechanical stress. Furthermore, the literature suggests [49] that it should not be assumed that non-centrosymmetric crystal classes will have a polar direction [50].

There are 230 possible configurations of atoms within a crystallographic unit cell [47, 49], and these combinations are generally referred to as crystallographic space groups [49]. Ignoring the translational repetitions, space groups can be segregated into 32 crystal classes or so-called point groups. Point groups are defined by geometrical symmetry factors like rotational axis, reflection planes and centres of symmetry, whilst space groups are defined mainly by translational symmetry between unit cells.

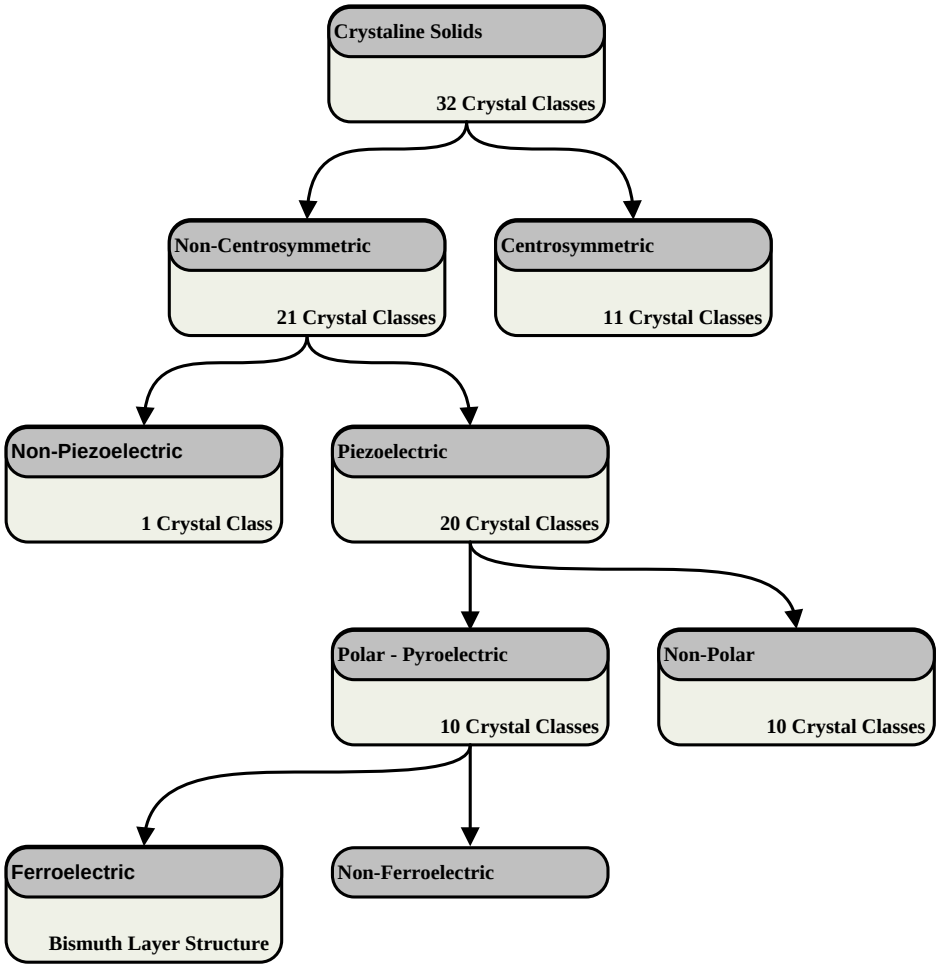

Figure 3-1 Diagrammatical representation of 32 crystal classes within context of crystal symmetry, piezoelectric, pyroelectric and ferroelectric properties.

The organization of crystal classes is described diagrammatically in Figure 3-1 [49, 51]. Of the 32 crystal classes [48, 49, 52], 11 are centrosymmetric, having no dipole moment and therefore exhibit no piezoelectric effect. The remaining 21 classes do not have a centre of symmetry and 20 of these exhibit the piezoelectric effect. One of the classes, cubic class 432, has certain symmetries which combine and result in no piezoelectric effect [49, 52]. From studying the diagram, it can be said that all ferroelectric materials are pyroelectric, all pyroelectric materials are piezoelectric and that all piezoelectric materials are non-centrosymmetric.

By definition, piezoelectric properties are dictated by the unit cell geometry of the crystal, making it very sensitive to temperature changes. This is particularly evident in polar crystal classes which exhibit finite polarisation even at zero field or stress. This property is called spontaneous polarization, and is generally referred to as the pyroelectric effect. Its effect is analogous to that of mechanical stress.

It can be said that any piezoelectric material will develop an electric charge in response to mechanical stress caused by temperature gradient across its bulk. However, only pyroelectric materials will develop charge when uniformly heated [38]. Examining the diagram of Figure 3-1, there are 10 crystal classes that are polar and hence exhibit spontaneous polarisation and the pyroelectric effect. The pyroelectric property is discussed at length by Burfoot [49], Megaw [46] and Jaffe et al. [38], whilst practical applications for materials exhibiting this property are discussed by Herbert [50].

Ferroelectric materials are a subgroup of materials exhibiting the pyroelectric effect and as such, they also exhibit spontaneous polarisation. This group of materials is interesting in that they lend themselves well to the switching of the direction of the dipole moment in response to an applied electric field. Looking at Figure 3-1, it is apparent that the number of crystal classes exhibiting this ability to change polar direction is few. The relationship between the applied field and the magnitude and sign of the dipole moment gives rise to hysteresis; analogous to that found in ferromagnetic materials. It was Valasek [53] who first reported hysteretic behaviour after observing it in Rochelle salt crystals, and he made a comparison to the ferromagnetic hysteresis phenomenon, which subsequently gave rise to the term

ferroelectricity. Ferroelectric materials do not exhibit strong piezoelectric properties due to weak non-symmetry in the crystal; however, the effect can be further improved by a process known as poling. Here, a strong electric field is applied across the sample at an elevated temperature for a defined period of time, and during this 'polarisation time', domain alignment will occur. The main purpose of the poling procedure is to encourage individual dipole vectors to align with the applied field and thereby reduce mutual cancelling.

A more in depth discussion of ferroelectricity can be found in Burfoot [49], Cady [47], Megaw [46], Valasek [53] and Jaffe et al. [38].

3.1.1. Piezoelectric Nomenclature

Physical constants of piezoelectric materials are generally discussed using conventional notation which identifies the property, crystallographic direction of applied stimuli, direction in which the property is being measured and the poling direction. This takes the general form of notation as d_{ijk}; where i, j and k represent different orientations.

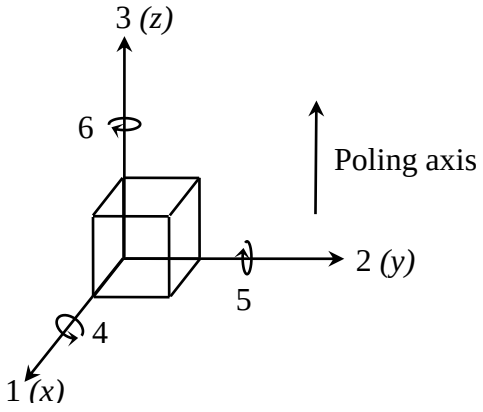

Figure 3-2 Conventional notation of piezoelectric axes. *Z* (3) axis is generally accepted as the polarisation axis.

In reference to Figure 3-2, the polarisation is generally confined to the *z* or *3* direction. Although *x*, *y* and *z* notation is commonly used to put the example into context of general 3D representation, numbers 1, 2 and 3 respectively are used to represent longitudinal, and 4, 5 and 6 are used for shear stresses.

Some other frequently used constants along with their units are [38, 54, 55];

d	Piezoelectric charge coefficient	pC N^{-1}
g	Piezoelectric voltage coefficient	Vm N^{-1}
k	Piezoelectric coupling coefficient	Ratio of mechanical energy available to electrical energy applied
s	Elastic compliance	Ratio of stress to strain
ε	Dielectric permittivity	Ratio to reference (vacuum)

In order to further define the boundary condition, a superscript is generally used and convention is shown in Table 3-1.

Coefficients	Parameter	Symbol	Conditions
ε	Stress	T	Mechanically free
	Strain	S	Mechanically clamped
s	Field	E	Electrical short circuit
	Displacement	D	Electrical open circuit

Table 3-1 Definition of Boundary Conditions [38, 54, 55].

Using the example of elastic compliance, it can be defined as s_{11}^{D}, where the first subscript indicates the direction of the applied stress and the second is the direction in which the strain is being observed. Superscript *D* means that compliance is measured with the piezoelectric material in an open circuit configuration.

3.2. Crystallography of Piezoelectric Materials

One of the most widely used and researched piezo-ceramic materials today is lead zirconium titanate or PZT. The main reason for its popularity is its extremely good piezoelectric properties and relatively low cost of manufacture. However, its weaknesses are that it has a very low Curie temperature, coupled with toxicity of lead oxide, some of which is emitted by vapour lost mainly during sintering of the material and also from leaching during use [56].

Sintered ceramics, such as PZT, tend to be stable but research has shown leaching of lead dissolved from PZT into water [57], indicating a possible path for contamination into the human body. This non-biocompatibility is an undesirable property of PZT.
Global trends to reduce the amount lead released into the environment are putting pressure on users and manufacturers alike to switch to lead free alternatives. Maeder *et al.* [57] have conducted a review of recent research focused on such alternatives. Other than non-biocompatibility of PZT, it is also limited to low continuous operating temperatures.
The advantages of being able to operate at temperature in excess of 400 °C is appealing to industrial users and Maeder *et al.* identify the potential of bismuth layer compounds as a good alternative material with high T_c. It is shown that ionic substitution can be used successfully to improve structural and piezoelectric properties. This strategy is well utilised and a number of other authors report successes in improving properties of lead free alternatives [58-61].

An alternative approach, which is often applied in parallel with ionic substitution, is the modification in the ceramic processing route. It has been shown that grain size and orientation in a polyceramic material is the key factor influencing its electrical and piezoelectric properties [62-64]. The conventional solid state sintering route is the most cost effective method of producing large quantities of bulk material, but it offers very little control over grain orientation. Highly textured materials produced by hot pressing [65, 66], forging [67] and spark plasma sintering (SPS) [62, 63, 66, 68] techniques have yielded extremely good improvements in overall properties of these materials.

3.2.1. Materials with High Curie Temperatures

For ferroelectric materials, spontaneous polarisation is present below the Curie temperature (T_c). Above the T_c, the structure assumes a symmetrical cubic form and as a result, the ferroelectricity and piezoelectric effect ceases to exist [47]. This is referred to as thermal depolarisation of electrical domains. In the case of ferroelectric crystals, spontaneous polarisation is restored when the temperature is reduced below T_c. However, for polarised piezoelectric materials, the net polarisation is permanently lost when the crystal is taken above T_c and can only be re-established by repeating the polarisation process [50].

Bismuth titanate, $Bi_4Ti_3O_{12}$ (BIT) has been selected as a good candidate for high temperature applications. This Aurivillius phase, also referred to as bismuth layer structure ferroelectric or BLSF, and other members of this family, generally have a high T_c and low ageing rate [69]. Survey of some materials with high T_c is summarised in Table 3-2.

Compound	Curie Point [°C]	Dielectric Permittivity *	d_{33} * [pC N^{-1}]	References
$Bi_4Ti_3O_{12}$ *Single Crystal*	675°	180	20	[38]
Bi_3TiNbO_9 *Single Crystal*	930°	100		[38]
$CaBi_2Nb_2O_9$ *Polycrystal*	943°	100 – 200	7 - 19	[70]
$PbTiO_3$ *Polycrystal*	460° – 520°	~150	45 - 56	[71]
$LiTaO_3$ *Polycrystal*	665°		6	[72]
LiNbO3 *Single Crystal*	1200°		d_{22} = 21	[72]

* *Room temperature values*

Table 3-2 Selection of materials with high T_c. (Values given here are typical).

Several compounds listed in Table 3-2 remain ferroelectric at temperatures in excess of 900 °C, far higher than BIT. However, high conductivity and the magnitude of the electric field required for polarisation (coercive field) are prohibitive factors during the poling process. Other factors such as ageing rate and oxygen loss at high temperature (particularly in lithium niobate) make these materials unsuitable for continuous use at high temperature.

Another notable feature of high T_c materials is the low piezoelectric coefficient, which in most non-single crystal cases is around 10 pC N^{-1} or somewhat higher. Bismuth titanate has been identified as a good candidate for acoustic transducer applications in the 300 °C to 600 °C temperature range [73], and it has been shown that a reduction in conductivity and improvement in the piezoelectric properties of this material can be achieved through Ti-site (referred to as B-site) doping [72, 74-78], accompanied with a marginal reduction in T_c. The structural modification of bismuth titanate is perceived as the key to realising significant improvements in its piezoelectric properties.

3.2.2. Perovskite and Aurivillius Phases

PZT is a perovskite, meaning that it belongs to a family of crystals assuming a structure similar to that of $CaTiO_3$. Most useful ferroelectric materials are perovskites [71], and they have a general formula ABO_3 with a closely packed FCC structure as shown in Figure 3-3. The two cations, A and B, are of distinctly different sizes and the larger of the two is accommodated at the A-site. The A-site can accommodate mono, di or trivalent cations such as La^{3+}, Nd^{3+}, Pr^{3+}, Sm^{3+}, Bi^{3+}, Pb^{2+} and Ba^{2+}, whilst the B-site is occupied by smaller cations such as Ti^{4+}, Nb^{5+}, Ta^{5+} and W^{6+}. In a 6-fold coordination with the oxygen anion, B cation forms the centre of a BO_6 octahedron, which repeats and shares corner atoms (Figure 3-3a), whilst A-site cations occupy holes between BO_6 octahedra in a 12-fold coordination (Figure 3-3b). Figure 3-3b shows a three-dimensional network of BO_6 octahedra which share corner oxygen atoms and accommodate an A-site cation in the middle.

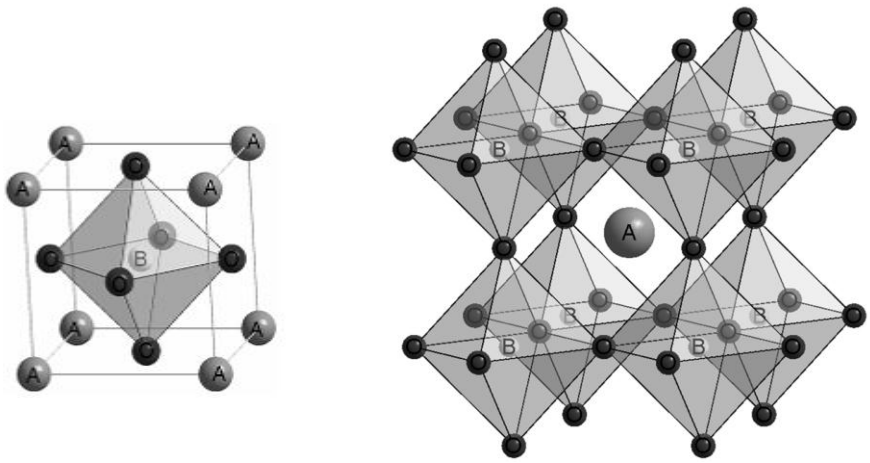

(a) *(b)*

Figure 3-3 Schematic representation of the ideal perovskite unit cell. Diagrams *a* and *b* show two conventional viewing configurations typically found in literature.

The stability of the perovskite structure is directly linked to the ionic radii of the A, B and O atoms, R_A, R_B and R_O respectively. It can be quantified by calculating the Goldschmidt tolerance factor *t* [79];

$$t = \frac{R_A + R_O}{\sqrt{2}(R_B + R_O)} \qquad \textbf{Eq. 3-1 [79]}$$

It has been suggested that stable structures have a tolerance factor $0.9 < t < 1.1$ [56] and deviation from this range results in the failure to form a crystal with the perovskite structure ABO_3. The spontaneous polarisation below T_c is the product of non-symmetrical distortion of the unit cell due to displacement of titanium and oxygen ions [80], and is depicted in Figure 3-4. In a polarised (tetragonal) state, the oxygen anions are displaced slightly below the centre of each of the faces of the cell, whilst the central B cation is located slightly above the centre of the cell, thus establishing a permanent ionic dipole moment.

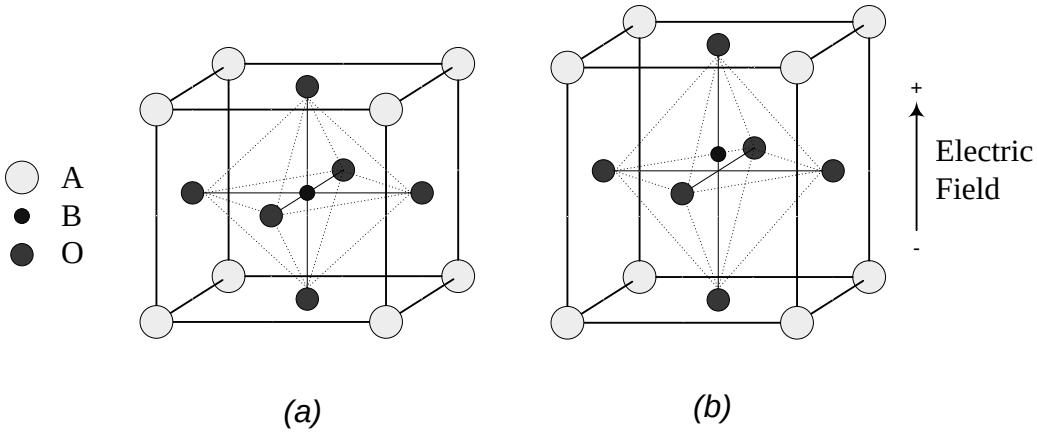

Figure 3-4 Perovskite cell; Non-polarised cubic (left) and polarised tetragonal (right).

Bismuth titanate is a perovskite compound, albeit with a layered structure, meaning that sheets of perovskite layers are interlaced with layers of bismuth oxide. It belongs to a family of compounds with this type of crystallographic arrangement, which are generally referred to as Aurivillius or bismuth layer structure ferroelectric (BLFS) compounds.

These compounds can be represented by a general formula; $(A_{m-1}Bi_2B_mO_{3m+1})^{2-}$. Here, 'm' is the integration factor having the range between 1 and 6 [70], and is the number of pseudo perovskite like layers separated by $(Bi_2O_2)^{2+}$ layers along the crystallographic c axis. In case of pure bismuth titanate $Bi_4Ti_3O_{12}$ (BIT), m = 3. Figure 3-5 shows a schematic diagram indicating significant features of the BIT unit cell.

It can be seen that the Bi ions occupy not only positions in the perovskite layer, but also in the bismuth oxide layer. Aurivillius (1950) [81] suggested that symmetry of BLSF compounds in ferroelectric phase is likely to be tetragonal. However, using XRD methods, Subbarao (1961) argued that the symmetry is in fact orthorhombic [82, 83]. More recent studies conducted by Jardiel et al. (2008) [84] and Rodel et al. (2009) [56], have shown that Aurivillius phases generally have an orthorhombic structure, however, BIT is an exception in that it maintains monoclinic symmetry. It is important to note that the choice of axes for the Aurivillius crystallographic model does not follow the orthorhombic convention $c < a < b$, however, it is convenient since *a* can be perceived as the polar axis [72, 85].

Jardiel et al. [84] suggests that for BLSF members with an even integration factor *m*, spontaneous polarisation will only exist along the *a* axis, whilst for those with an odd integration factor, in addition to a large polarisation vector in the *a* direction, there is a weak component in the c-direction, which can be switched independently. This is supported by published data [85] and BIT, with an integration factor of 3, exhibits spontaneous polarisation in both *a* and *c* directions with a factor of 10 difference in magnitude.

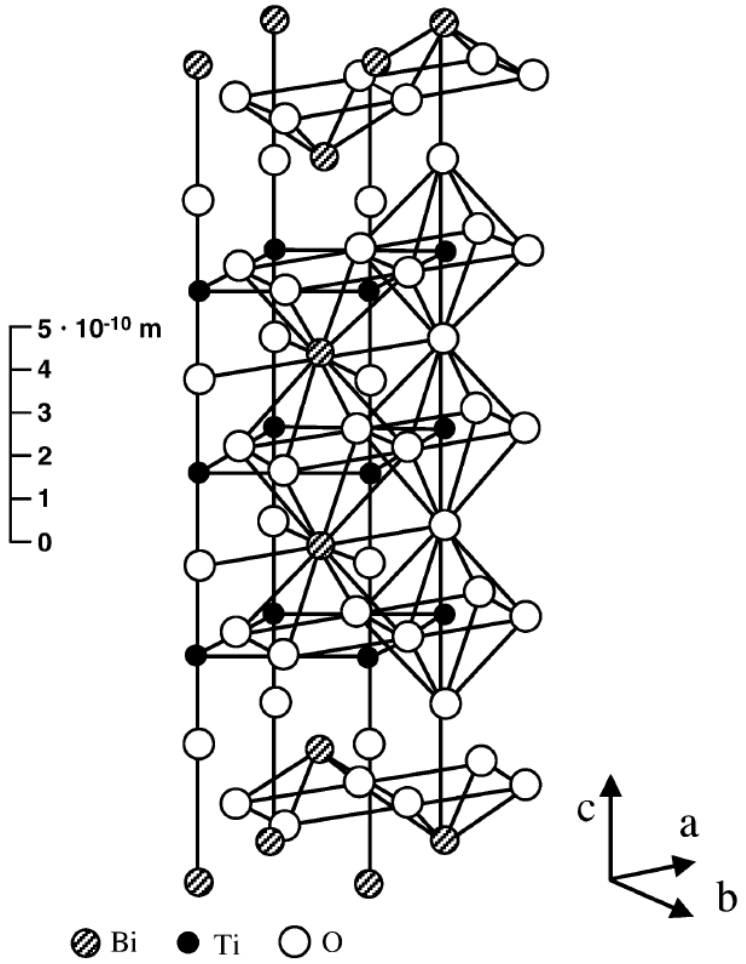

Figure 3-5 Schematic diagram of a half Aurivillius unit cell. Adapted from Aurivillius [81]. It shows three pseudo perovskite layers which infinitely expand in *a* and *b*, and are interlaced with bismuth oxide layer along *c*.

3.2.3. Origins of Ferroelectricity in $Bi_4Ti_3O_{12}$

A study of the structure and ferroelectricity in BIT was published in 1971 by Newnham et al. [86].

The structure can be explained by considering the bismuth oxide layer first. The electron configuration of the oxygen atom valence shell demands two further electrons in order to complete the stable inert gas configuration. This requirement is met by the neighbouring bismuth atom, and each bismuth atom forms a bond with four neighbouring oxygen atoms.
Since oxygen gains two electrons, bismuth must lose two, making it a Bi^{2+} ion. This leaves one electron available for bonding in the valence shell of bismuth, which is taken up by the apex oxygen of the perovskite layer. Since apex oxygen requires further electron to complete its inert configuration, it forms a bond with the B-site cation, pulling the two atoms closer together and resulting in octahedral distortion by way of repulsing remaining oxygen atoms in the centre of the octahedron. This laterally widens the octahedron and weakens the remaining bonds.

For BIT, which has three perovskite layers, distortion of outer layers is mirrored, whilst the middle layer preserves more symmetrical form. The outer perovskite layers are also slightly tilted about the *a* axis caused by the bismuth-oxygen bond strain. This is shown schematically in the Figure 3-6.

It was put forward by Newnham et al. [86] that the source of spontaneous polarisation in BLSF could be attributed to a dipole created by the shift of the octahedral cation from the octahedral centre. Subsequently, it has been shown by Rae et al. [87] that the main contributor to spontaneous polarisation is the displacement of A-site cations along the *a* axis in relation to octahedral chains.

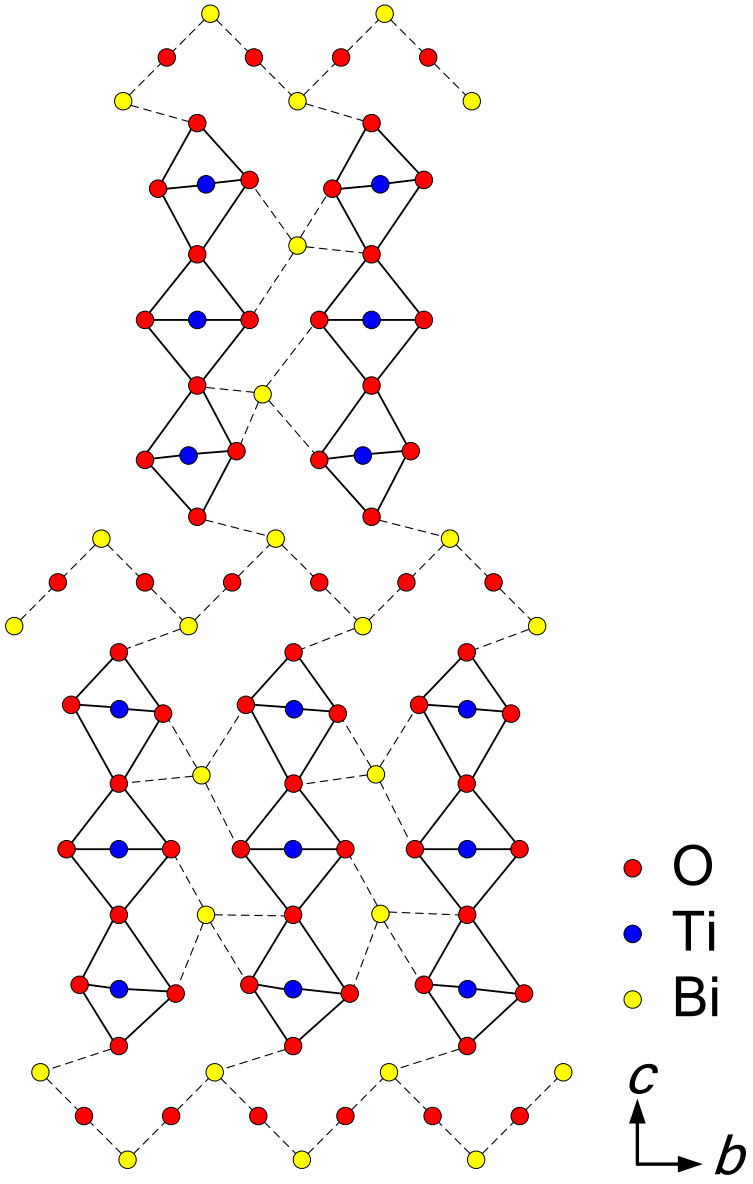

Figure 3-6 Schematic diagram of the ionic bond structure of $Bi_4Ti_3O_{12}$. It shows octahedral tilt about *a* axis. Adapted from Newnham [86].

3.2.4. Implications of Poling on the Properties and Use of Ferroelectrics

Polarised domains are the key feature of ferroelectric materials, which induces strong coupling between electrical and mechanical properties [55].

However, in polycrystalline ferroelectrics, the net polarisation is zero, since individual domains are randomly oriented and hence cancel each other out. It is well known that piezoelectric properties can be vastly improved by the poling process. Essentially, this process exposes the bulk sample material to a high electric field, usually at a relatively high temperature to take advantage of higher domain mobility, for a defined period of time inversely related to the temperature. Figure 3-7 shows the simplified diagram of three states - before, during and after the poling process respectively. Figure 3-7 (a) shows material prior to polarization and since the electric domains are not oriented in any particular direction, the net polarisation of that material is zero. Once a DC field is applied, all domains strive to align themselves in the direction of the field as shown in Figure 3-7 (b). After the electric field is removed, domain relaxation ensues to a certain degree, but a semi-permanent polarisation vector remains, Figure 3-7 (c). The effect of domain alignment is also manifested by the fact that the bulk material will generally elongate in the direction of the polarization axis [88]. Polarisation is semi-permanent since individual domain vectors are under strain to revert back to their original position, which will result in permanent depolarisation. Randeraat and Setterington [55] outline three principal mechanisms that cause depoling and rules for handling piezoelectric materials in order to avoid such depolarisation.

- **Thermal de-poling.** The temperature of the polarised material should be kept well below its Curie temperature. Literature suggests that a safe maximum operating temperature is slightly above $T_c/2$. [54, 55]
- **Electrical de-poling.** The piezoelectric material should not be exposed to excessive AC or DC fields in opposition to the direction of poling.
- **Mechanical de-poling.** Mechanical stresses exerted on the material should be kept within defined limits which are dependant on the material composition.

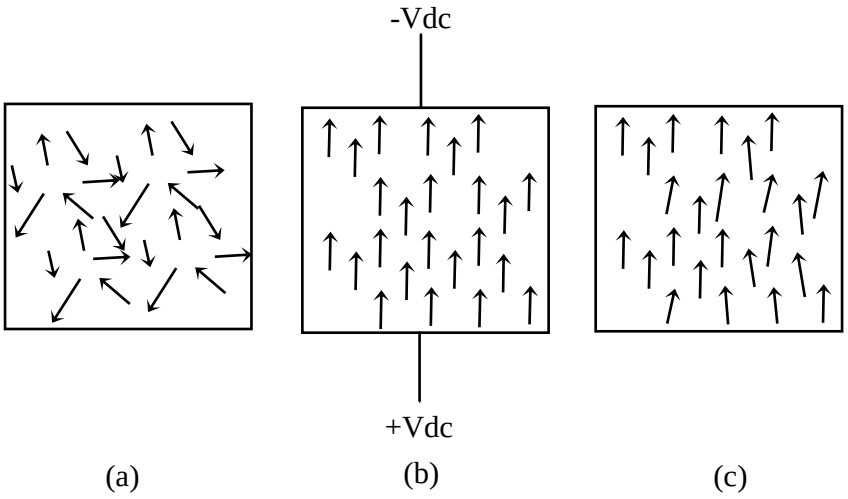

Figure 3-7 Three stages of polarization. Non-polarized, isotropic bulk material (a); Aligned domains during polarization (b); relaxed bulk material showing high degree of remnant polarisation (c).

Thermal depoling is caused when the temperature of the piezoelectric material approaches the Curie point, resulting in a loss of alignment of electrical dipoles. As the Curie temperature is approached, the material polarisation properties sharply deteriorate and subsequently diminish to negligible levels as the Curie point is breached.

Electrical depoling is of course a function of the strength of the field applied across the sample, but is also influenced by the temperature and duration of the applied field. Generally, all piezoelectric materials will depolarise at a lower electric field at a given higher temperature. The type of material will also have some influence on the effect of electric depoling.

Literature suggests [55] a depolarising field strength of 500 Vac or 1000 Vdc (opposite to direction of poling) as a guide.

Mechanical depoling is caused by excessive mechanical stress or strain being applied across the material when the material in open circuit mode. This causes a charge build up on the electrode surfaces and if the charge build up is of same polarity as the direction of poling, no depolarisation will take place. However, if the charge is in the opposite direction to direction of poling, this will have same effect as depolarisation due to an applied DC field [55].

Almost all properties of ferroelectric materials will deteriorate with time [54] a process referred to as ageing. The causes of ageing in ferroelectric materials are subtle in nature but can generally be ascribed to electrical domain-wall pinning and grain boundary effects, exhibiting relaxation-type behaviour. The onset and rate of ageing is largely influenced by temperature.

The ageing rate is specific to a particular material composition but generally ageing occurs in two phases. The first phase lasts up to 48 hours or so from the time of polarisation and it is during this time that the majority of deterioration occurs. The second phase can last many months or even years when the material ages at a very slow rate. This effect causes some practical problems in the use of piezoelectric materials due to degradation of material properties over time. However, it has been suggested that these changes can be reduced by an artificial ageing process where the material is subjected to number of temperature cycles prior to deployment. [89].

3.3. Defects and Doping in Bismuth Titanate

Bismuth titanate $Bi_4Ti_3O_{12}$ is one of the most promising members of the lead-free family of piezoelectric materials, largely due to its strong piezoelectric and ferroelectric properties, coupled with a high Curie temperature. However, pure BIT has a value of piezoelectric charge coefficient around 50 times lower than that of PZT, at $d_{33} < 8$ pC N^{-1}. One of the suggested reasons for this is the relatively high conductivity in pure BIT, which impedes the poling process [74, 75]. Therefore reducing conductivity in BIT is one of the key challenges in improving its piezoelectric properties. The enhancement of BIT properties can also be achieved by grain orientation processing techniques such as texturing [58, 68, 75]. However, this makes the cost of such materials prohibitive for use in most applications. A more favoured approach is to optimise the piezoelectric ceramic through structural modification via doping. It has been shown in literature that piezoelectric properties and morphology of crystals can be successfully controlled by addition of doping and alloying elements into the crystal structure [72, 74, 90]. Observations in PZT show that even small amount of doping can strongly influence defect structure and hence induce variations in sintering kinetics, as well as electrical properties of the ceramic. Understanding of this influence can aid otherwise heuristic approach to optimisation of properties in bismuth titanate. To further elaborate on the proposed structural modifications in BIT, it is useful to consider the perovskite unit cell ABO_3. Since the B cation is much smaller than the A cation, it is confined within octahedral oxygen-ion cage. The larger A cation is therefore restricted to cubohedral space delimited by oxygen octahedrons, joined at corners. This geometry and the size of O_2 ions therefore dictates the size of A and B cations that are allowed in the structure.

The O-O distance along the octahedral edge is given by:

$$x = \sqrt{2}\,(RO + RB) \qquad \textbf{Eq. 3-2}$$

and the suitable radius of the A cation is given by:

$$RA = x - RO \qquad \textbf{Eq. 3-3}$$

Where RA, RB and RO are the ionic radii.

The degree of fit as well as the iconicity of the bond between A and O ions are the determinants of the Curie temperature

Literature shows that doping with donor cations such as Nb^{5+}, W^{6+} and Ta^{5+} in the 'B' (Ti) site of the pseudo-perovskite cell of BIT, decreases electrical conductivity and enhances the material properties [74, 75, 91-93], and this approach is followed in present work in order to improve properties of pure bismuth titanate.

Chapter 4 Experimental Methods

The following chapter describes experimental procedures used in the present work. It details preparation and characterisation of raw materials, calcination, sintering and characterisation of BIT ceramics.

4.1. Processing of Piezoelectric Ceramics

Preparation of ceramic materials is generally a multistage process requiring tight control over factors influencing contamination during thermal treatment and the mechanical handling of the material. Literature indicates particle size of starting oxides between 1 to 10 μm and the strong influence of particle size on the structure of the obtained sample material is suggested [38, 50]. Particles of more than 10 μm produce a polyceramic which contains large intergranular voids which in turn lead to lower density.

Figure 4-1 shows a generic flow diagram of the manufacturing process, typically adopted for preparation of piezoelectric ceramics [50], via the conventional solid state (mixed oxide) sintering method.

Considering the number of processing steps required to produce the final product, this type of approach is very vulnerable to contamination and strict laboratory controls had to be put in place in order to keep the contaminants at the absolute minimum. Jaffe et al. [38] suggests that impurities in raw materials affect reactivity as well as dielectric and conductive properties. However, this method does offer certain cost merits for the manufacture of piezo-ceramic materials in contrast to other reported methods such as polymeric precursor [94, 95], sol-gel synthesis [96], precipitation [97, 98] and hydrothermal synthesis [99] amongst others.

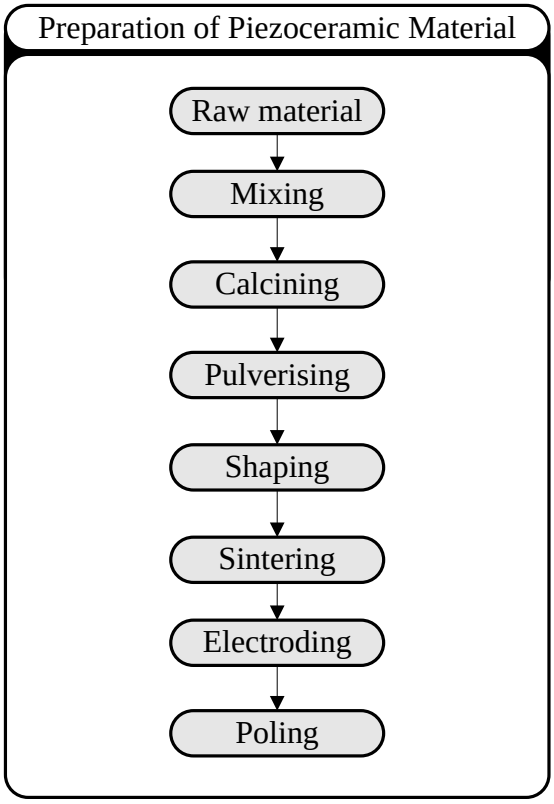

Figure 4-1 Typical stages of conventional, solid state sintering process used for preparation of ceramics [50].

Given the general process diagram in Figure 4-1, the actual processing procedure can vary slightly depending upon specific requirements. This sub-chapter describes the derived preparation process for bismuth titanate in order to manufacture a sample in the form of a small disk having diameter of around 10 - 13 mm and 0.5 mm in thickness. Details of raw materials used in the experiments are given in the Table 4-1.

Powder	Purity	Supplier	Supplier Number	Mean Particle Size [μm]
Titanium (IV) oxide (anatase)	99.8%	Aldrich	232,033	10
Tungsten (VI) oxide	99.9%	Fluka	95410	10
Bismuth (III) oxide	99.9%	S. Aldrich	22,389-1	10
Chromium (III) oxide	98.0%	Alfa Aesar	012286	< 44
Antimony (III) oxide	99.0%	S. Aldrich	230898	5
Niobium (V) oxide	99.9%	S. Aldrich	20,851-5	< 44
Tantalum (V) oxide	99.0%	S. Aldrich	303518-1	10

Table 4-1 Raw materials used in experiments and their relevant purities.

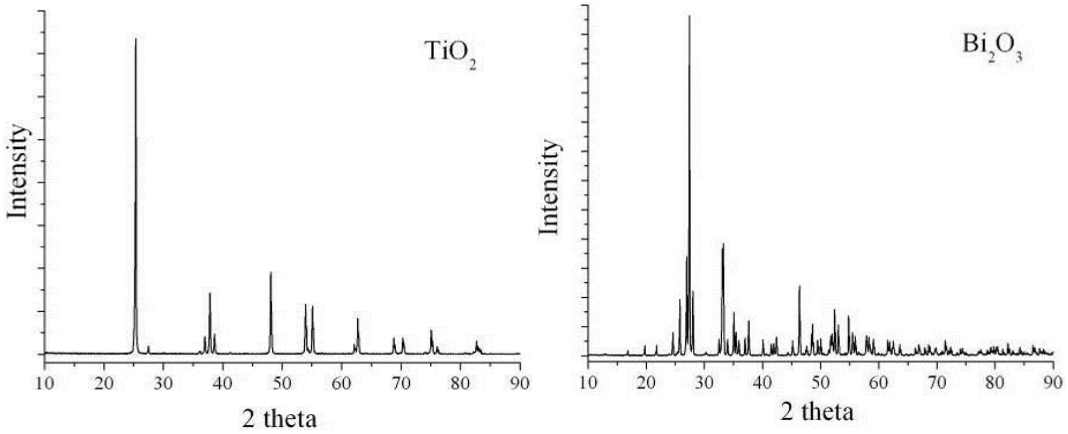

Figure 4-2 X-Ray diffraction patterns of starting titanium dioxide (anatase), and bismuth oxide powder respectively.

Preparation of nominally stoichiometric bismuth titanate $Bi_4Ti_3O_{12}$ was carried out by mixing bismuth oxide and titanium dioxide powders by following the process described in Figure 4-1, with minor deviations or refinements. The simplified diagram of the manufacturing procedure is shown in Figure 4-3. It shows the process divided into four distinct phases.

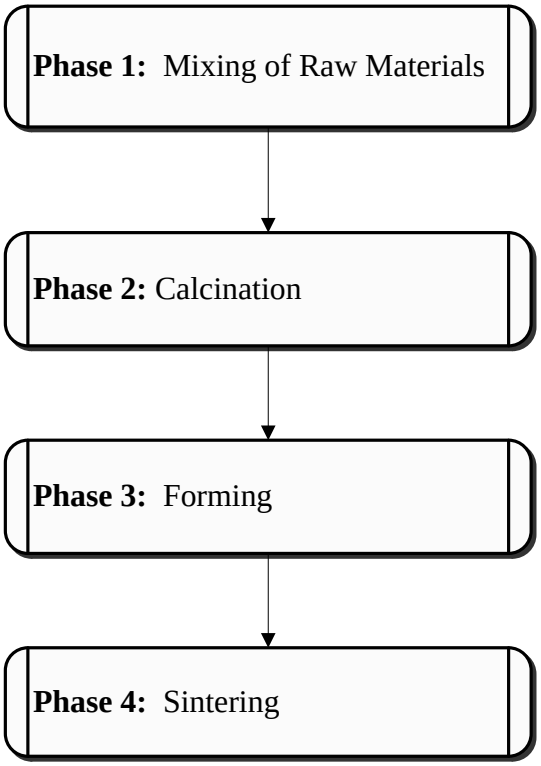

Figure 4-3 Process for preparation of BIT piezoelectric ceramic samples. Each phase of the process required optimisation based on literature and experimental procedure. It was found that slight deviations in processing resulted in non-consistencies in material properties.

4.1.1. Phase 1: Mixing of Raw Materials

The key aspect of this phase is to produce homogenous stoichiometric mixture of starting powders ready for calcination. Starting materials were chosen with particle size of around 10 μm and in the case of titanium dioxide, the anatase structure was selected. It was experimentally determined that batches of 20 to 50 g of powder would be the most suitable quantity for lab production. For all samples conventionally sintered in air, 3 wt% of Bi_2O_2 was added to substitute the loss of bismuth oxide during sintering as suggested by literature [64]. Herbert [50] suggests the particle size below 1 μm for the pre-calcination powder and initial experiments were conducted to determine the correct milling regime. Raw, weighed oxide powders were placed into a 250 ml nylon bottle together with 10 zirconia milling balls, each having typical diameter of 10 mm. Ethanol was added to cover the solid contents of the bottle and the bottle was then placed on a roll mill. Figure 4-4 shows the particle size distribution after milling for 4, 48, 72 and 120 hours. It demonstrates a significant particle size shift to below 1 μm after 72 hours of ball milling and this was deemed as a good compromise for further experiments. After ball milling, the slurry was emptied into a tray and all zirconia milling balls were removed. Ethanol was evaporated in a drying oven leaving dry powder ready for further processing.

Initial experiments conducted using alumina milling balls showed a strong influence on the ceramic properties of BIT ceramic; particularly when the balls were used for the first time. This indicated contamination from the milling media due to the surface roughness of unused balls. Improvements in results were achieved by using milling balls which have been conditioned in the mill for at least 72 hours prior to using them with the BIT powder. The conditioning of milling balls removed the loose particles and smoothed the surfaces, reducing the amount of contamination during BIT powder milling. The process was further improved by substituting alumina balls for zirconia milling balls.

One possible source of processing errors in this phase is the weighing of very small amounts of doping materials used for certain BIT compositions. This was addressed through careful handling of materials and the optimised balance setup. Figure 4-5 summarises the processes of phase 1.

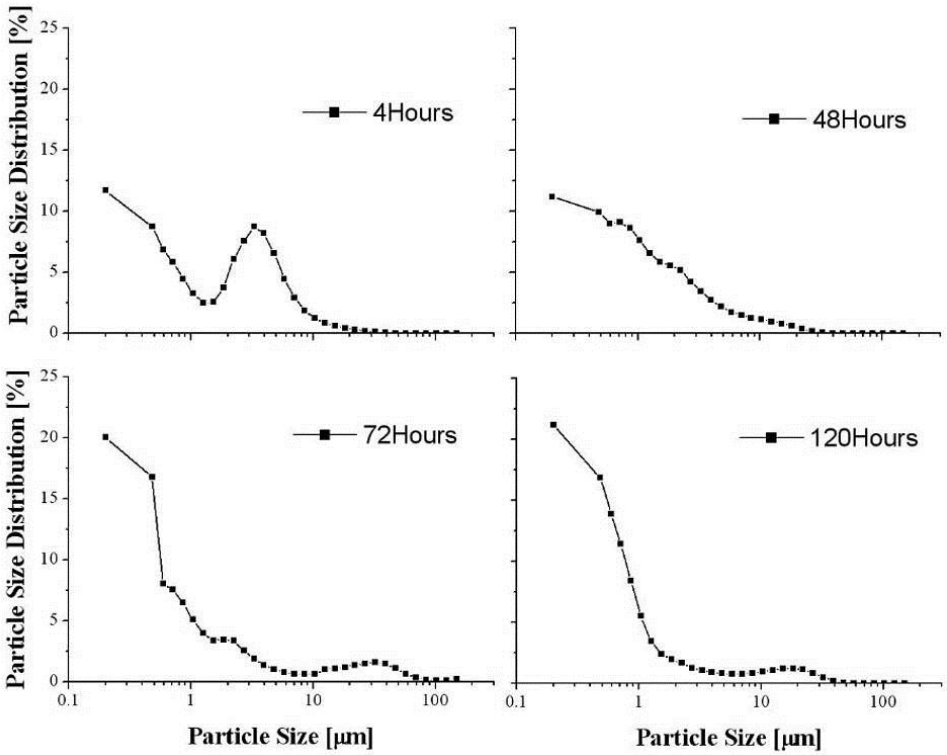

Figure 4-4 Particle size distribution diagrams for 4, 48, 72 and 120 hours of ball milling. Starting powder was 10 μm in diameter.

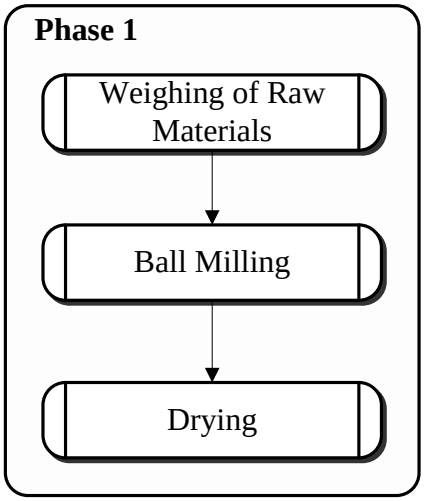

Figure 4-5 Phase 1 process steps. Contamination and loss of raw material was critical during this phase.

4.1.2. Phase 2: Calcination

Calcination is a term used to describe a solid state reaction process of oxides, at a substantially lower temperature than that of sintering. There are three main reasons for carrying out this procedure separately from the sintering process;

1. To remove any organic contaminants.
2. To induce a thermo-chemical reaction between oxides.
3. To allow the majority of material shrinkage to take place prior to shaping of the sample[38, 71].

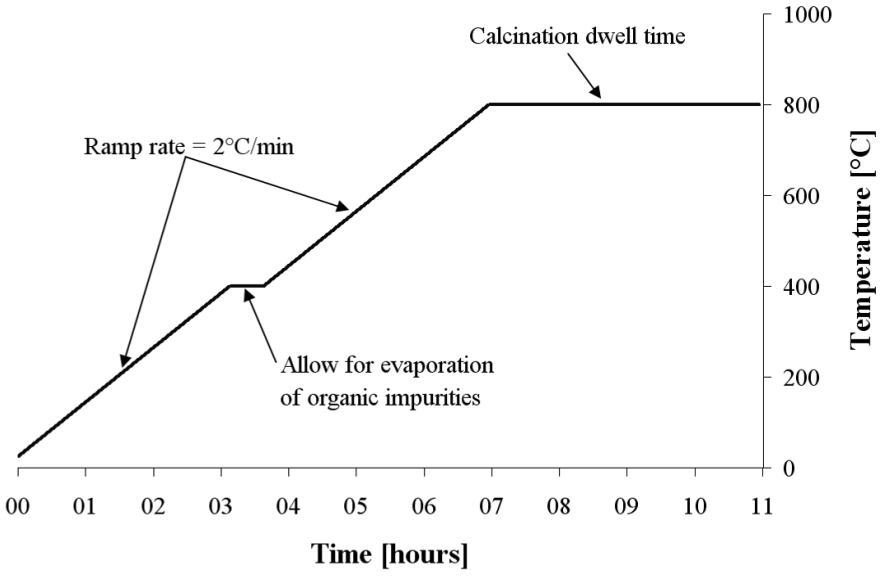

Figure 4-6 Calcination temperature profile used prior to sintering of bismuth titanate powders.

The adopted calcination regime temperature profile is shown in Figure 4-6. During the temperature increase from ambient to 400 °C, a linear expansion of particulates occurs and is accompanied by the loss of organic matter and moisture from the powder. A short dwell period at 400 °C allows for complete volatilisation of organics. Thermo-chemical reaction takes place between 400 °C and 800 °C during

which the main bulk of shrinkage occurs. Literature suggests that the ideal calcination temperature is a compromise between the temperature being high enough for all powder to react and low enough to prevent agglomeration or evaporation of oxides [38]. Calcination of BIT powders at temperatures above 820 °C produces a green powder stock which contains large amount of agglomerates due to the presence of bismuth oxide in the liquid phase. This also leads to evaporation and loss of bismuth oxide, albeit a small amount, and is in agreement with early phase characterisation of $Bi_4Ti_3O_{12}$ by Speranskaya et al. [100], where it was shown that bismuth oxide melts at 840 °C and a number of intermediate phases are identified. Subsequent refinement of this data by Bruton [101] has identified further intermediate phases which form a eutectic with bismuth oxide at melting temperature of 795 °C.

Experiments conducted by Shulman [72] have shown that with a ramp of 5 °C min^{-1} to 800 °C calcination regime, strong evidence of glassy phase was observed, indicating presence of melted bismuth oxide and an intermediate phase. A dwell of 1 hour at 600 °C prevented melting by allowing more coherent reaction of oxides.

During the present experiments, the ramp rate was reduced to 2 °C min^{-1} without a dwell period at 600 °C, and it was found that there was no evidence of glassy phases in the green powder. The optimum calcination temperature regime, as shown in Figure 4-6, was deduced by a series of calcination experiments at a range of temperatures. The green powder was then examined using X-Ray Diffraction (XRD) for the presence of intermediate phases.

Figure 4-7 shows the XRD data of BIT calcinated at a range of temperatures. The intermediate phase is evident at 600 °C and it is apparent that the major phase is formed above 700 °C. A calcination temperature of 800 °C was ultimately deemed appropriate, since it increases the rate of reaction but is below melting point of bismuth oxide. Calcination itself was carried out in a small alumina crucible, which was covered with an alumina plate and placed inside a programmable box furnace.

After calcination, powder had to be milled again as described in phase 1, dried and then graded using 38 μm mesh sieve.

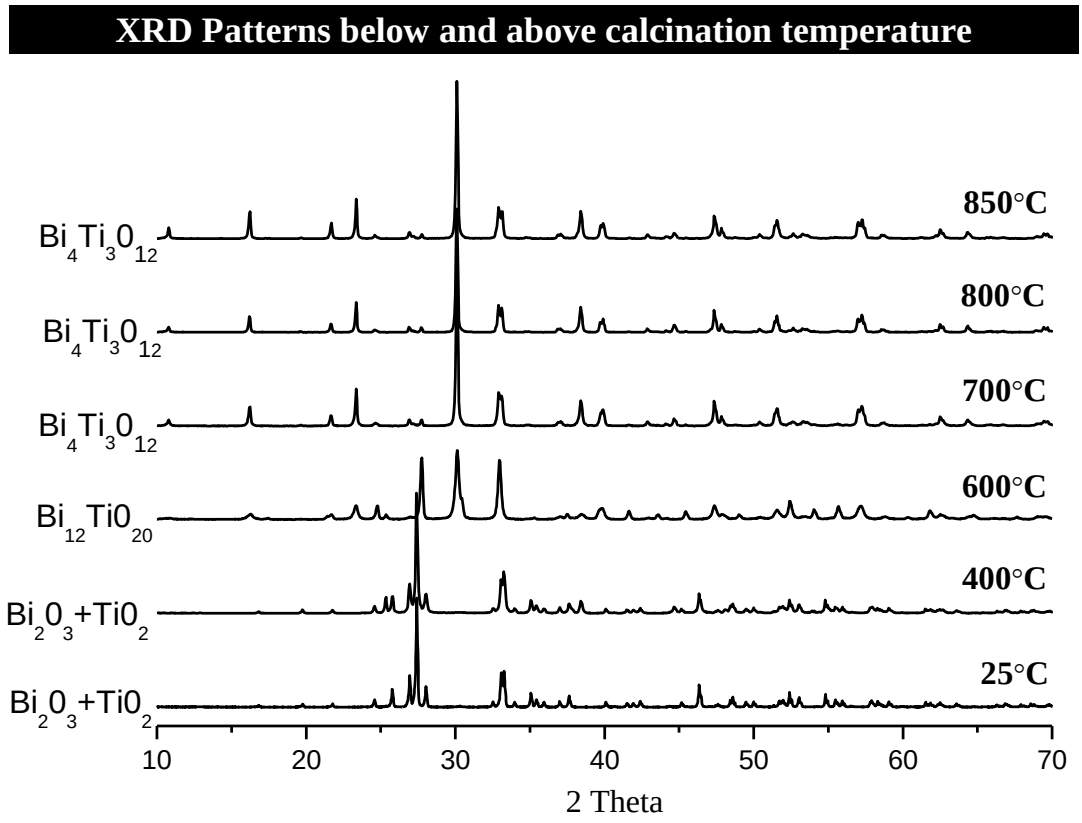

Figure 4-7 Phase formation XRD Data. The intermediate phase is evident at 600 °C and major phase can be seen forming above 700 °C.

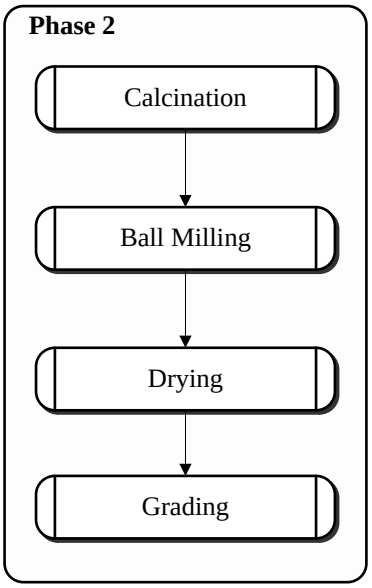

Figure 4-8 Phase 2 process steps for production of green BIT powder.

4.1.3. Phase 3: Forming

In this phase, the procedures for fabrication of a sample pellet are described and the steps of phase 3 are shown in Figure 4-9.
After grading in phase 2, the powder was then mixed with 5 wt% of polyvinyl alcohol (PVA) as a binder, to produce a pellet. Experiments carried out with a higher concentration of PVA showed increased porosity in finished samples while those which used lower concentration of PVA made pellets likely to fracture.

Each pellet, consisting of 2 to 4 g of powder stock, was loaded into an evacuable stainless steel die and pressed with 2 tons of pressure for 5 seconds in order to form a fracture free semi-solid pellet. The pellets were then vacuum sealed into a plastic bag and isostatically pressed to 200 MPa. This was followed by a heat treatment to release PVA binder prior to sintering. The ramp rate used during the binder release was 1 °C min^{-1} up to 500°C, followed by half hour dwell and natural cool down to room temperature.

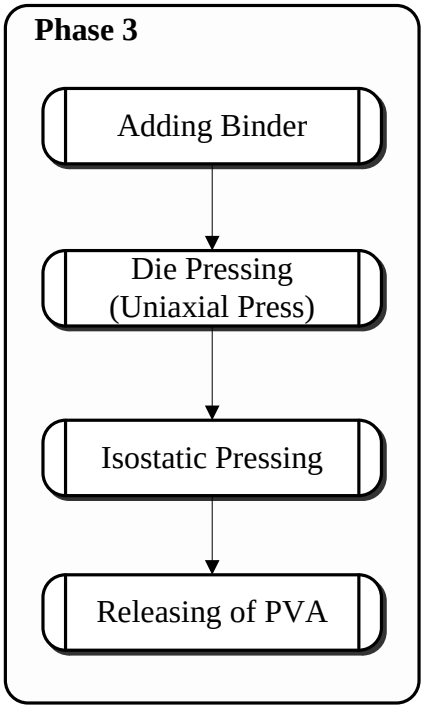

Figure 4-9 Phase 3 process steps for production of green pellets ready for sintering.

4.1.4. Phase 4: Solid State Sintering

Phase 4, solid state sintering, is the final part of the BIT ceramic preparation process. The solid state sintering principles are discussed at length by Rahaman [102] and Barsoum [103]. In present work, green pellets were placed on a platinum plate and covered with an alumina crucible. The sample was then sintered in a programmable box furnace. Figure 4-10 shows the temperature regime used for the process.

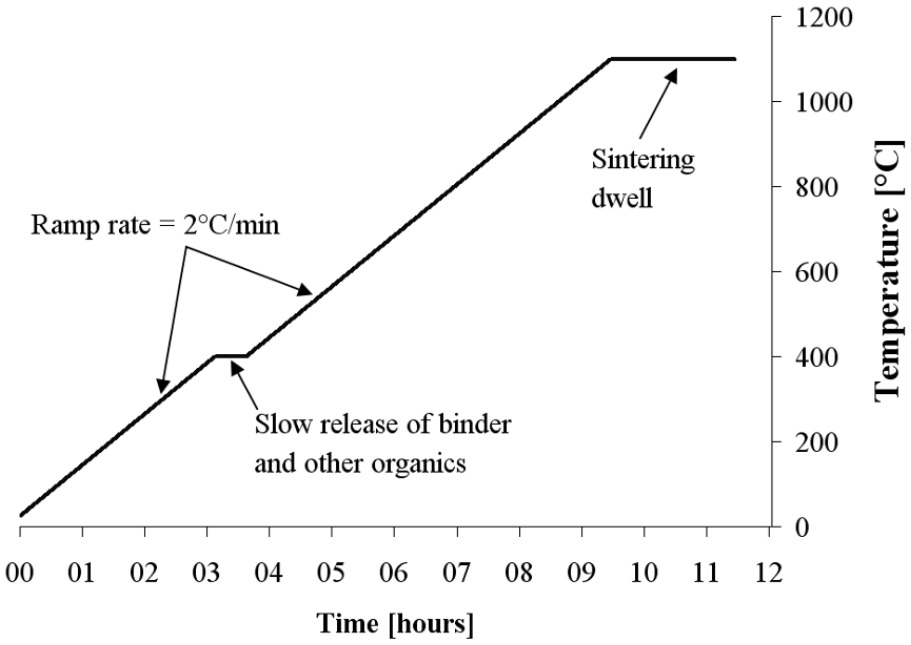

Figure 4-10 Sintering temperature regime utilised for production of high density BIT samples.

Pampuch [45] defines the sintering process as the phenomenon where fine powder grains form a dense polycrystalline structure as a result of being heated to an appropriately high temperature, below the melting point of the grains. The sintering process is accompanied by the loss of free energy due to migration and transport of grain centres, which decreases the volume of intergranular voids and therefore causing shrinkage in the bulk material. Rahaman [102] identifies three main factors in sintering and he refers to them as "driving forces for sintering". They are particle curvature, applied pressure and chemical reaction. According to Rahaman, particle curvature is the main driving force for sintering, where the applied pressure or chemical reaction is absent. The strength of the force is proportional to the free energy available in the system. This free energy can be calculated by first working out the number of particles N (considered as spheres) in one mole of powder.

$$N = \frac{3M}{4\pi a^3 \rho} = \frac{3V_m}{4\pi a^3} \qquad \textbf{Eq. 4-1 [102]}$$

where a is the particle radius, ρ is the particle density, M is the molecular weight and V_m is the molar volume. Having found the number of particles, the total surface area is therefore;

$$S_A = 4\pi a^2 N = \frac{3V_m}{a} \qquad \textbf{Eq. 4-2 [102]}$$

By introducing the specific surface energy of particles, γ, into the above equation, then the free surface energy is;

$$E_S = \frac{3\gamma V_m}{a} \qquad \textbf{Eq. 4-3 [102]}$$

The total free energy, E_S, is the energy that needs to be dissipated in order to produce a fully dense material. For ceramic manufacture from powders, the particle curvature always contributes to the driving force for sintering.

However, with the addition of applied pressure, the particle curvature contribution becomes less significant and the majority of work done is due to external pressure. The magnitude of the work done can be approximated by

$$W = pV_m \qquad \textbf{Eq. 4-4}$$

where p is the applied pressure and V_m is the molar volume. The effects of external pressure and its influence on densification is particularly exploited by hot pressing and other similar, pressure assisted sintering methods [66, 103, 104].

Chemical reaction has the potential to produce a larger driving force than that of applied pressure. However, it can be said that sintering and densification process is influenced by cumulative action of all three factors.

Figure 4-11 shows a simplified overview of the transport mechanism during solid state sintering.

During the sintering cycle, the ramp rate is kept relatively low at 2 °C per minute and is interrupted by a half hour dwell at 400 °C. It was found experimentally that the dwell period reduced the risk of sample fracture during densification. The final sintering temperature was varied between 1050 °C and 1150 °C depending on composition.

A two hour sintering dwell allowed for grain growth and densification before a slow cool down period to room temperature. Solid state sintering in air results in a polyceramic which is generally formed with randomly oriented grains and with no specific physical definition in terms of shape or axial alignment. A number of literature sources report improvements in densification and material properties of piezoelectric ceramics using hot press sintering [65-67] and spark plasma sintering methods [58, 59, 62, 63, 70].

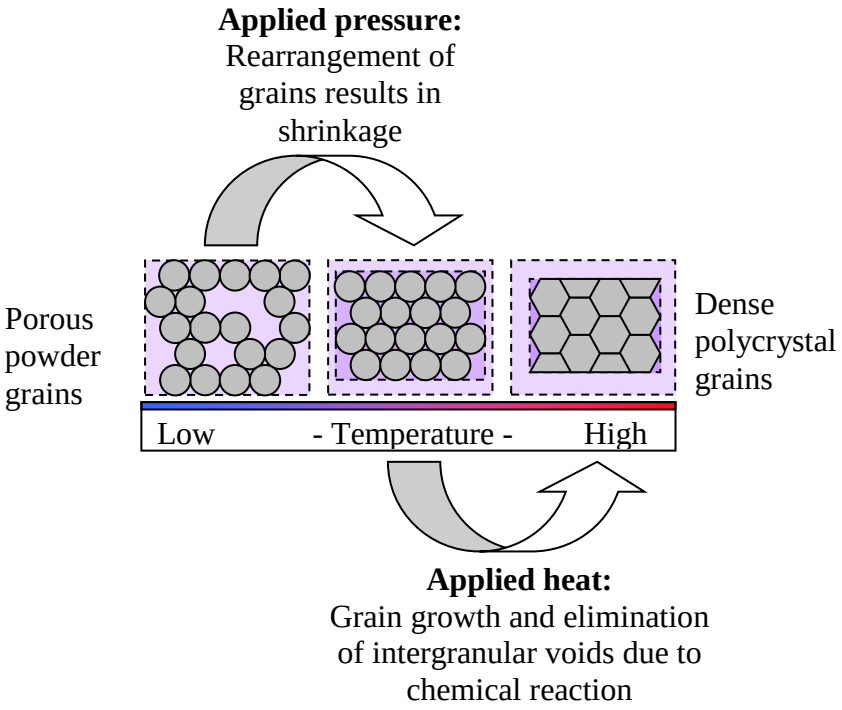

Figure 4-11 General principle of sintering and densification. The diagram shows loose powder particles on the left. By application of heat and pressure, a solid state reaction takes place and an accumulative driving force for sintering induces densification.

4.1.4.1. Hot-Press Sintering

The hot-press sintering process is a relatively high cost option for manufacturing materials where extremely high densities are not an absolute requirement. However, it is commonly employed for investigations into density or texturing studies.

Key advantage of hot-press sintering is the significant increase in densification rate, which in turn reduces the sintering time and hence suppresses the grain growth. Because of the higher densification rate, the sintering temperature can also be reduced, and in the case of bismuth titanate, this results in lower losses of bismuth due to volatilisation.

Other than high cost, there are several disadvantages with using the hot-press sintering method. The high density graphite used for manufacture of hot-press dies is a fairly loose material and tends to contaminate the sample powder leading to higher porosity. Rahaman [102] suggests hot-pressing of ready-compacted pellets which are then packed with alumina powder into the die, in order to buffer the sample from intimate contact with its walls. This solution also addresses the issue of sample fracture during sintering caused by excessive uniaxial pressure. The fine packing powder is able to flow freely around the pellet, distributing the applied pressure around the sample surfaces.

In the present work, hot-press sintering was conducted using a vacuum furnace with an induction heating system and also incorporating a hydraulic ram for the application of pressure to the sample. A high density graphite die was designed and manufactured for this purpose and its construction is shown in Figure 4-12.

High density graphite is a choice material for this type of application having very good compression strength, low coefficient of thermal expansion and is of course conductive, which makes it a key in induction heating. Due to increasing graphite oxidisation above 450 °C, sintering experiments had to be conducted in vacuum, and all die surfaces were coated with boron nitride which acted as the release agent [102].

A similar method for manufacturing hot pressed ceramics is described by M. R. Holdsworth in a US patent [104].

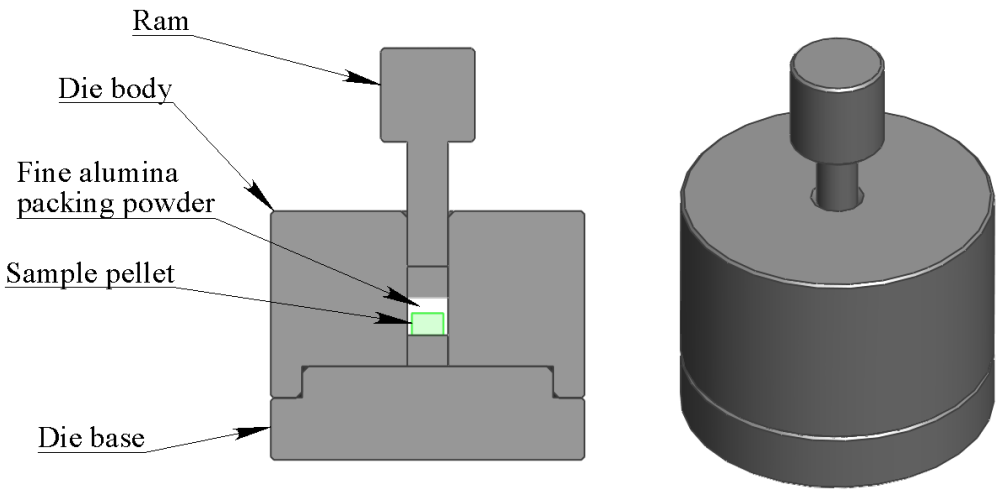

Figure 4-12 Cross section of a hot-press die fabricated from high density graphite. It shows the sample pellet packed with fine grain alumina powder for more even pressure distribution in order to reduce the risk of sample fracture. To prevent sample ceramic reacting with graphite, the die was coated with a thin layer of boron nitride.

4.1.4.2. Spark Plasma Sintering

Spark plasma sintering (SPS) is a promising but relatively underutilised form of pressure assisted sintering where a DC current of several kA in magnitude, is passed through the green sample and a suitable graphite die, whilst applying pressure of up to 100 MPa. This generates a large amount of heat in the sample. The heating mechanism is not fully understood at present although it is suggested that heat is generated by spark discharges generated in the voids between the green particles [102]. Phenomenally high heating rates are possible with this technology and ramp rates between 600 and 1000 °C min^{-1} are reported [105].

According to Orru et al. [106], for conducting green powders the current is passed straight through the sample itself and the heat is generated by the Joule effect in the sample and the die. For non-conducting powders, such as bismuth titanate, the sample is heated only by thermal conduction from the die, and for this reason the die has to be electrically conductive of course. It can be argued that in the present application, the heating is purely due to the Joule effect in the die and not due to sparking or plasma formation. This feature of the SPS process raises a problem associated with conductivity of samples and dies in that the current distribution has to be homogeneous in order to avoid excessive localised overheating and melting of the sample powder. This limits the process to simple and uniform geometrical shapes. Closed loop temperature control is typically implemented by using a thermocouple or a pyrometer as a temperature feedback sensor and DC current as a control variable.

For the research described here on bismuth titanate the spark plasma sintering furnace, Dr. Sinter 2050 manufactured by Sumitomo Coal Mining Co.[3] was kindly provided for the project by Queen Mary University London. A high density graphite die having diameter of 12 mm was used for all experiments and it was lined by a graphite shim of 0.3 mm thickness, obtained under its commercial name of Papyex® (N998). Green powders were sintered in the form of a disk having a thickness of 2 to 3 mm and with

[3] SPS kindly made available by Prof. M. Reece and run by his team at Nanoforce Technology (Queen Mary University London)

an applied pressure in the range between 15 to 30 kN. The sintering temperature was between 900 and 1000 °C, significantly lower than that used in conventional, mixed oxide sintering, which is typically above 1100 °C. Figure 4-13 shows the simplified schematic diagram of an SPS setup, and process variables during typical procedure are given in Figure 4-14

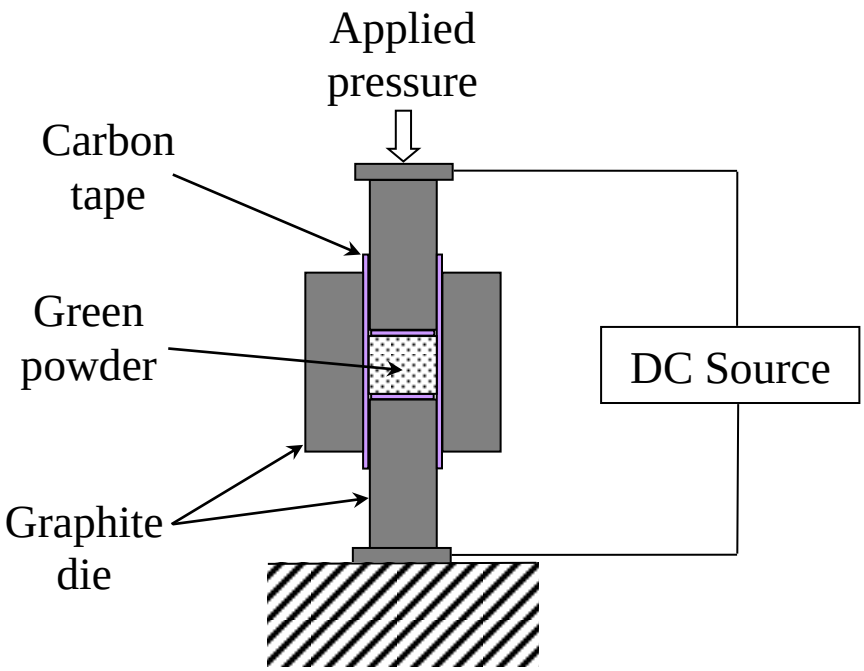

Figure 4-13 Schematic representation of spark plasma sintering or SPS furnace. Thin sheets of carbon paper are used to isolate green powder from the direct contact with the graphite die.

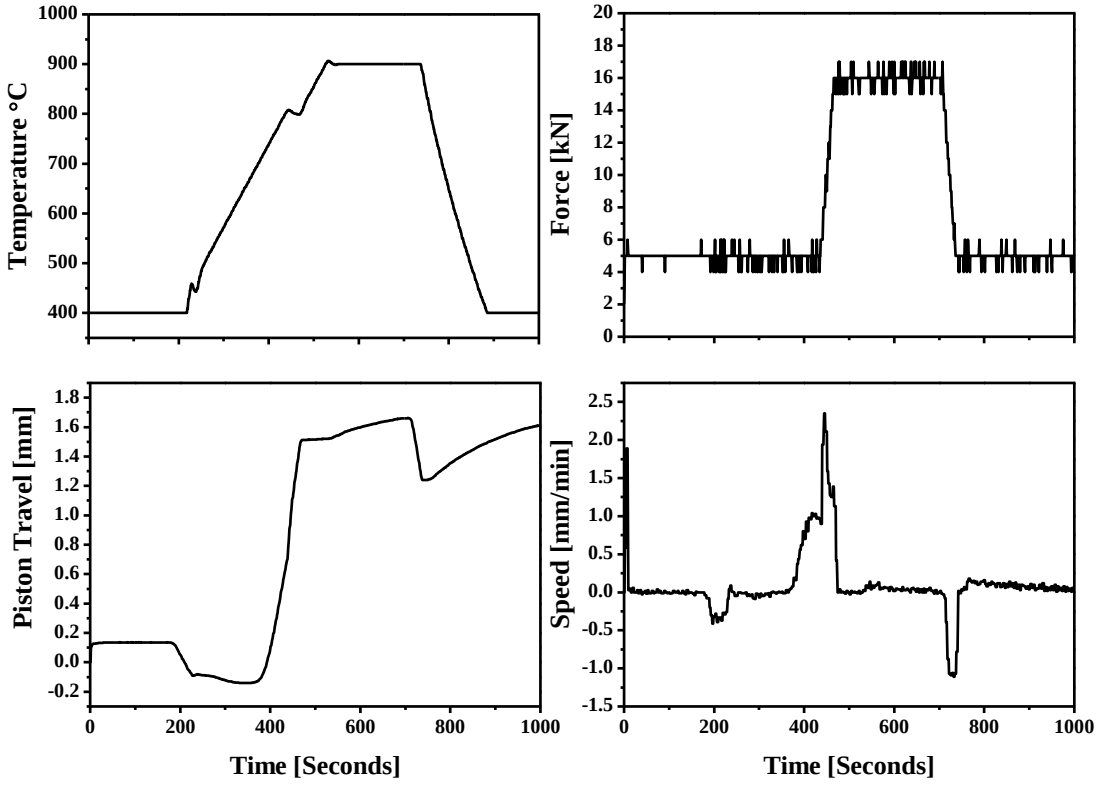

Figure 4-14 Typical SPS experiment data. Temperature trace shows a rolling start from a 400 °C dwell, allowing for evaporation of moisture and organics prior to densification ramp.

4.2. Characterisation of Piezoelectric Ceramics

4.2.1. Electron Microscopy and Energy Dispersive X-Ray Spectroscopy

Scanning electron microscopy or SEM is a material characterisation technique generally employed to observe surface features of sample material at high resolution [107]. High resolution images are obtained by using a secondary electron (SE) imaging detector, whilst chemical phase distribution analysis is performed with back-scattered electron (BE) imaging detector.

In the present work, qualitative and quantitative chemical analysis was performed using energy dispersive X-ray spectroscopy or EDS analyser (ISIS 300), fitted to a JEOL 5800 LV SEM. Depending on availability, JEOL 6340 FEG was also used.

Acceleration voltages from 10 kV to 20 kV were typical, with working distance of 10 to 15 mm. Solid samples were lapped with 800 grit SiC paper and then thermally etched at 1000 °C for 10 minutes, in order to reveal surface morphology. To avoid fracture of samples during etching, the temperature ramp rate was kept low at 2 °C per minute. Samples were then mounted on an aluminium sample holding stub using double sided carbon loaded adhesive tape and sputter coated with gold or platinum for 3 minutes under current of 20 mA or 40 mA respectively. For powders, an aluminium stub, having a conductive, double sided sticky tape applied to one side, was pressed into the powder in order for particles to adhere to the surface and was then sputtered as described earlier.

4.2.2. X-ray Diffraction Analysis

X-ray diffraction or XRD is a non-destructive characterisation method for powders or solids, used for identification of crystalline phases [80]. Phillips PW3050 and Bruker D8 (theta/theta) X-ray diffractometers were used to analyse crystallographic phases of BIT powders.

X-ray beam, having a high energy and short wavelength, penetrates the surface of the sample material whose atomic planes act as a diffraction grating. The incident beam is therefore diffracted at characteristic angles, representative of materials crystallographic structure according to Bragg's law;

$$n \times \lambda = 2 \times d_{hkl} \times \sin\theta \qquad \textbf{Eq. 4-5 [51]}$$

where n is the order of reflection (always an integer),

λ is the wavelength of the X-ray source,

d_{hkl} is the lattice plane spacing,

θ is the subtended angle between incident and diffracted beam.

The λ value for Cu K_α radiation is 1.54 Å (154 pm). The X-ray diffraction spectra were typically acquired over the range 10 to 90° at 0.05° step size and a dwell time of 2 seconds. Data was analysed using Phillips Xpert software.

The main limitation of this technique and equipment combination is that phases with very low concentration could not be easily detected due to the very low signal intensities produced.

4.2.3. Thermal Analysis

Thermal gravimetric analysis (TGA) is a characterisation technique in which the weight change of the sample is measured as a function of temperature. Differential scanning calorimetry (DSC) is another technique in which the heat loss from the sample is measured and compared to an inert reference (alumina), in order to identify endothermic or exothermic reactions taking place in the sample material.

In the present work TGA and DSC were carried out simultaneously using a TA Instruments SDT Q600 in inert atmosphere (argon). Figure 4-15 shows the main measurement mechanism.

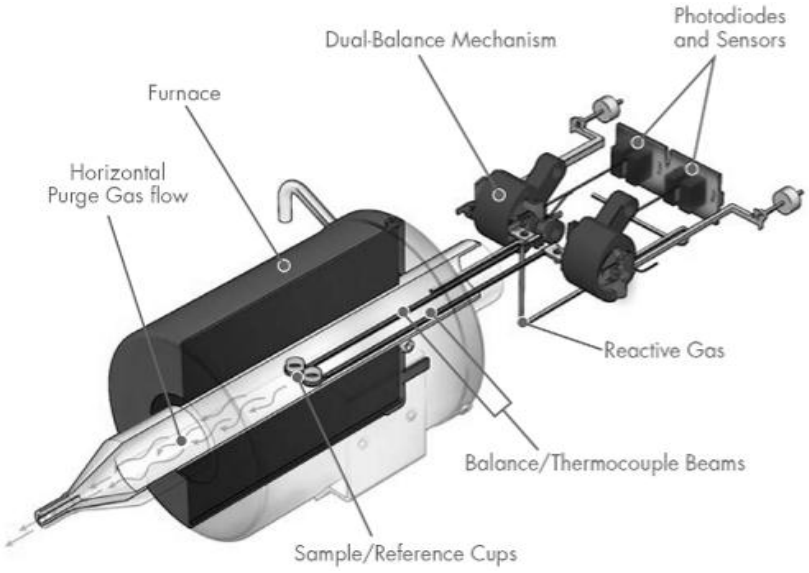

Figure 4-15 Diagram showing the construction of the main measurement mechanism on the SDT Q600. The weight of the sample is continuously measured against the reference cup using a microbalance, whilst the sample temperature is acquired by means of a small thermocouple positioned by the sample. Reproduced from TA Instruments marketing literature [108].

4.2.4. Density

The density of the ceramic samples was experimentally determined by implementing Archimedes principle [109]. All samples were weighed using a Sartorius AC120 S laboratory balance, under three specific conditions in order to get dry (*Wd*), suspended (*Ws*) and wet (*Ww*) sample weights. In the first instance the sample was placed inside a drying oven at 120 °C and once dry, it was weighed to obtain *Wd*. The sample was then submerged into distilled water and placed inside a glass vacuum chamber which was then evacuated until formation of bubbles on the surface of the sample had stopped, indicating sample pores being full of water. The sample was then weighed whilst suspended in distilled water, the temperature of which was measured, to obtain the *Ws* weight. Finally, the sample was removed from water and all surface water was removed, after which the final weight was taken; *Ww*. Density of sample is given by;

Bulk density; $$\rho = \frac{Wd}{Ww - Ws} \times \rho_w$$ **Eq. 4-6 [109]**

where ρ is the density of the sample and ρ_w is the density of water. The porosity of the sample is calculated using equation;

$$\frac{Ww - Wd}{Ww - Ws} \times 100$$ **Eq. 4-7 [110]**

This gives the percentage of open pores in the sample. Because of relatively simple geometry, the sample density could also be calculated using dimensions of the dry pellet, and the equation;

$$\rho = \frac{Wd}{\pi \times r^2 \times l}$$ **Eq. 4-8 [111]**

Where *r* is the sample radius and *l* is the sample thickness. Main sources of error in this method come from balance accuracy.

The error in density measurement was calculated using the standard method given by Skoog *et al*. [112] and found to be less than 0.2 %.

4.2.5. Particle Sizing

Particle sizing was performed on a Malvern P580 Mastersizer/E which analyses particle size distribution using forward light scatter of the incident laser beam. During the procedure, particles suspended in ethanol at a concentration of 1 wt% were mechanically agitated to ensure adequate distribution of particle and the measurement was made by 32 concentric ring detectors, measuring the angle of diffraction and averaging over a 10 minute period.

4.2.6. Dilatometry

Dilatometry is a material characterisation technique in which the length of a solid sample is measured as a function of temperature. A Netzsch DIL 402 push rod dilatometer was used primarily to evaluate the shrinkage of green sample during sintering and also to investigate thermal expansion properties of sintered BIT material.

4.2.7. Piezoelectric Characterisation

The characterisation of piezoelectric properties were carried out on fully sintered pellets which were lapped to required thickness and provided with adequate electrodes on two adjacent surfaces. Sintered pellets, having typical diameter of 10 to 13 mm, were lapped between 0.4 and 0.5 mm thickness using 1200 grit SiC paper. A silver electrode was then applied to one side of the clean and dry sample by means of silk screen process in order to achieve a uniform coat, after which the sample was fired at 750 °C with the ramp rate of 1 °C min^{-1}, and half hour dwell periods at 300 °C and 750 °C. The silver paste was then applied to the other side of the sample, followed by firing at 800 °C with respective dwell periods to reduce the risk of sample fracture.

Silver paste type 9912-A from ESL Europe was used and it was found experimentally that the procedure described previously produces good electrode adhesion, with good tolerance to standard soldering methods.

Ferroelectric bismuth titanate was then polarised based on methods reported in literature [38, 47, 49, 54, 80]. Polarisation of samples was carried out using a poling rig assembled at the department of Material Science and Metallurgy (University of Cambridge), which consisted of a temperature controlled oil bath filled with Dow Corning 210H high temperature fluid. The oil was required to ensure even temperature distribution and also to prevent corona discharge during the presence of a HT field. It was initially found that thermostatic temperature control on the rig produced ±30 °C of hysteresis which influenced the results. The system was improved by disabling thermostatic controls and replacing it with a digital temperature controller (Eurotherm), which provided temperature stability of ±0.5 °C and was considered adequate.

During the polarisation procedure, the sample pellet was held in a polarisation cell, fabricated from brass and PTFE materials, and was submerged under the heated oil.

Diagram in Figure 4-16 shows the construction of the polarisation cell. The samples were first allowed to stabilise at a polarisation temperature of 200 °C (typical), and the field would then be gradually applied. After 15 minutes under applied HT field, the temperature control was switched off allowing the oil to cool down slowly, whilst the field was maintained until the oil temperature dropped to below 120 °C. The amplitude of field that could be safely applied without damaging the sample varied with sample density. Typical values were between 40 and 80 kV cm^{-1}. The polarisation voltage was supplied by a 5 kV, reversible polarity power supply, constructed at the Material Science and Metallurgy department (University of Cambridge).

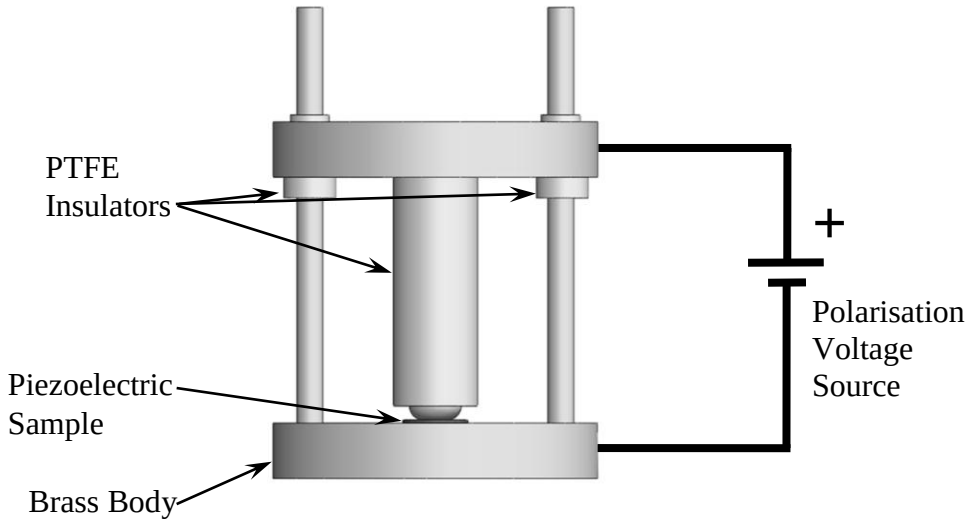

Figure 4-16 Piezoelectric pellet polarisation cell which allowed samples to be dipped into hot oil and a polarisation voltage to be applied simultaneously. The sample, having the bottom electrode in contact with the brass body, is positioned so that the ram is gently pushed against the top electrode. The polarisation voltage is applied through the ram and the base of the polarisation cell, to the sample.

4.2.7.1. Piezoelectric Coefficient

The piezoelectric charge coefficient (d_{33}) was measured by a quasi-static (dynamic) method as described in reference standards [113, 114] using a Berlincourt type d_{33} meter, manufactured by Sinoceramics Inc. and distributed under a trade name "d_{33} Calibrator". The principle of operation is that a low frequency (110 Hz) sinusoidal force of 0.25 N is applied to the sample, whilst the charge generated on electrodes is analysed. The instrument was specified to have ±2 % accuracy for the applied range and all data given in present work is subject to this error.

A calibration procedure was carried out prior to every use, according to instructions and using the reference sample provided by the manufacturer. Another small source of error with this measurement method was identified by Erhart and Burianova [115] as the position and alignment of the jaws with respect to sample geometry. These errors were mitigated by careful positioning of the jaws in the centre of the sample during measurement. Furthermore, the critical aspect ratio of 2:1 (min), defined by the IEEE standard [113] was observed for all samples.

4.2.7.2. Impedance Spectroscopy

Resonant and AC properties of piezo-ceramic samples and ultrasonic transducers were investigated via impedance spectroscopy technique using a Solartron 1260 impedance gain/phase analyser. The general principle followed is that the instrument applies a sinusoidally varying electric field of 1 V across the device under test and impedance is calculated based on the magnitude and phase angle of the current measurements.

Measurements were performed at a range of frequencies and temperatures, using four probe topology in order to reduce the influence of connecting leads on the final measurement, and data was collected using Zplot® software.

Real and imaginary permittivity of material was then calculated from impedance data using relationships;

$$\varepsilon' = \frac{-Z''}{\omega C_o \left(Z'^2 + Z''^2\right)} \quad \text{Re.} \qquad \textbf{Eq. 4-9}$$

$$\varepsilon'' = \frac{Z'}{\omega C_o \left(Z'^2 + Z''^2\right)} \quad \text{Im.} \qquad \textbf{Eq. 4-10}$$

Where ω is the angular frequency, C_0 is the static capacitance and Z' and Z'' are the real and imaginary impedance respectively.

The theory behind the impedance measurement is explained thoroughly by Bauerle [116] in his paper on characterisation of solid electrolyte. The author uses complex admittance plots to build an electrical RC model representing the response of the material. This approach was followed in the present research.

4.2.7.3. Hysteresis

Ferroelectric hysteresis of the material was characterised using a method based on Sawyer Tower bridge. The test setup is shown in Figure 4-17.
The frequency was controlled using a programmable function generator, which fed into a 100 W audio amplifier at the frequency of up to 4 kHz. To avoid large temperature change in the sample due to losses, the AC field was applied in bursts of 20 cycles. For hysteresis measurements at elevated temperatures, the sample was suspended in a beaker of high temperature silicone oil and heated on a hotplate.

It was found that for some experiments, the coercive field required to saturate BIT samples could not be achieved and the apparatus therefore had limited use.

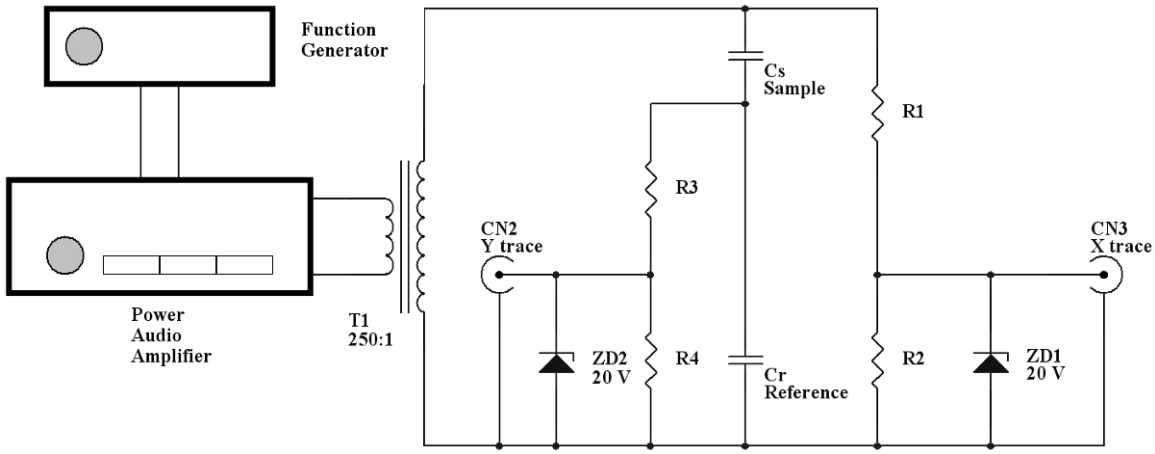

Figure 4-17 Ferroelectric hysteresis measurement setup based on classic Sawyer Tower bridge [114, 117].

Chapter 5 Modified Bismuth Titanate for High Temperature Sensor Applications

5.1. Introduction

It has been shown in previous chapters that bismuth titanate had recently enjoyed a surge in interest from the scientific community. However, keeping the motives for present research in focus, it is important that this fascinating material finds its way from the laboratory and into various industrial applications, as a viable alternative to lead based products. BIT demonstrates good overall properties and a potential for significant improvement in piezoelectric coefficient, whilst preserving high Curie temperature. It is the aim of this chapter to investigate the means of optimising the morphology and electrical properties of BIT through improvements in processing methods and structural modification via donor doping.

Consistency of the sample quality is the key to developing piezoelectric material and enhancing its properties, so a deeper understanding of processing variables and their influences on final properties is sought. The approach presented in this section was to enhance the sintering conditions by studying morphology of the material and also to investigate the effects of impurities introduced by the processing techniques.

Initially, the preparation procedures of green powders are investigated and sources of contamination and their influence on final densities are identified. The temperature profile of the sintering cycle is then optimised, taking into consideration loss of bismuth oxide at elevated temperature as a potential factor for lowering the density of the finished ceramic [118].

In a further exploration of density enhancement, some experimental data from hot press and SPS sintering experiments is presented.

Published literature suggests significant potential for improvement in piezoelectric properties of bismuth titanate, both in terms of inclusion of doping elements and in refinement of processing methods [69, 70, 72, 119]. It is well known that high conductivity in bismuth titanate is a major obstacle during polarisation of the ceramic [72], forcing significant reduction in the magnitude of the poling field and hence lowering the ultimate piezoelectric charge coefficient that can be achieved. In addition to this, electrical conductivity is a significant contributor to the accelerated ageing rate in piezoelectric ceramics due to induced charge drift and gradual reduction of electrical domain alignment [120]. It was postulated that application of a multi-doping (MD) strategy to target specific characteristics of BIT would result in a novel piezoelectric material with properties enhanced to suit ultrasonic sensor application.

5.2. Processing Routes for High Density Bismuth Titanate

5.2.1. Green Powder Processing

A detailed explanation of the powder preparation procedure was discussed in chapter 4. Initial experiments with production of green BIT powders were conducted according to literature references for mixed oxide preparation procedure [45, 102]. Full review of this procedure was carried out in order to identify areas where improvements could be made to minimise the risk of sample inconsistency in terms of ceramic density and characteristic properties.

The first potential cause of variation in sample properties was identified as a loss of raw powder during weighing and handling prior to calcination. This was particularly critical for doping elements due to their rather small mass ratio in comparison to mass of bismuth and titanium oxides. The procedure was improved by weighing all powders in the same weighing boat and ensuring that doping elements were always added last, and hence no powder is left behind after transfer to the milling container. This small practical change has shown more consistent powder characteristics.

Influence of sintering temperature on ceramic density was evaluated by sintering samples of pure bismuth titanate at 1050 °C, 1075 °C, 1100 °C and 1125 °C. Sintered samples were polished and thermally etched in order to expose surface grain structure of the material in preparation for SEM characterization of morphology. Figure 5-1 shows the surface morphology features of pure BIT samples.

The evaluation of images suggests that the average grain size increases with sintering temperature, whilst the material becomes more porous. Figure 5-2 shows the relative densities of uniaxially and isostatically pressed pellets at various sintering temperatures. Density measurements indicate that the maximum density of 95 % for pure BIT composition was realized with sintering temperature of 1100 °C, however the sample was still relatively porous, possibly due to low uniaxial pressure applied to

the sample during forming. In a drive to reduce the porosity and increase density, uniaxially pressed pellets were isostatically pressed with 200 MPa. As a result, a noticeable improvement in density to 97 % was observed.

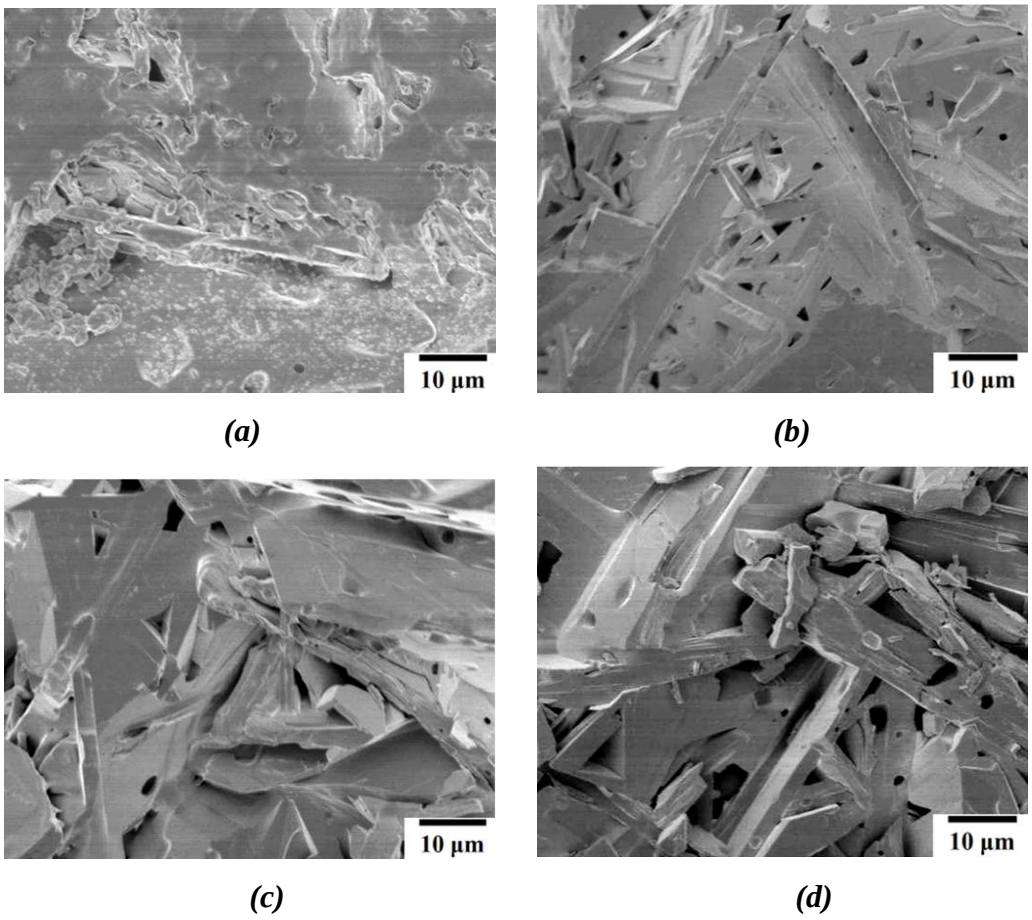

Figure 5-1 SEM patterns of pure bismuth titanate sintered at: a) 1050 °C, b) 1075 °C , c) 1100 °C and d) 1125 °C. Influence of sintering temperature on grain growth can be observed.

This improvement can be attributed to application of pressure, more intimate arrangement of BIT particles and the increase in contribution from residual pressure as a driving force for sintering. At temperatures greater than 1100 °C, abnormal grain growth can be observed resulting in poorer sintering.

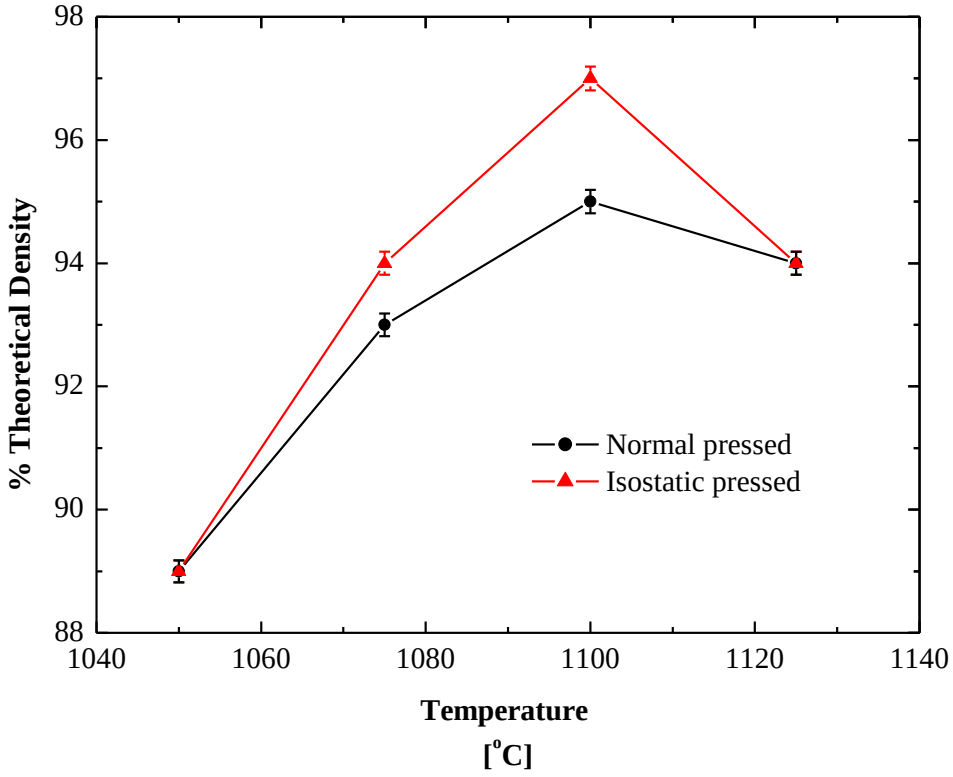

Figure 5-2 Relative sample densities for normal and isostatically pressed ceramic sintered at 1050°C, 1075°C, 1100°C and 1125°C. 2 % improvement in density can be noted at optimum sintering conditions.

These initial findings also suggested that inconsistencies in density and general properties of the material from batch to batch could also be attributed to variations in basic composition of the powder. Two main sources of contamination were identified as purity of raw powders and process contamination.

It has been shown in the literature that the impurities in raw materials have a significant influence on the properties of doped bismuth titanate [72]. Taking this into account and accepting that raw material impurities will always be present in small quantities, it can be said that by using the same batch of starting powder, the end product will be consistent and can therefore be used as a benchmark to aid qualitative assessment of BIT properties. The introduction of impurities during processing of raw materials did however introduce a degree of variability into sources of contamination, and of particular interest was the high energy ball milling of powders. Ball milling of powders was conducted using alumina milling balls and it was noted that the condition and appearance of the milling balls changed significantly on the first and subsequent use, indicating a change in surface texture and hence material loss and homogenisation with the BIT powder during ball milling. Distributed alumina grains within the BIT polycrystal introduce structural defects and variation in conductivity, thereby reducing the breakdown strength and impeding the polarisation process.

To investigate the effects of Al_2O_3 contamination on BIT properties, alumina milling balls were replaced with zirconia, which were pre-conditioned in ethanol on a roll mill for 72 hours prior to use. Calcinated BIT powder samples were then mixed with 0.5, 1.0 and 1.5 wt% of fine grain alumina powder (0.2 µm average grain size), and placed on a roll mill for 72 hours. After shaping and isostatic pressing, samples were sintered at 1050 °C, 1075 °C, 1100 °C and 1125 °C. The XRD data of samples sintered at 1100 °C is shown in Figure 5-3. Formation of $Bi_4Ti_3O_{12}$ phase does not seem to be inhibited by the varying concentration of Al_2O_3, suggesting that the concentration of Al_2O_3 is dispersed at the grain boundaries of BIT crystals. Due to the very low concentration, the presence of isolated alumina is not detectable with the XRD method.

Figure 5-4 shows the XRD pattern of Al-BIT polyceramic sintered at 1050, 1075, 1100 and 1125 °C. Maximum density is achieved at 1100 °C, which is slightly higher temperature than that reported for pure BIT [72].

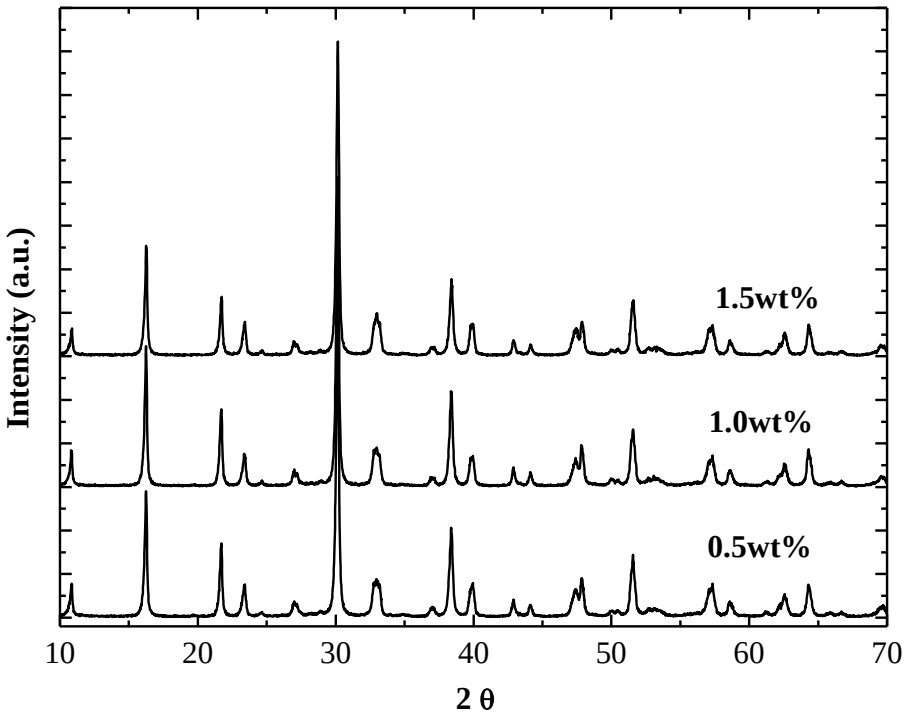

Figure 5-3 XRD data shows consistent powder patterns for all three concentrations of alumina. This indicates no influence on crystal structure and isolated alumina is below the detectable threshold for XRD.

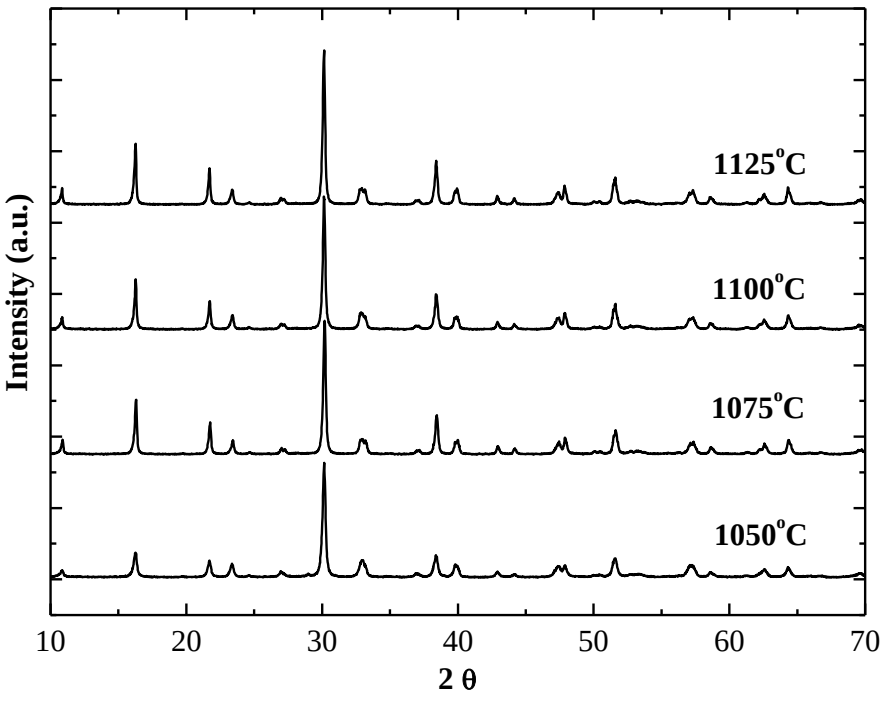

Figure 5-4 XRD patterns of Al-BIT sintered at different temperatures. Highest density is achieved at 1100 °C.

Figure 5-5 shows a distinct influence by the alumina concentration on density of BIT ceramic, exhibiting a peak density of 99 % at 0.5 wt% alumina and sintering temperature of 1100 °C. This data indicates that for a small concentration of alumina powder, optimised packing conditions can be achieved and the alumina grains are dispersed along the BIT grain boundaries, filling in what otherwise would be intergranular voids. As the concentration of alumina increases, the BIT grains are displaced and the sample volume is increased.

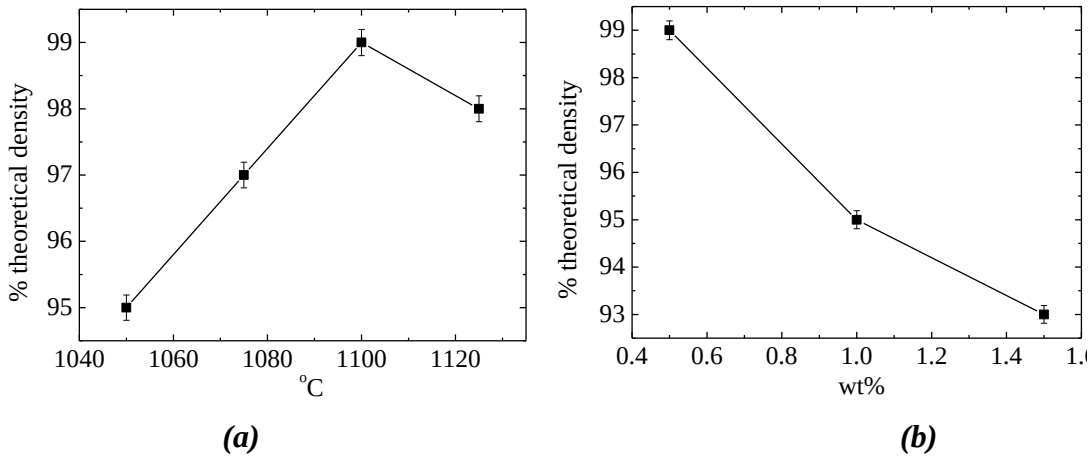

Figure 5-5 Densities of Al-BIT samples sintered at various temperatures. (a) various temperatures for 0.5 wt% Al-BIT samples, (b) different concentration of alumina.

Addition of Al_2O_3 into the BIT polycrystal had a negative effect on the sample polarisability. Reduced dielectric strength of the sample meant that only weak electric fields of up to 10 kV cm^{-1} could be applied and therefore the piezoelectric coefficient was typically lower than expected for pure BIT.

Alumina balls were subsequently replaced with zirconia, which has significantly higher fracture toughness and better wear resistance. This has shown more consistent properties in BIT.

5.2.2. Pressure Assisted Sintering

Two forms of pressure assisted sintering were experimented with in order to increase the density of the BIT samples: hot press sintering (HPS) and spark plasma sintering (SPS). Both fabrication methods are described in more detail in section 4.1.4.

Hot press sintering experiments were carried out at the Department of Material Science and Metallurgy (University of Cambridge) using a Radyne vacuum furnace fitted with a hydraulic ram and induction heating coil.
HPS experiments were found to produce inconsistent results and poor sample quality. Although regions of high density were observed, voids caused by graphite contamination from the die generally introduced a large number of holes and fissures in the sample body. In order to protect the graphite die from volatilisation at high temperature the chamber had to be kept evacuated so the cooling rates were very slow. This prolonged dwell at temperature above 900 °C induced an undesired and uncontrolled grain growth. Figure 5-6 shows SEM images of the HPS BIT samples.

A crude system for application of pressure meant that sample fracture was common and often; structural issues would only be revealed after the sample was cut. Having identified the issues with the processing method, further evaluation and optimisation of the experimental setup and procedure was required in order to produce a more reliable ceramic sample. This technique was perceived to be unreliable to implement with the current experimental setup and an alternative method was sought.

Presently only a limited number of SPS experiments have been carried out which show good improvement in material density and promising d_{33} characteristics. Due to time constraints on the project, further SPS experiments will be carried out in the next stage as part of the EPSRC PhD Plus program and in collaboration with Nanoforce Technology Ltd (Queen Mary, of University London).

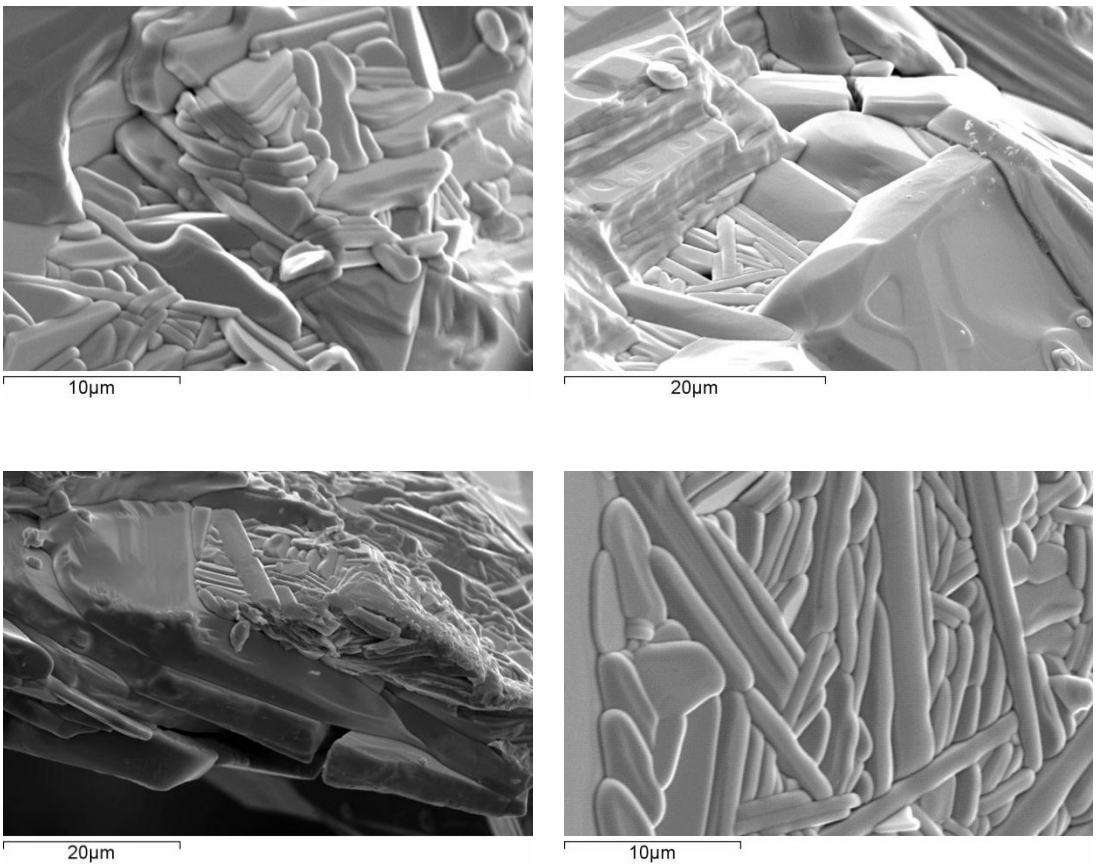

Figure 5-6 SEM images of 4 HPS BIT samples. Although relatively low porosity can be observed, variation and inconsistency in grain size is evident.

5.3. Electrical Characteristics of Bismuth Titanate ($Bi_4Ti_3O_{12}$)

Impedance analysis is generally used for investigation of dielectric material properties in frequency domain. It is a technique based on voltage and current phase analysis; polarisation and relaxation of the dielectric material under test. As a result, it is generally expressed as a complex number where the real part represents the resistance, and the imaginary part is the reactance of the sample at a particular frequency.

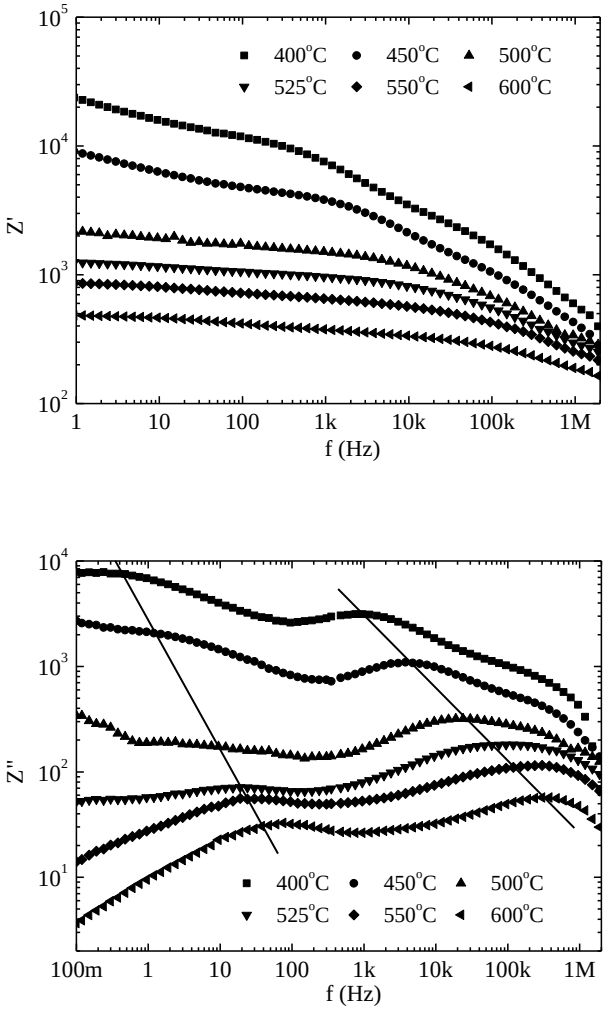

Figure 5-7 Real (Z') and imaginary (Z") impedance plots vs. frequency at a range of temperatures.

Figure 5-7 shows plots of real and imaginary impedance up to 1 MHz at a range of temperatures. It is shown that the value of *Z'* decreases with increase in frequency, and based on Eq. 5-4, this can be attributed to rise in AC conductivity. The influence of temperature diminishes at higher frequencies, which also reflects on the values of the imaginary impedance *Z''*, also shown in Figure 5-7. Two relaxation peaks are evident (marked with straight lines) and they are shown to shift to higher frequencies at higher temperature, exhibiting typical electrical relaxation behaviour which can be attributed to the presence of defect vacancies.

Complex permittivity (ε*) of the material is typically used in the literature to describe material characteristics against a time varying electric field, and is given by;

$$\varepsilon^*(\omega) = \varepsilon'(\omega) + j\varepsilon''(\omega) \qquad \textbf{Eq. 5-1 [71]}$$

where real and imaginary parts are storage and loss, or dielectric polarisation and relaxation components respectively. Figure 5-8 shows the real and imaginary permittivity for pure BIT samples. It can be seen that the permittivity falls off as a function of frequency, demonstrating increasing phase lag between the alternating field and the polarisation of the material. Only marginal temperature influence on permittivity can be observed due to permanent dipoles and all temperatures being below T_c.

For dielectric loss (tan δ) however, the opposite is true, with temperature having a more pronounced influence in addition to response to time varying field. This is due to dielectric losses being largely influenced by domain wall vibrations [121], which can be easily altered or displaced even by a weak electric field or change in temperature. Therefore, tan δ can be said to represent the change in domain wall contribution to the overall polarisation of material. Dielectric loss (tan δ) is given as a ratio:

$$\tan\delta = \frac{\varepsilon''}{\varepsilon'} \qquad \textbf{Eq. 5-2 [71]}$$

Figure 5-9 shows the BIT dielectric loss data measured at various temperatures and in the frequency range from 1 Hz to 1 MHz. Temperature contribution at low frequency is more pronounced and losses are largely influenced by DC conductivity as well as polarisation and relaxation components. At higher frequencies, polarisation

contribution diminishes with increasing phase lag between the alternating field and the domain polarity, leaving the relaxation component as a more dominant factor.

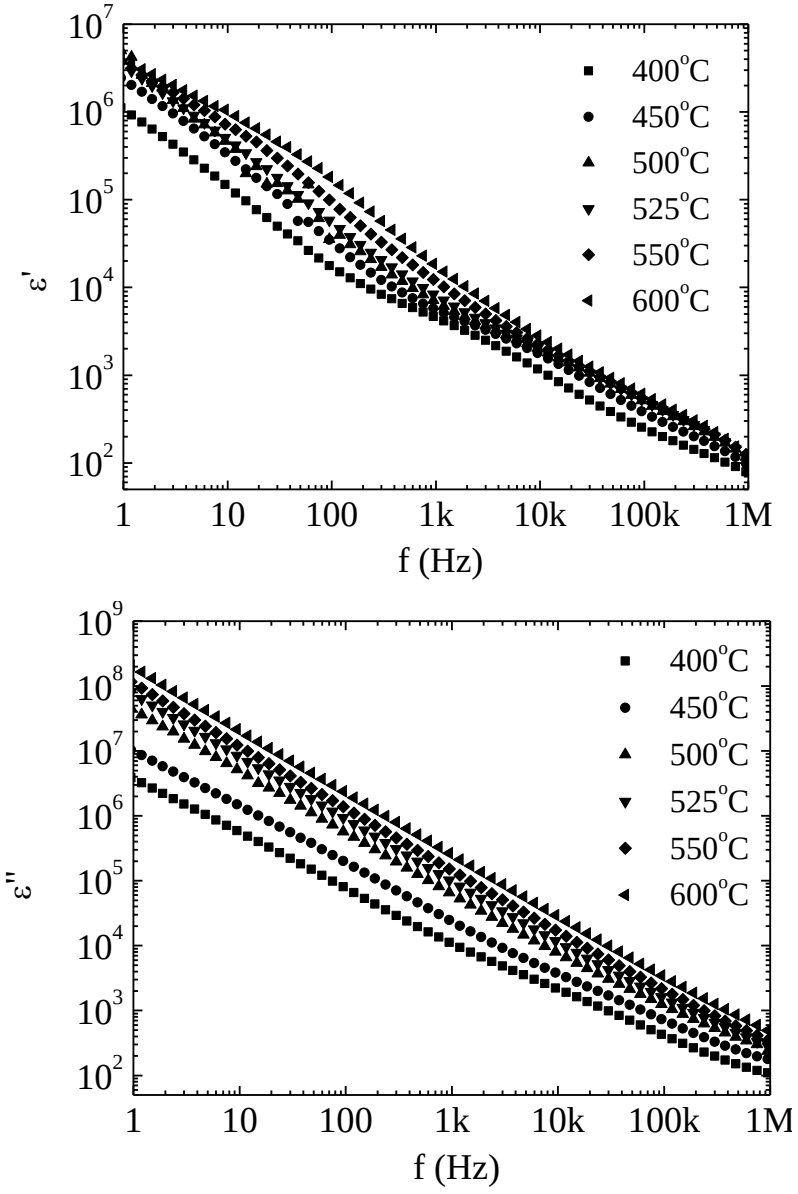

Figure 5-8 Permittivity of BIT in frequency range between 1 Hz to 1 MHz, showing the real (ε') and the imaginary (ε'') part.

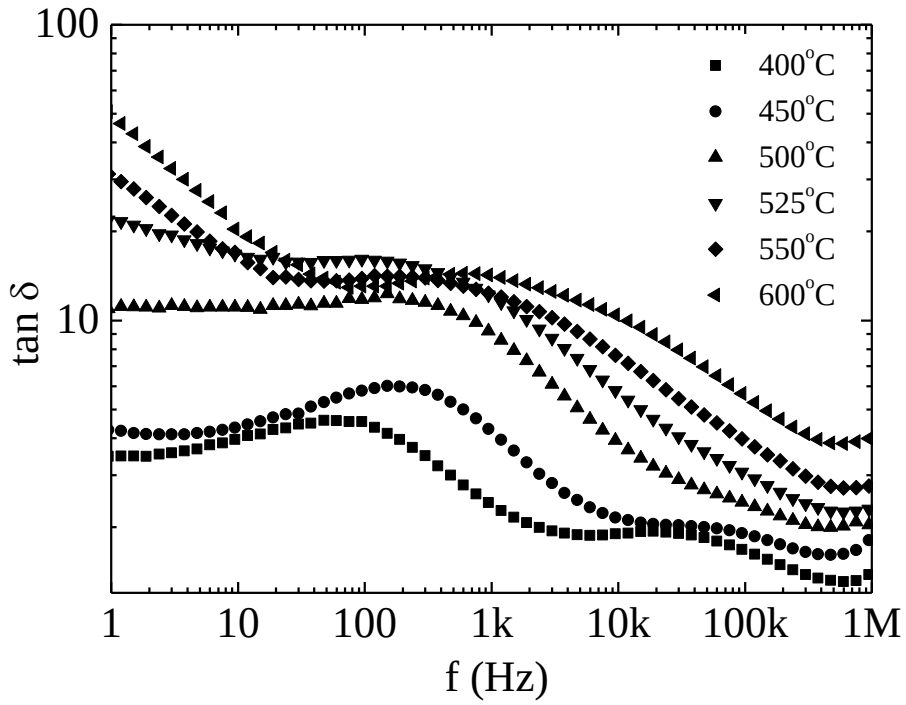

Figure 5-9 Dielectric loss data for BIT at various temperatures and frequency range from 1 Hz to 1 MHz. Dielectric loss represents the tangent of the phase angle between voltage and current.

Low frequency losses are influenced by DC conductivity (σ_{DC}), which is given by;

$$\sigma_{DC} = \omega\varepsilon_0 \times \varepsilon''_{DC} \qquad \textbf{Eq. 5-3 [71]}$$

where ε_0 is the permittivity of vacuum. AC conductivity is given by;

$$\sigma_{AC} = \sigma_{DC} + A\omega^n \qquad \textbf{Eq. 5-4 [122]}$$

where exponent *n* represents many body interactions of the charges, impurities and electrons. It is influenced by temperature and ranges from 0 to 1; 0 for pure conductance and 1 for pure capacitance. *A* is the polarisability factor, which is temperature dependant but a frequency independent quantity

The migration of relaxation peaks can be further studied by looking at the relationship between electrical relaxation frequency and the temperature, by means of the Arrhenius relation which is given by;

$$f_m = f_o \exp\left(-\frac{E}{kT}\right) \qquad \textbf{Eq. 5-5}$$

Here, f_o is the pre exponential or frequency factor, k is the Boltzmann constant, T is the absolute temperature and E is the activation energy.

The activation energy was calculated using Eq. 5-5 and the linear fit of the estimated peak data at different temperatures shown in Figure 5-10. A degree of data spread is observed which can be put down to rather broad peak data and estimated values as sources of error. However, it is found that activation energies for the two peaks are 1.64 and 1.29 eV respectively.

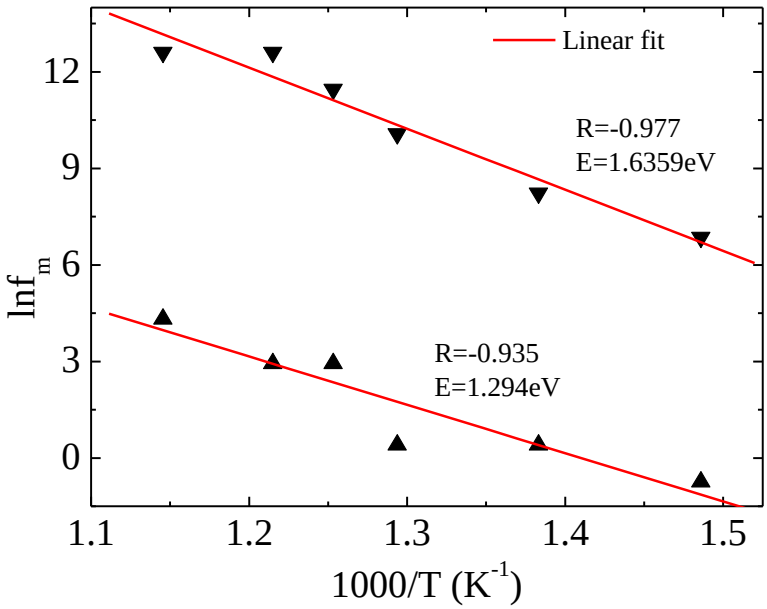

Figure 5-10 Arrhenius plot for relaxation frequency vs. temperature.

In order to explain the transport mechanism in BIT, influence of temperature on electronic conductivity is studied. Electronic AC conductivity can be expressed in terms of permittivity and dissipation factor as given in Eq. 5-6.

$$\sigma(\omega) = \omega.\varepsilon_o.\varepsilon^{'}.\tan\delta \qquad \textbf{Eq. 5-6}$$

Here, ω is the angular frequency and ε_0 is the permittivity of free space. Dielectric loss studies have suggested that temperature has a strong influence and that at low frequencies DC conductivity is dominant. The increasing influence of AC conductivity therefore comes with increase in frequency and this can be observed in Figure 5-11.

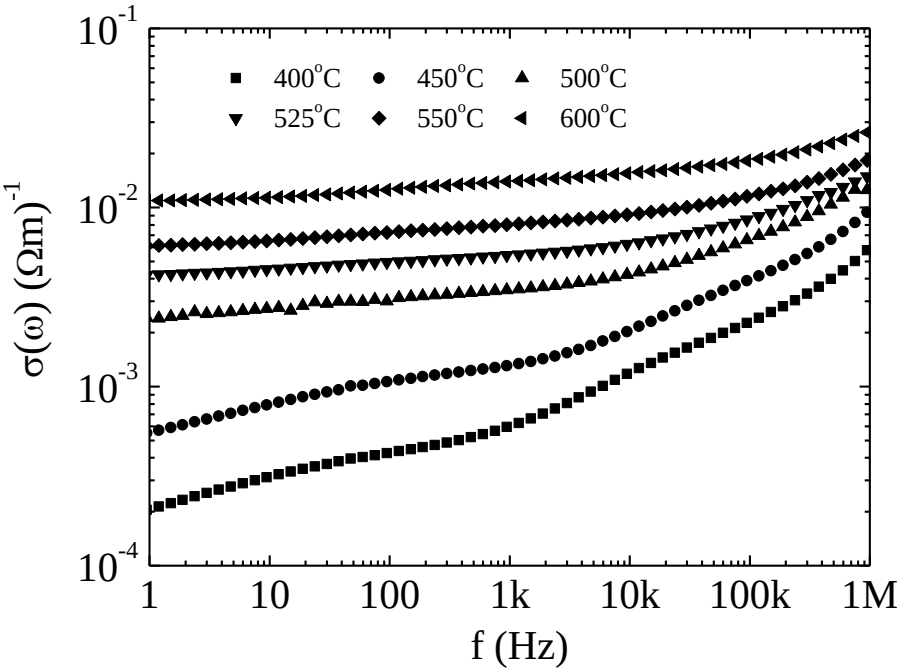

Figure 5-11 BIT AC Conductivity measured at various temperatures and at a frequency range between 1 Hz to 1 MHz.

However, data in Figure 5-11 implies that this assessment applies strongly at low temperatures whilst at high temperatures DC conductivity is a dominant contributor. This is indicated by a gradual flattening of the trace with the increasing temperature. Taking into consideration the frequency from 1 Hz to 1 MHz as shown in Figure 5-11, it can be said that conductivity is due to space charge and hopping polarisation, both of which have certain time constants associated with them. The influence of temperature on DC conductivity can be examined by applying the Arrhenius equation.

$$\sigma_{DC} = \sigma_o \exp\left(-\frac{E_{DC}}{kT}\right) \qquad \textbf{Eq. 5-7}$$

Here, σ_o is pre-exponential factor and E_{DC} is activation energy associated with dc conductivity. DC conductivity is shown as a function of inverse of absolute temperature in Figure 5-12. The variability in activation energy associated with DC conduction is estimated from the slope of the linear fit and the processes responsible for activation energy can be ascribed to ionic hoping and dipole relaxation [74].
It is important to note that some defects in the crystal lattice are due to volatilisation of bismuth oxide during sintering, causing oxygen and bismuth vacancies. However, greater loss of Bi than oxygen is expected which is electrically compensated by holes, in turn increasing conductivity at higher temperatures.

The analysis of pure BIT data suggests relatively high conductivity making the material difficult to polarise and lowering its piezoelectric properties only being able to achieve 8 pC N^{-1}. This, in general terms, agrees with published literature [72, 122, 123], and therefore a case is built for research effort into reduction of conductivity in bismuth titanate.

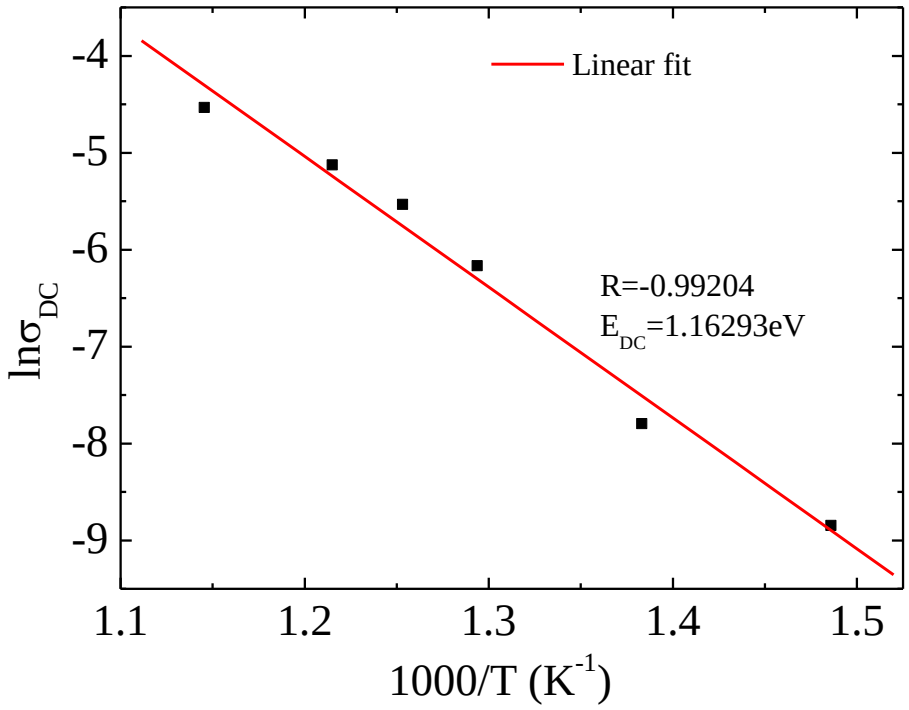

Figure 5-12 DC conductivity as a function of inverse of absolute temperature

5.4. Multi-doping of Bismuth Titanate for Enhancing Piezoelectric Properties

5.4.1. Tungsten and Chromium Doped Bismuth Titanate

The study into the influence of tungsten doping on sintering and electrical properties of bismuth titanate was reported by Villegas et al. [92]. It is reported that relatively weak doping with tungsten has a significant effect on grain growth, density and electrical conductivity. At low levels of dopant, densification is controlled by increase in diffusion coefficient of ions in the lattice and/or along the grain boundaries, whilst with increased amount of doping excess tungsten which could not be incorporated into the BIT lattice is acting as a grain growth inhibitor. Tungsten comes with an excess of electrons which can compensate for excess holes in pure BIT, thus decreasing the electrical conductivity. Notable improvement in electrical properties is attributed to the incorporation of tungsten into the BIT lattice structure with substantial decrease in conductivity and dielectric losses, and an increase in the d_{33} value to 22 pC N^{-1}.

It is reported that chromium addition is effective at reducing dielectric loss and ageing rate [61, 124-126], so it acts as a stabilizer of piezoelectric and dielectric properties. Within the BIT crystal structure, incorporation of Cr at the B-sites, results in increase in oxygen vacancy concentration which tend to form stable $Cr_{Ti} - V_O$ pairs, responsible for pinning domain walls and decreasing ageing. Excess of oxygen vacancies can promote sintering by enhancing lattice diffusion rates, reduce grain size and change the texture by altering the growth kinetics. The sintering and densification mechanism is also influenced by addition of chromium to the grain boundaries since accumulation of chromium ions (Cr^{3+}) at the grain boundary inhibits the grain growth, particularly at concentrations between 0.2 and 0.3 wt%, and hence has a positive contribution to the final density of the polycrystal [124]. Although literature survey reveals much previous study concerning doping with tungsten or

chromium, reports on simultaneous tungsten/chromium doped bismuth titanate BITWC were found to be scarce.

In this project, a composition of bismuth titanate doped with tungsten and with added chromium was investigated. It was expected that the effects from the two dopants would complement each other, producing enhanced piezoelectric and dielectric properties.

$Bi_4Ti_{3-x}W_xO_{12+x}$ + 0.2 wt% Cr_2O_3 (BITWC, x = 0 – 0.15) ceramic was prepared and characterised using methods described previously. The concentration of added chromium was kept low, in line with findings reported by Hou et al. [124], and Figure 5-13 shows BITWC XRD patterns reflecting the range of tungsten concentrations. It shows that BITWC maintains BLSF structure even under extensive modification by W^{6+}/Cr^{3+}. It should be noted that the amount of Cr added corresponds to only 0.046 atomic fraction per molecule of $Bi_4Ti_{3-x}W_xO_{12+x}$, such that effect of Cr should not swamp the effect of W (at x > 0.023) in improving the dielectric property of the doped BIT. Detailed study of the evolution of peaks relative to concentration of tungsten, shown in Figure 5-14, reveals some moderate changes in crystal structure with increased concentration of W.

It can be observed that at low concentrations of tungsten there are two close peaks at 2θ of 33°, which is in agreement with the orthorhombic structure of BIT. With the increasing concentration of tungsten, peaks (020) and (200) begin to merge and eventually combine into a single peak at x = 0.05. Further narrowing of the peak and a subtle shift higher of the 2θ value is evident with increasing concentration. The merger of (020) and (200) peaks, and the shift of the 2θ values at higher concentration indicates a decrease in lattice parameters and reduction in orthorhombicity. Migration of the (1115) peak, with its complete absence above x = 0.10 relative to tungsten concentration, is also evident. This suggests that the presence of tungsten ions at the B-site distorts the crystal lattice at the pseudo-perovskite layers, due to the ionic radius of tungsten being 5 % less than that of titanium, leading to a looser fit and a reduction in interatomic spacing. XRD data indicates that the structural distortion caused by tungsten ions is mainly affecting the lattice in the *a* and *b* planes, whilst no notable changes are observed for the *c* parameter. Since the majority of changes occur below x = 0.10, this indicates that above this concentration, presence of a secondary phase such as $Bi_6Ti_3WO_{18}$ [127, 128] is probable, although it is below the detection limits of the XRD.

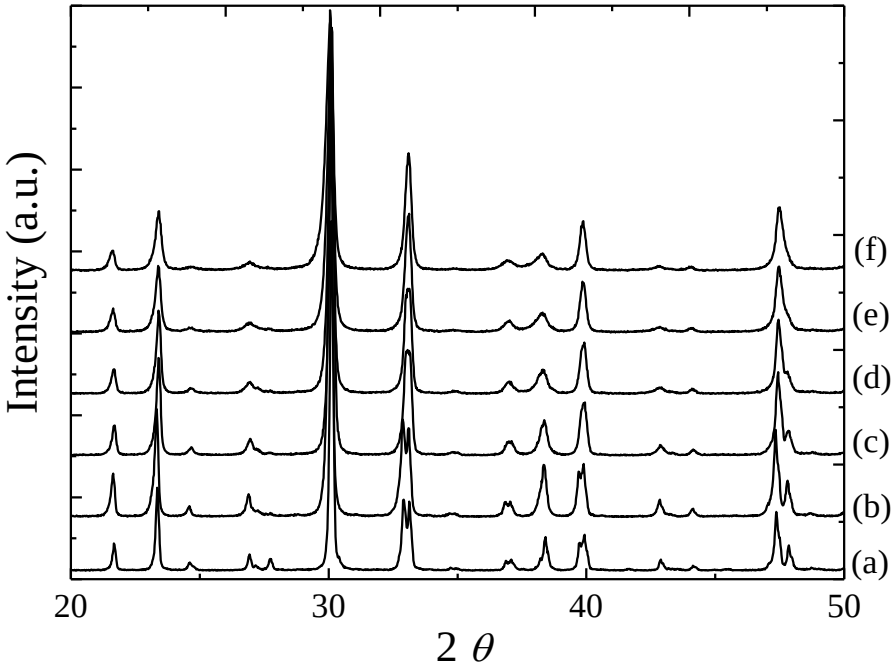

Figure 5-13 XRD patterns of BITWC with 0.2 wt% of chromium and tungsten concentration (x) of: (a) 0.0, (b) 0.025, (c) 0.05, (d) 0.075, (e) 0.10 and (f) 0.15.

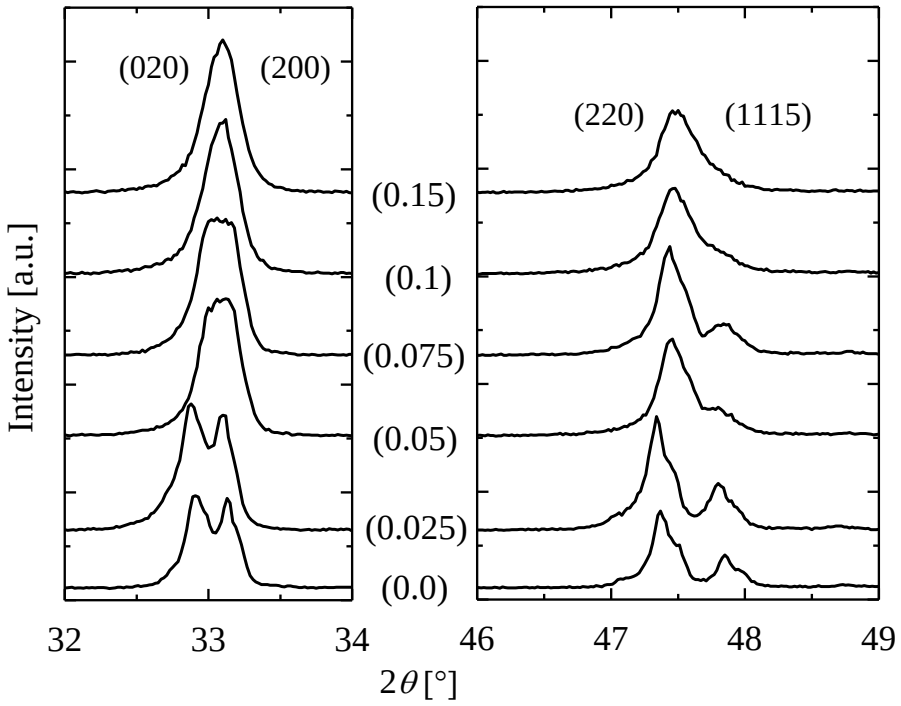

Figure 5-14 Evolution of XRD patterns with increased concentration of tungsten (x). Merger of peaks can be attributed to decrease in lattice parameters.

Presence of the secondary phase is also suggested by the EDS analysis data shown in Table 5-1. A notable change in the data pattern can be observed with $x \geq 0.075$.

With $x < 0.075$, pure BIT element composition is maintained and there is only marginal variation possibly due to different evaporation rates of bismuth during sintering. This suggests incorporation of tungsten and chromium ions into the BLSF structure.

At $x \geq 0.075$ compositions are in less agreement with that of pure BIT, indicating possible presence of the secondary phase.

Element	BIT	x = 0.025	x = 0.05	x = 0.075	x = 0.1	x = 0.15
Bi	4.00	3.98	3.97	3.96	3.93	3.87
Ti	2.99	2.98	2.94	2.91	2.86	2.81
W	0	0.025	0.05	0.076	0.11	0.16
Cr	0	0.4	0.4	0.39	0.4	0.37
O	12.00	12.00	12.00	12.08	12.09	12.16

Table 5-1 Energy Dispersive Spectroscopy (EDS) data showing atomic ratios for various doping compositions.

Figure 5-15 shows polished and thermally etched surfaces of BITWC ceramics at different tungsten/chromium concentrations. It is apparent that the average grain size decreased with the increase in concentration from approximately 10 μm to 1 μm. This suggests strong influence of tungsten/chromium on the plate like grain growth and the enhanced densification of ceramics at higher concentrations, which can be attributed to a slower grain boundary diffusion process [129]. Decreased grain size leads to better granular arrangement during sintering and thus aids densification.

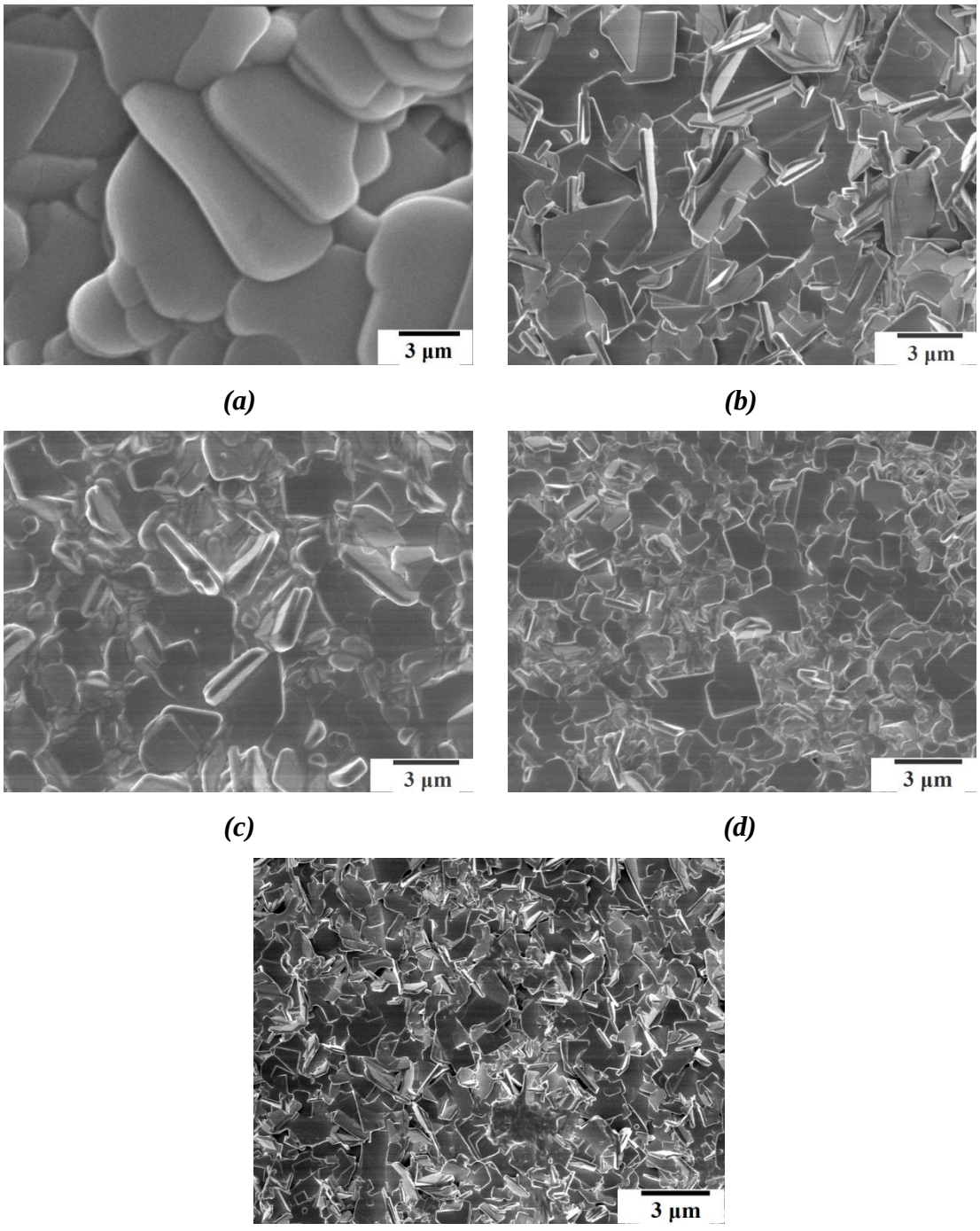

(a) ***(b)*** ***(c)*** ***(d)*** ***(e)***

Figure 5-15 SEM images of tungsten chromium modified BIT sintered and thermally etched samples for tungsten (x): (a) 0.025, (b) 0.05, (c) 0.075, (d) 0.10 and (e) 0.15. Decreasing grain size with increased tungsten concentration is evident.

A further characterisation study was carried out based on impedance data of x = 0.025 composition and Figure 5-16 shows the variation in real (Z') and imaginary (Z'') impedance at various temperatures and a range of frequencies.

It is evident based on real impedance data that the value of Z' decreases significantly with increased frequency as well as temperature, suggesting an increase in AC conductivity. The normalised imaginary impedance plot (Z''/Z'_{max}) as a function of frequency is also shown and it can be seen that at higher temperatures, the peak is shifting to higher frequencies. All peaks show the same characteristic shape, demonstrating that the relaxation behaviour is caused by the same mechanism. This is a typical, temperature dependant relaxation behaviour seen in dielectric materials, which can be attributed to defects or vacancies.

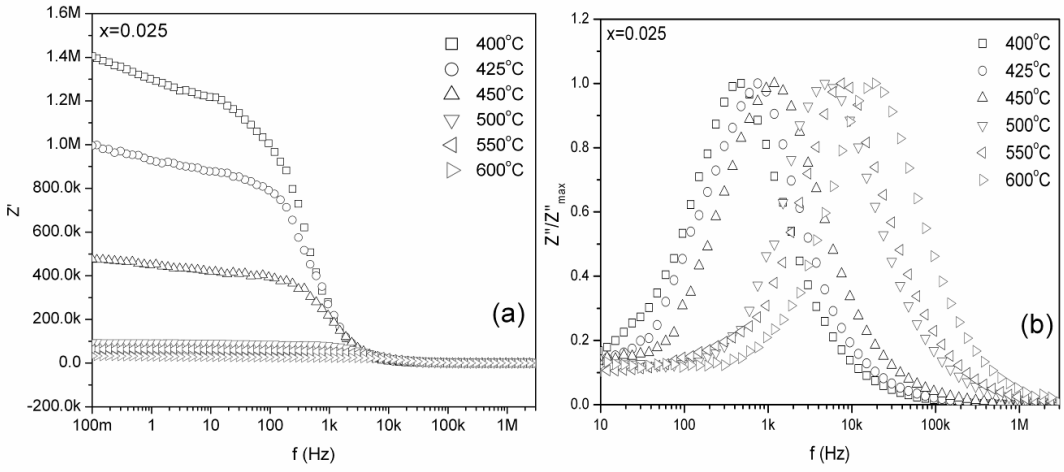

Figure 5-16 **BITWC** (a) Real and (b) imaginary parts of complex impedance versus frequency plots at various temperatures for x = 0.025 composition. Temperature dependant relaxation behaviour is evident.

The activation energy of the relaxation mechanism was studies using the Arrhenius equation, where relaxation frequency is plotted against the inverse of absolute temperature and the slope of the linear fit can be used to calculate activation energy. Calculated activation energy for different BITWC compositions is shown in Figure 5-17 and it can be seen that the activation energy is increasing with the increase in doping concentration. This implies a decrease in oxygen vacancy and defect concentration, which is in strong agreement with findings published by Coondoo et al. [130].

Using complex impedance data, a dielectric P was calculated based on the following relationship;

$$\varepsilon' = \frac{-Z''}{\omega C_o \left(Z'^2 + Z''^2\right)} \qquad \textbf{Eq. 5-8}$$

where C_0 is the equivalent vacuum capacitance of the sample and ω is the angular frequency.

The temperature dependence of the dielectric permittivity is shown in Figure 5-18. It is evident that all dielectric peaks reside above 640 °C, which corresponds to T_c of the composition. This is slightly lower than T_c values for pure BIT and a gradual decrease from 675 °C to 640 °C, linked to dopant concentration, is shown in the lower graph. Decrease in T_c could be attributed partly to differences in ionic radii and also to decrease in lattice distortion [131, 132]. Again, the presence of a second phase is suggested by the damped secondary peak with $x \geq 0.1$ [128, 133].

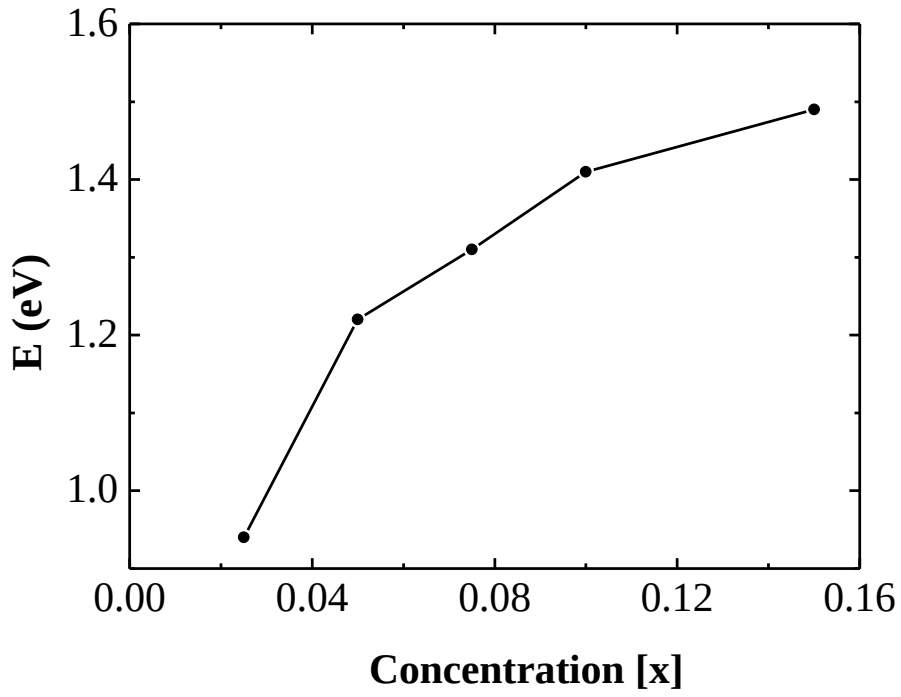

Figure 5-17 Activation energy versus dopant concentration, calculated using Arrhenius relation.

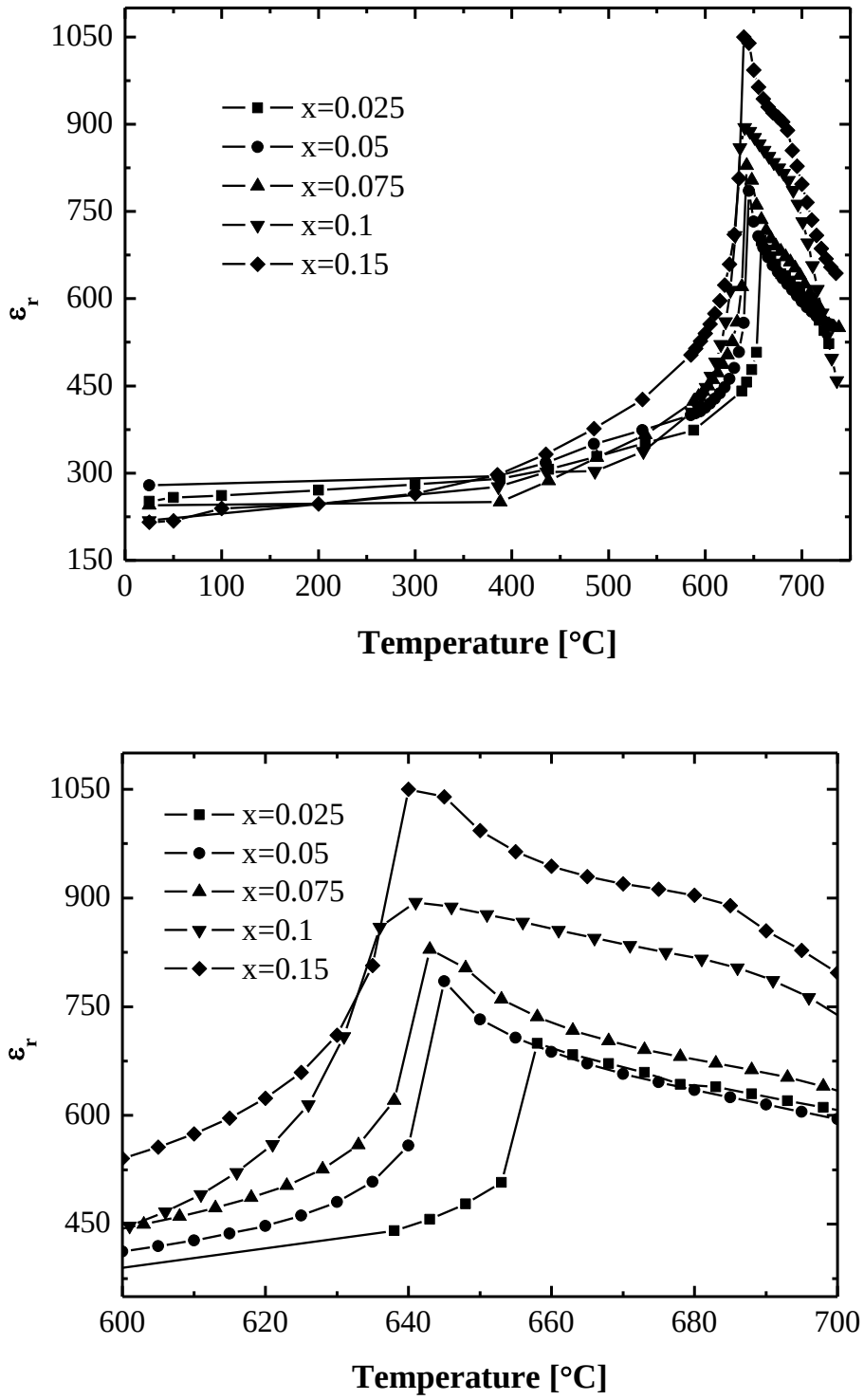

Figure 5-18 Dielectric permittivity as a function of temperature and dopant concentration for BITWC shown for the 0 to 750 °C temperature range (upper graph), and the detail around 650 °C (lower graph). Sharp peaks above 600 °C identify the phase transition or Curie temperature.

Dielectric loss was calculated as a real and imaginary impedance ratio using Eq. 5-9, and data is shown graphically in Figure 5-19.

$$\tan\delta = \frac{Z'}{-Z''} \qquad \textbf{Eq. 5-9}$$

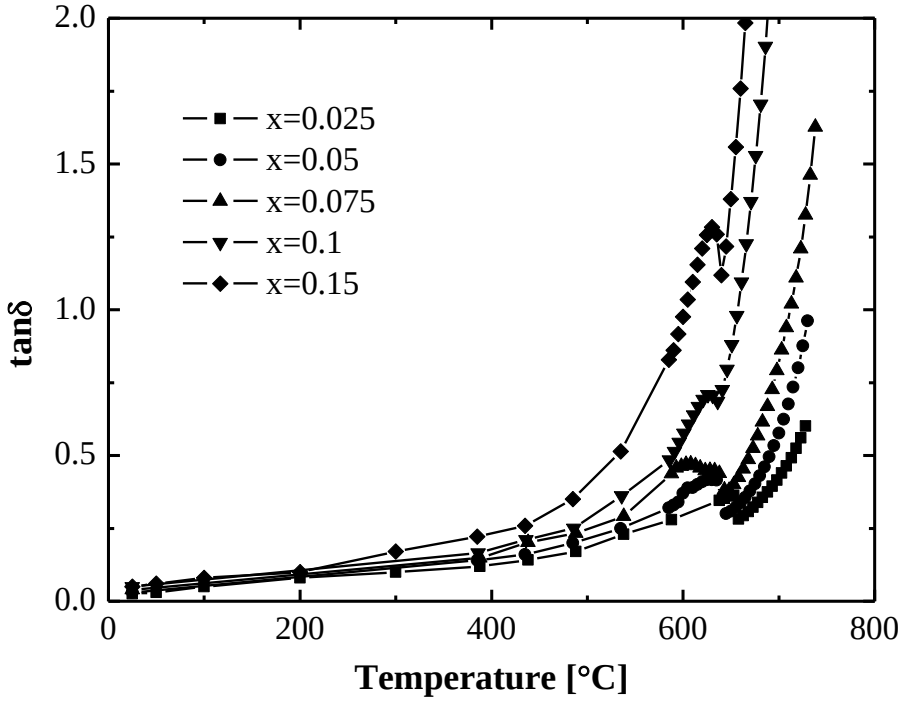

Figure 5-19 Dielectric loss as a function of temperature for various compositions.

On approaching the Curie temperature, lossy behaviour for all compositions of the material is brought to a peak just below T_c, triggered by domain wall movement, and then suddenly reduces at the T_c point. It bottoms out with the phase transition and after this the value of dielectric loss increases for all compositions.

Peaks identified in both dielectric permittivity and dielectric loss are in agreement for phase transition temperature, and characteristic room temperature properties for various compositions are listed in the Table 5-2. It can be seen that with increased dopant concentration the Curie temperature decreased whilst the dielectric permittivity and loss exhibit marginal increase.

The piezoelectric coefficient is shown to benefit substantially from mild doping with W and Cr, compared to pure BIT. However, the d_{33} value decreases with the increasing dopant concentration, which can be attributed to reduced defect density.

$Bi_4Ti_{3-x}W_xO_{12+x}$ +0.2 wt% Cr_2O_3	T_c [°C]	ε' (at 100 kHz)	$\tan\delta$ (at 100 kHz)	d_{33} [pC N^{-1}]
x = 0.025	658	178	0.02	22
x = 0.05	650	186	0.021	17
x = 0.075	648	197	0.023	16
x = 0.1	645	205	0.028	14
x = 0.15	640	211	0.028	12

Table 5-2 Summary of physical characteristics of BITWC at room temperature for various compositions. It shows a marginal reduction in T_c and a substantial improvement in d_{33}.

A further transport mechanism study can be carried out by observations in electrical conductivity behaviour within ceramics at different temperatures and dopant concentrations. Frequency dependant electrical conductivity (σ_ω) and dielectric behaviour are linked by the relationship;

$$\sigma_\omega = \omega\varepsilon_0\varepsilon'\tan\delta \qquad \textbf{Eq. 5-10 [130]}$$

where ω is the angular frequency and ε_0 is the permittivity of the vacuum.

Frequency dependant conductivity is a function of dynamic response and as such it is a sum of ac and dc conductivity;

$$\sigma_{\omega} = \sigma_{DC} + A \times \omega^{n} \qquad \textbf{Eq. 5-11 [130]}$$

A is a temperature dependent parameter and the exponent *n* is a characteristic parameter representing the many body interactions of the electrons, charges, and impurities. It varies from 0 to 1 and for an ideal Debye-type behaviour it is equal to 1 [134]. Given that σ_{ω} is the sum of ac and dc components of conductivity, it is more appropriate than a study of dc alone for the present application.

Ac conductivity is shown in Figure 5-20 for different BITWC composition as well as pure BIT.

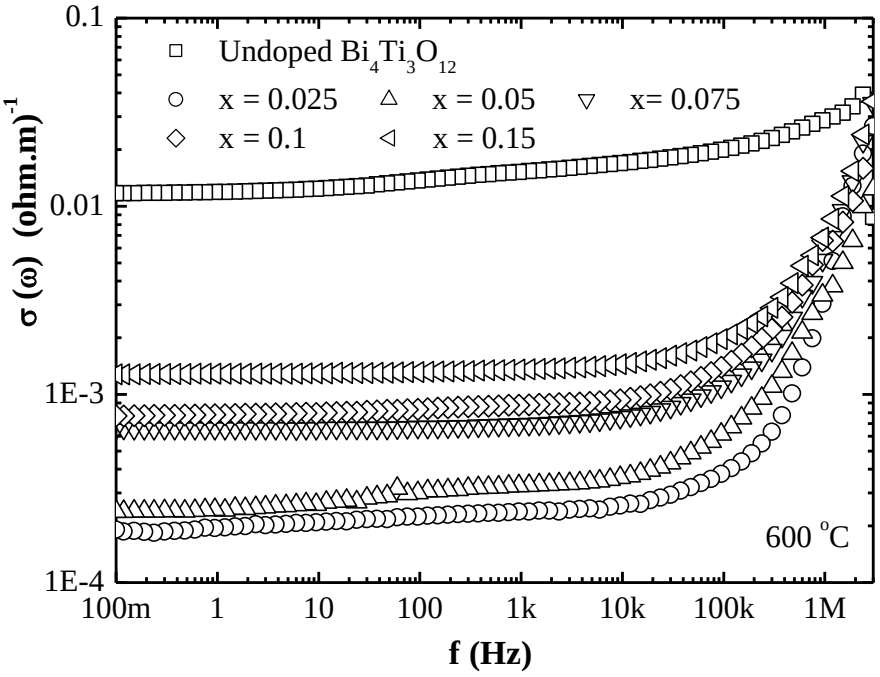

Figure 5-20 Frequency dependent electrical conductivity for BITWC variant compositions at 600°C. The influence of low dopant concentration is marked by a significant reduction in conductivity.

It is interesting to note that the conductivity in pure BIT at 600 °C is evidently much higher than of any other composition of BITWC. The biggest reduction in conductivity is achieved with lowest dopant concentration of x = 0.025, after which the conductivity begins to increase.

In bismuth titanate ceramics, hole compensation of bismuth vacancies promotes *p*-type electronic conductivity [91]. When W^{6+} substitutes Ti^{4+}, two positive charge centres at W sites and two electrons will be created under the charge neutrality restriction. These electrons neutralize the influence of the holes, and therefore the conductivity decreases with donor doping to a minimum value where the concentration of electron holes matches the electron concentration. With a further increase in the donor concentration, the conductivity becomes *n*-type and starts to increase again.

5.4.2. Niobium and Tantalum Doped Bismuth Titanate - BITNT

Tungsten and chromium multidoping has been shown to enhance the properties of base BIT composition, both in terms of lower conductivity as well as higher piezoelectric coefficient, with moderate compromise on Curie temperature. Continuing with the theme of using the multidoping strategy established in the previous section, consideration was given to niobium and tantalum. In previous work published on the subject of reduction of conductivity in BIT, niobium has been shown to be a good candidate as an aliovalent, B-site donor dopant [74, 75, 93]. However, no scientific literature was found in connection with simultaneous doping with niobium and tantalum. Alternative composition was investigated in the present work and multidoped base BIT with niobium and tantalum was produced using the solid state sintering method described previously. Initial experimental data suggested that low concentrations produced highest increase in piezoelectric coefficient.

$Bi_4Ti_{3-2x}Nb_xTa_xO_{12+2x}$ green powder with concentrations x = 0.01 (BITNT1), x = 0.02 (BITNT2), x = 0.04 (BITNT4) and x = 0.06 (BITNT6), was manufactured by calcination at 800 °C for 4 hours. Crystal structures were analysed using XRD and the results are shown in Figure 5-21.

As expected due to very low dopant concentration, diffraction data does not indicate any presence of niobium or tantalum oxides and all peaks can be accounted for by primary phase BIT. This suggests that Nb and Ta ions in the BITNT ceramics do not form a secondary phase or segregate at the grain boundaries but diffuse into the pseudo perovskite lattice. Strong peak consistency at different concentrations is also an indication that the cell parameters remain consistent with that of base BIT, particularly when we take into consideration that the ionic radius of Ti, Nb and Ta is distinctly comparable, with Nb (V) ions being 2.9 % and Ta (V) ions being 7.4 % larger than Ti (IV) ions. Therefore, the BTNT ceramic maintains a layer structure similar to that of perovskite BIT.

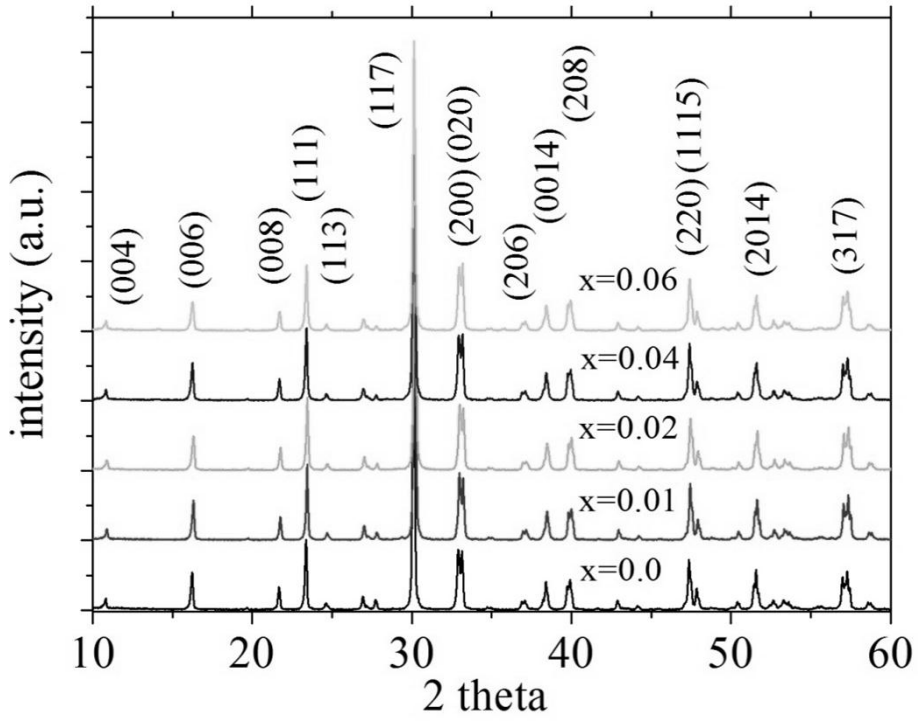

Figure 5-21 XRD patterns of $Bi_4Ti_{3-2x}Nb_xTa_xO_{12+x}$ powders calcined at 800 °C for 4 h on different Nb/Ta amounts.

Microstructure investigation reveals significant influence by low dopant concentration on sintering kinetics of BITNT, and a general trend for reduction in grain size with increasing doping can be noted.

The surface microstructures of BITNT ceramic are shown in Figure 5-22. It can be seen that the grain size ranges from around 40 μm to less than 1 μm in length, which suggests that dopant combination is a grain growth inhibitor, much like tungsten and chromium as shown previously, and the main sources of porosity are observed at the grain boundaries.

Both sintering and grain growth are closely associated with ion migration and it can therefore be expected that if the incorporation of aliovalent niobium and tantalum into BIT structure led to an increase in the activating energy, a reduction in the grain size would be expected with the increasing dopant concentration. This is in agreement with the BITWC study and according to the sintering theory, the particle surface energy and grain boundary energy are the major driving forces for sintering and grain growth.

Another important observation that can be made is that at minimum dopant concentration, the grain structure tends to have a higher degree of uniformity than those of increased doping with a well-defined structural orientation. A definite preferred direction of long flat grains is particularly evident in Figure 5-22(a).
Taking into consideration the very isotropic nature of the green powder, this can be attributed to the application of uniaxial force during the shaping process prior to sintering. In absence of the inhibitor, high grain growth rate during the dwell cycle results in large plate like grains, which are oriented and lie perpendicular to the pressing axis. With the increased dopant concentration, grain growth rate is increasingly inhibited, preventing the agglomeration of smaller grains into larger ones. The evidence of this can also be seen in Figure 5-22 (b), where grains are not necessarily oriented to the same degree as in the previous image, but the plate like shape is still evident.

It would therefore be expected that BITNT1, with a higher degree of orientation, would have superior piezoelectric properties.

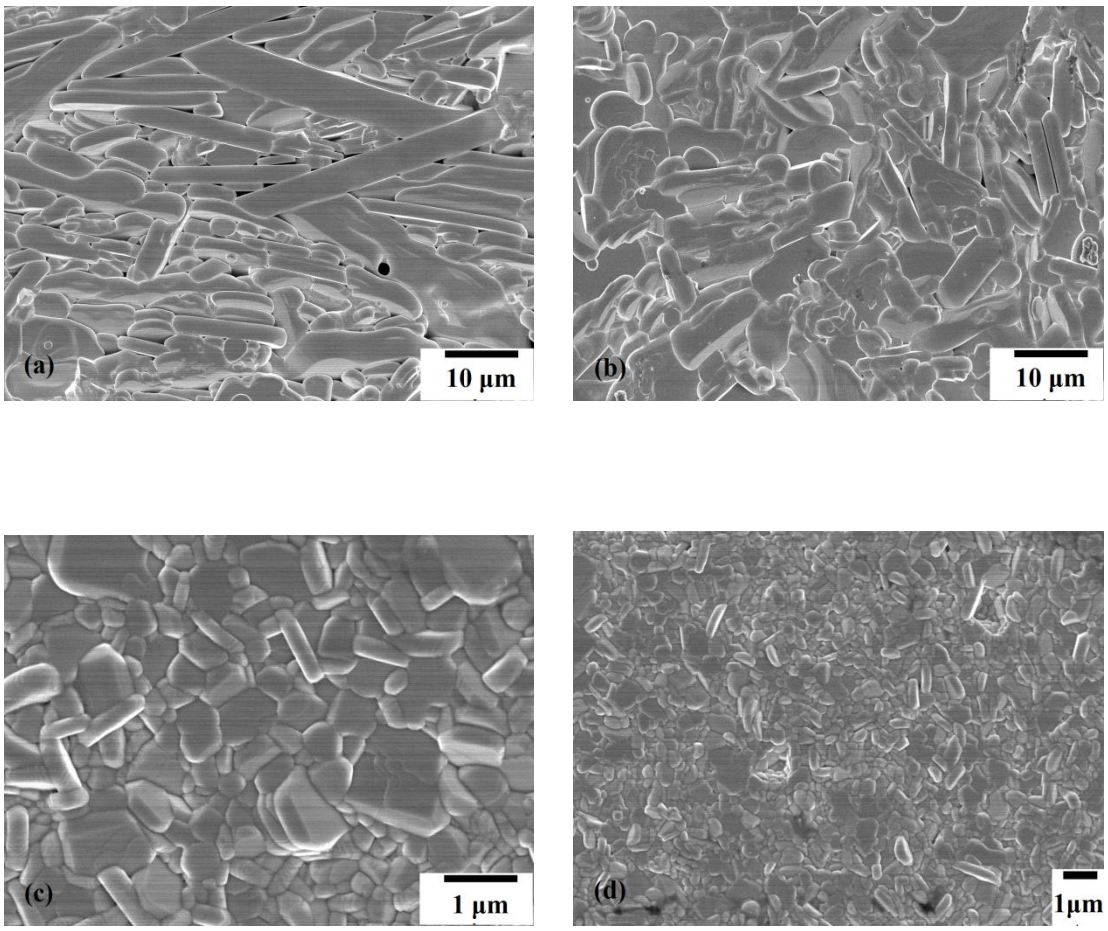

Figure 5-22 SEM images of $Bi_4Ti_{3-2x}Nb_xTa_xO_{12+x}$ ceramics demonstrating the influence of dopant concentration on microstructural evolution. (a) x = 0.01, (b) x = 0.02, (c) x = 0.04, (d) x = 0.06.

In order to evaluate dielectric properties of BITNT ceramics, samples were sintered to produce highest density values. Figure 5-23 shows the permittivity, ε_r, and dielectric loss, tan δ, of BITNT ceramics as a function of temperature measured at a frequency of 100 KHz. It can be noted that the phase transition temperature of BITNT ceramics gradually decreases from 675 to 630 °C with the increasing dopant concentration. This can be attributed to space charge and ionic motion [135]. Furthermore, the phase transition peaks become broader, which may be a product of increased cation exchange at the B-site between Ti^{4+} and dopants Nb^{5+} and Ta^{5+}, and release of misfit strain related to ionic radii. With regards to dielectric loss, there is an evident positive trend with increasing temperature and a peak position slightly below the phase transition temperature. After phase transformation, the dielectric loss reaches a minimum and then begins a steep increase. Increased dopant concentration is accompanied with the dielectric loss peak shifting to lower temperature and being less pronounced. This suggests the increase in activation energy of oxygen vacancies. It is clear that the introduction of donor dopants at the B-site can effectively reduce the oxygen vacancy concentration.

A decrease in oxygen vacancy concentration after doping, results in decrease of the dielectric loss peak, which is consistent with the previous reports [74, 77, 90, 91, 131].

Selected room temperature properties of BITNT ceramics as a function of Nb/Ta amounts and temperature are characterized and shown in Figure 5-24. It is evident that permittivity of the BITNT ceramics increased in line with dopant concentration, whist dielectric loss decreased due to depression in oxygen vacancies. It is interesting to note that piezoelectric coefficient peaks at a very low Nb/Ta concentration (BITNT1) and reaches the value of 26 pC N^{-1}, with a moderate decrease in T_c. Thereafter, the value steadily decreases. Previous research has shown that doping a small amount of Nb_2O_5 or Ta_2O_5 resulted in an increase of piezoelectric coefficient from 8 to 20 pC N^{-1} [75, 91]. This 30 % increase in piezoelectric coefficient by Nb/Ta co-doping is much desirable, indicating a significant improvement in piezoelectric properties. Enhancements can be attributed to grain orientation and size leading to coherent development of ferroelectric domains. As a result, there may be more crystallographic directions suitable for polarization, facilitating piezoelectricity.

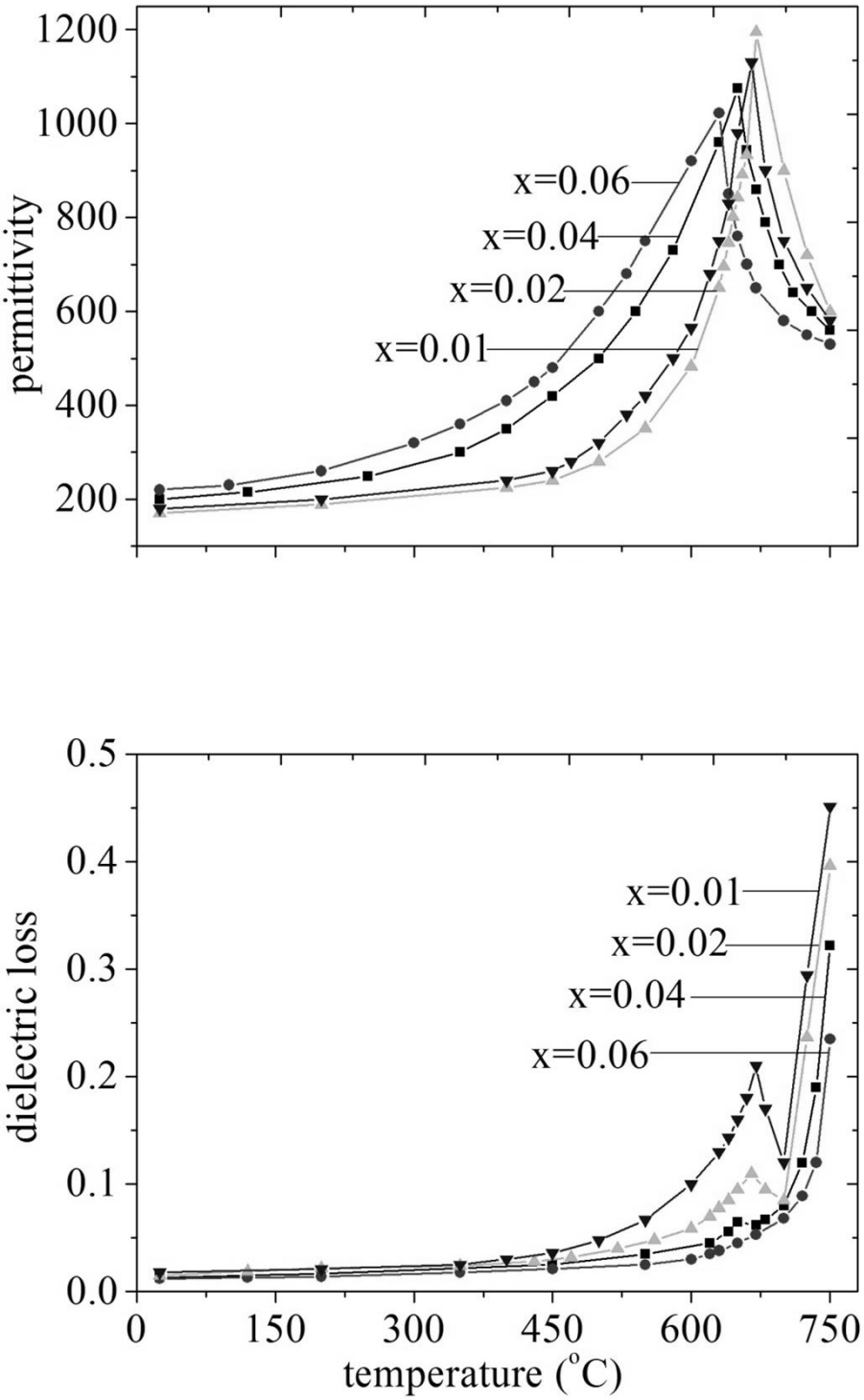

Figure 5-23 Temperature dependence of permittivity and dielectric loss for BITNT ceramics on Nb/Ta concentration.

Based on the decreasing trend in dielectric loss, it is proposed that the grain size effect is a fundamental factor influencing the piezoelectric response.

At the same time, with the decrease of oxygen vacancies diffusing into the domain wall, the occurrence of domain wall pinning decreased, whilst the number of available switching domain walls increased, further enhancing the d_{33} value.

It is suggested that an increase in dopant concentration above BITNT1 level could act as pinning centres for domain walls and decrease their d_{33} contribution, and this would be consistent with previous literature reports that incorporation of niobium and other cations into the perovskite layer leads to a dimensional mismatch between perovskite and bismuth oxide layers [136]. It is also suggested that beyond a certain concentration of doping with pentavalent cation dopants in tetravalent sites, a switch over to n-type conductivity can occur. There is an optimum level of doping at which p-type conductivity is exactly negated by electron donor dopants. Thermal depoling experiments were conducted by holding the poled samples for 2 hours at each temperature, cooling to room temperature, measuring d_{33}, and repeating the procedures at intervals of 50 °C up to 700 °C.

As Figure 5-24(*d)* demonstrates, the values of d_{33} for the BITNT ceramics show a relatively stable behaviour with annealing temperatures up to 500 °C. With further increase in temperature to about 75 % of T_c, the piezoelectric coefficient of all BITNT compositions declines sharply and tends to zero at around T_c.
AC conductivity of BITNT1 at different temperatures and a frequency range from 0.1 Hz to 1 MHz is shown in Figure 5-24(*e*).

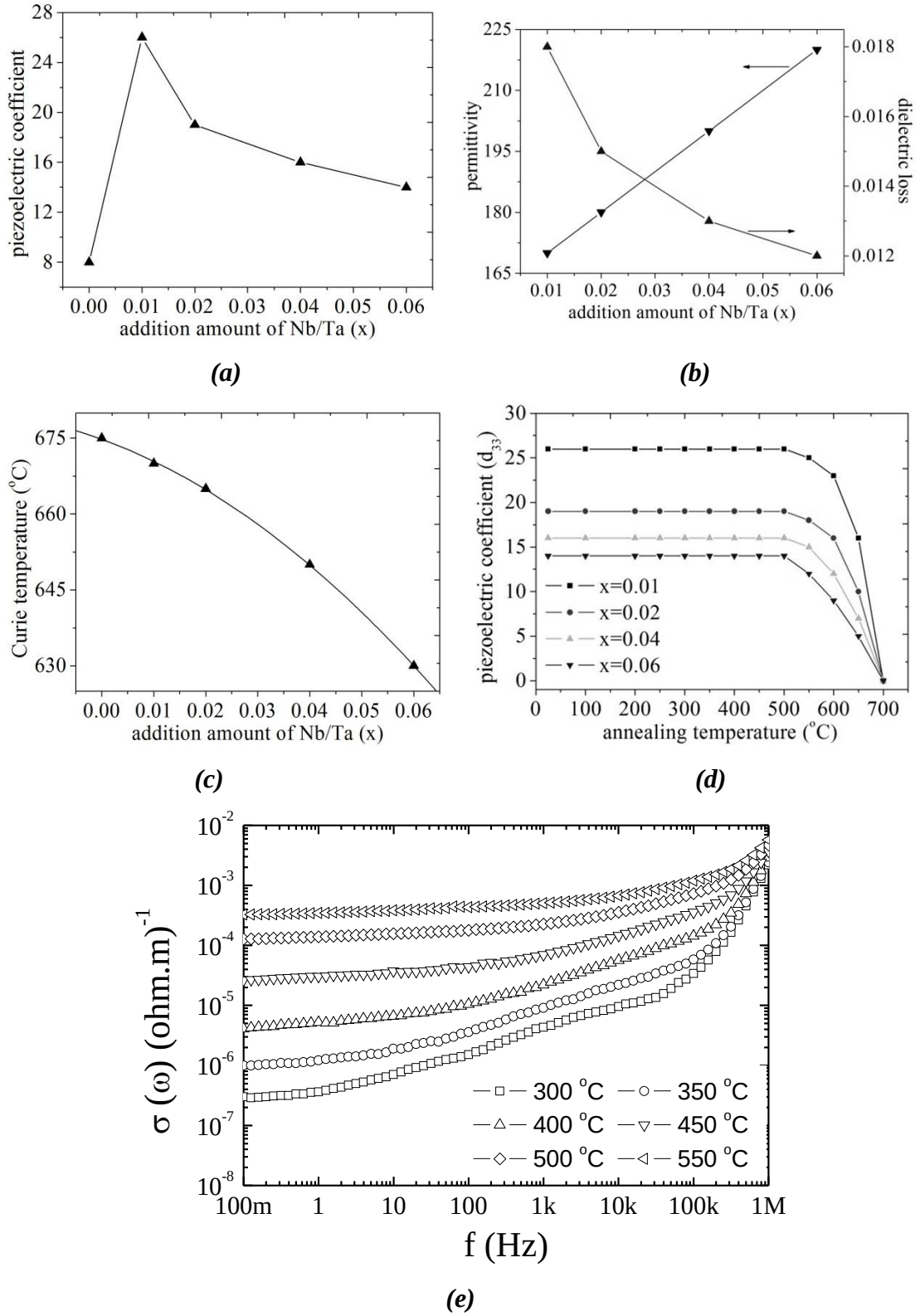

Figure 5-24 Properties of $Bi_4Ti_{3-2x}Nb_xTa_xO_{12+x}$ ceramics versus different Nb/Ta amounts at room temperature (*a,b,c*), the effect of annealing temperature on d_{33} of $Bi_4Ti_{3-2x}Nb_xTa_xO_{12+x}$ ceramics (*d*), and AC conductivity at various temperatures (*e*) for BITNT1.

5.4.3. Effects of Antimony Substitution on Structural and Electrical Properties in BITNT.

Previous studies on antimony doped lead-free piezoelectric materials indicate significant enhancements in piezoelectric and dielectric properties [137-139]. It is also noted that there were no reported studies on antimony doped bismuth titanate, so it was deemed worth while exploring further.

Continuing with the multidoping strategy, Sb_2O_3 was used to modify $Bi_4Ti_{3-2x}Nb_xTa_xO_{12+x}$ (BITNT) via the conventional solid state reaction route. The present study evaluated the additive influence of Sb_2O_3 on the structural, morphological, dielectric, electrical conductivity and piezoelectric properties of the ceramics.

The compositions of $Bi_4Ti_{3-2x}Nb_xTa_{x-y}Sb_yO_{12+2x}$ (BITNTS, x = 0.01, y = 0, 0.002, 0.004, 0.006, 0.008, 0.01, denoted as 0BITNTS, 2BITNTS, 4BITNTS, 6BITNTS, 8BITNTS and 10BITNTS, respectively) were prepared via the conventional solid-state reaction route described previously. Samples having diameter of 10 mm were sintered at an experimentally determined most favoured temperature of 1100 °C for 2 hours, whilst placed on a platinum foil to achieve optimum density. After sintering, samples were lapped to 0.5 mm thickness and silver ink electrodes were deposited using silk screening method. Samples were then fired at 750 °C for 30 minutes. Polarisation was carried out in a silicone oil bath at 180 °C and an electric field of around 60 kV cm^{-1} for 30 minutes, depending on dielectric strength of samples.

XRD patters of BITNTS powders calcined at 800 °C for 4 hours and sintered at 1100 °C for 2 hours are shown in Figure 5-25. The analysis of diffraction patterns reveals much consistency with that of BITNT1, therefore suggesting that BITNTS ceramic maintains layered perovskite structure assimilated to that of pure BIT.

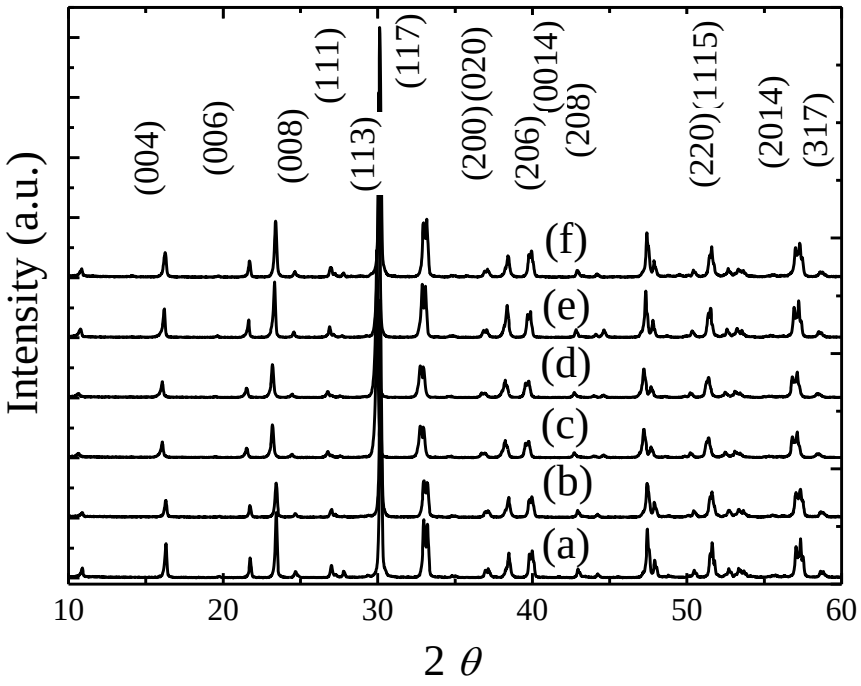

Figure 5-25 XRD patterns of BITNTS powders calcined at 800 °C for 4 hours and sintered at 1100 °C, with varying concentration of Sb_2O_3; (a) 0BITNTS, (b) 2BITNTS, (c) 4BITNTS, (d) 6BITNTS, (e) 8BITNTS, (f) 10BITNTS.

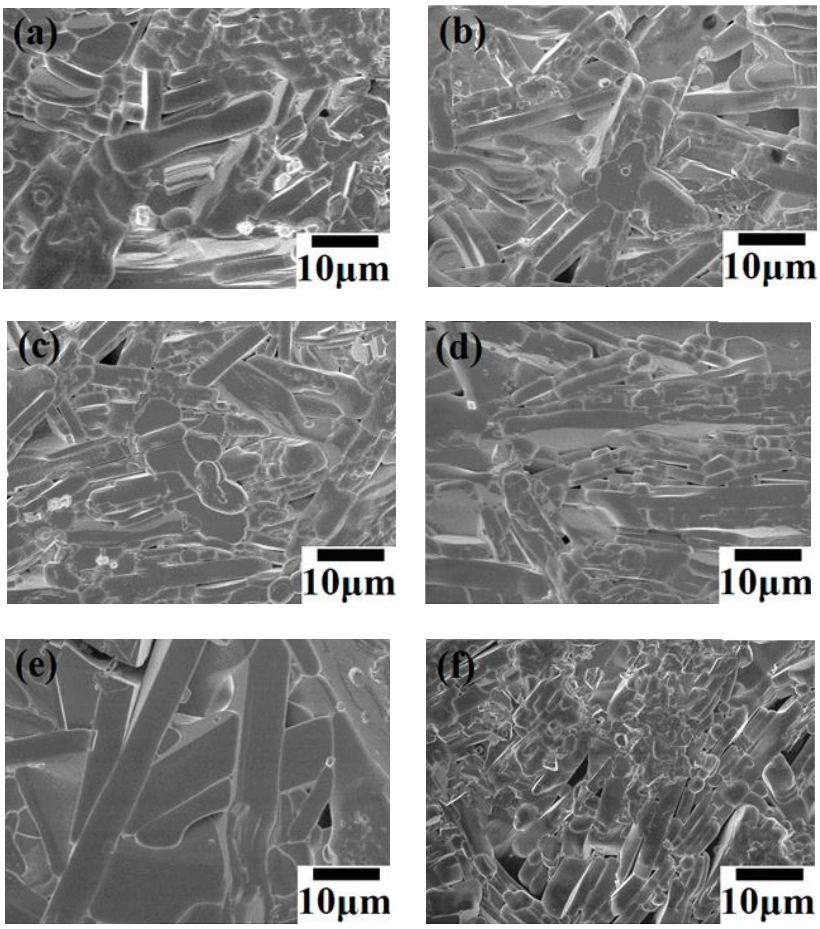

Figure 5-26 Surface morphology of thermally etched BITNTS ceramic for; (a) 0BITNTS, (b) 2BITNTS, (c) 4BITNTS, (d) 6BITNTS, (e) 8BITNTS, (f) 10BITNTS.

The surface morphology of BITNTS ceramics is shown in Figure 5-26.

In agreement with BITNT study, the average grain size is varying with dopant concentration. However, given that the overall ratio of dopant to BIT has remained constant in all compositions, the variation in grain size can be attributed to increasing concentration of antimony. It can be observed that 8BITNTS ceramic exhibits slightly larger grains whilst there is a small variation in grain size for the other samples.

Observable changes in microstructure with variation in dopant could be attributed to formation of liquid ($Bi_{12}TiO_{20}$) sillenite phase [140, 141], which is typically present during sintering of BIT. Figure 5-27 shows the Bi_2O_3 - TiO_2 binary system phase diagram.

The onset of solid BIT phase may be postponed by the increased concentration of Sb, allowing for the increased grain growth. 8BITNTS sample is shown to have the largest grain size due to the presence of larger quantity of sillenite phase. For 10BTNTS sample, with further increase in Sb concentration, the diminishing influence of tantalum for increased grain growth is brought to nothing, and a subsequent drop in grain size can be observed.

However, it is interesting to note that the sillenite phase was not detected by XRD analysis. One of the reasons for this is that sillenite phase is only stable up to 750 °C, and since calcination is carried out at 800 °C, all of the Bi_2O_3 has reacted with TiO_2, incorporating any doping ions and forming base BIT or BITNTS. Even though the phase transition occurs at a quite low temperature (< 750 °C), the grain growth is cumulative in nature, so the influence of this liquid phase contribution is significant.

Room temperature piezoelectric coefficient (d_{33}) characteristics of BITNTS are shown in Figure 5-28, and the variation in magnitude is evidently linked to Sb concentration. The value of d_{33} was found to be the highest for 8BITNTS composition achieving d_{33} = 35 pC N^{-1}, which is the highest reported value for BLSF material. Centering on the optimum values of x = 0.01 for both Nb (V) and Ta (V) ions in BIT, a partial substitution of Ta (V) by y = 0.008 Sb (III) has produced a large difference in d_{33} value suggesting that use of the Sb (III) has allowed the fine tuning of hole – electron doping transition.

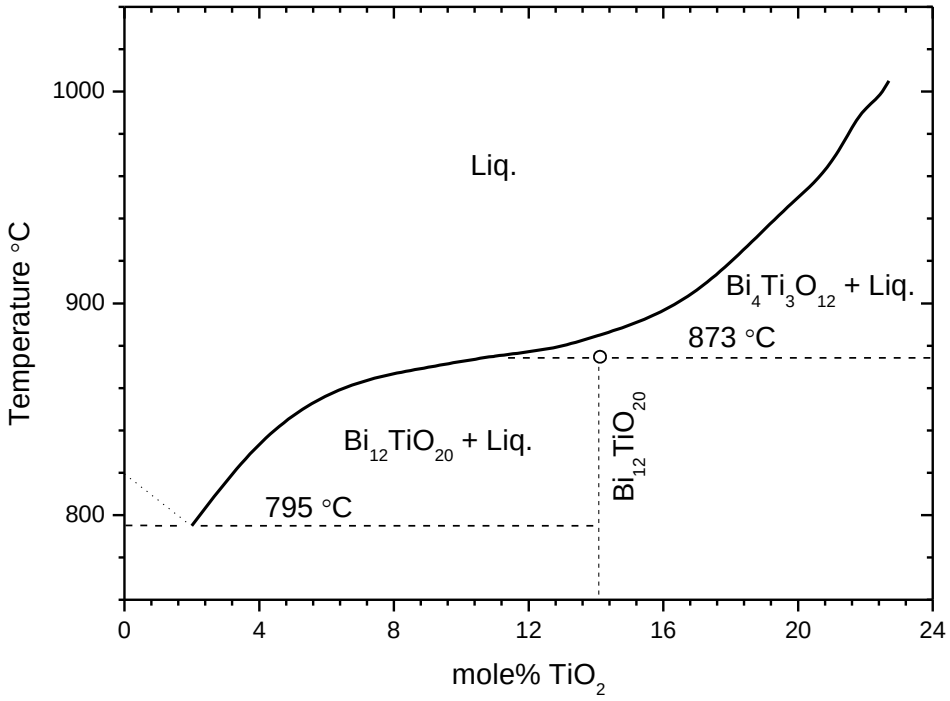

Figure 5-27 Bi_2O_3 - TiO_2 binary system phase diagram [101, 141]

It is also possible that Sb (III) is readily oxidised to Sb (V) state and Sb has partially taken over the role played by Ta (V) but more effectively. The property deteriorates in both directions from the main peak, but at all concentrations below y = 0.008, it achieves more than 20 pC N^{-1}.

Thermal depolarisation behaviour for the 0BITNTS, 8BITNTS and 10BITNTS compositions were studied by holding the samples for 2 hours at the annealing temperature, cooling them down to room temperature and then performing d_{33} measurements. The measurement temperature range was between 50 and 700 °C at increments of 50 °C. The characteristic behaviour of this material is consistent with that of other compositions studied in present work, and it is shown that d_{33} remains relatively stable up to 500 °C, beyond which the value begins to drop steeply and

eventually zeroes at the phase transition point T_c. This would suggest that BITNTS ceramic is a stable material which is suitable for applications up to 400 °C and fits in the primary requirements of base application for high temperature gas flow applications.

Figure 5-29 shows the influence of dopant composition on phase transition temperature. It is interesting to note a very small decrease of 8 °C for the entire range of dopant concentrations.

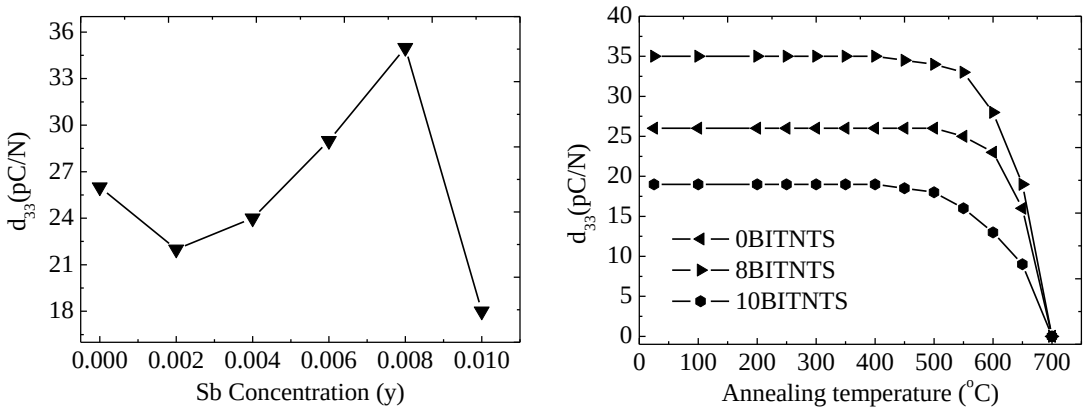

Figure 5-28 Piezoelectric coefficient (d_{33}) properties of BITNTS (left), and thermal annealing characteristics of polarised ceramics (right).

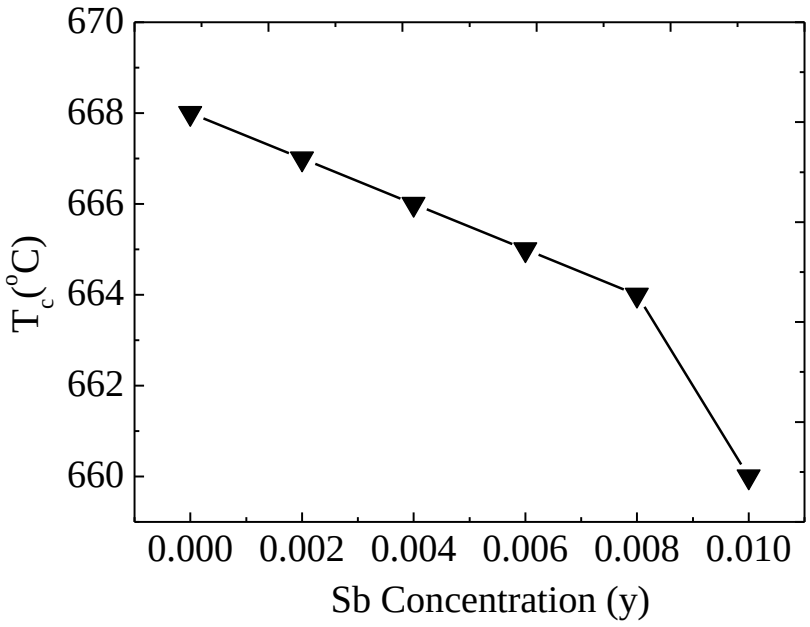

Figure 5-29 Effects of antimony concentration on Curie temperature in BITNTS. Linear decline is evident up to optimum concentration of y = 0.008 after which the step change increases. This could be viewed as an indicator of the optimum BITNTS composition reaching a saturation point and becoming less stable.

Given the intended application for BITNTS ceramics, the characterisation of electrical properties over appropriately wide frequency and temperature range is very desirable. 8BITNTS composition, having the most favourable piezoelectric properties, was investigated. Permittivity (ε′) of 8BITNTS is shown in Figure 5-30, measured at 100 kHz and 1 MHz, across a temperature range which includes the phase transition point at around 664 °C. It is interesting to note that a second peak at around 600 °C is also evident at both frequencies, suggesting a phase transition of a secondary 8BITNTS phase. To further elucidate this point, the differential scanning calorimetry (DSC) measurement was made for 8BITNTS over the relevant temperature range and the trace is shown in Figure 5-31. The primary phase transition point is a sharp peak at 664 °C, which is in strong agreement with the permittivity data. However, the 600 °C peak is missing, suggesting no secondary phase transition but an effect of AC field and a shift in charge mobility due to temperature.

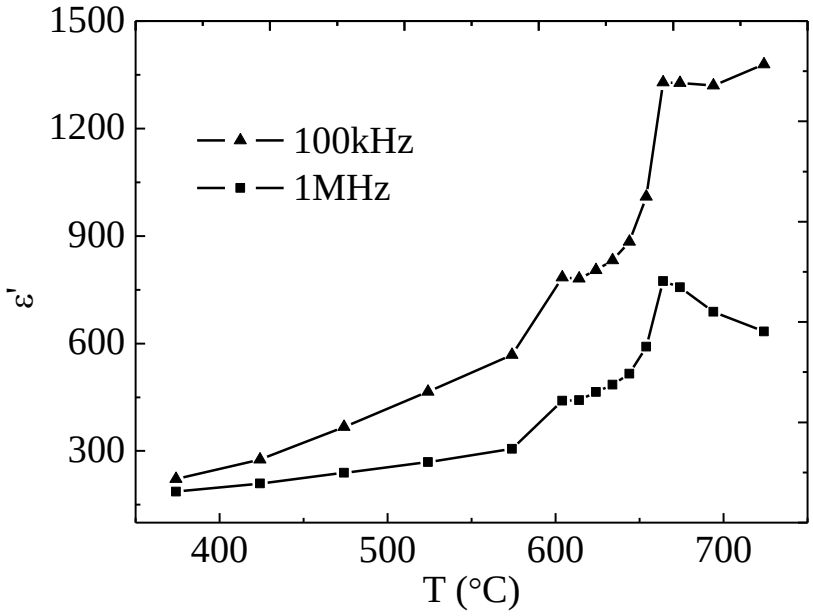

Figure 5-30 Permittivity of 8BITNTS at 100 kHz and 1 MHz, over wide temperature range including the phase transition point.

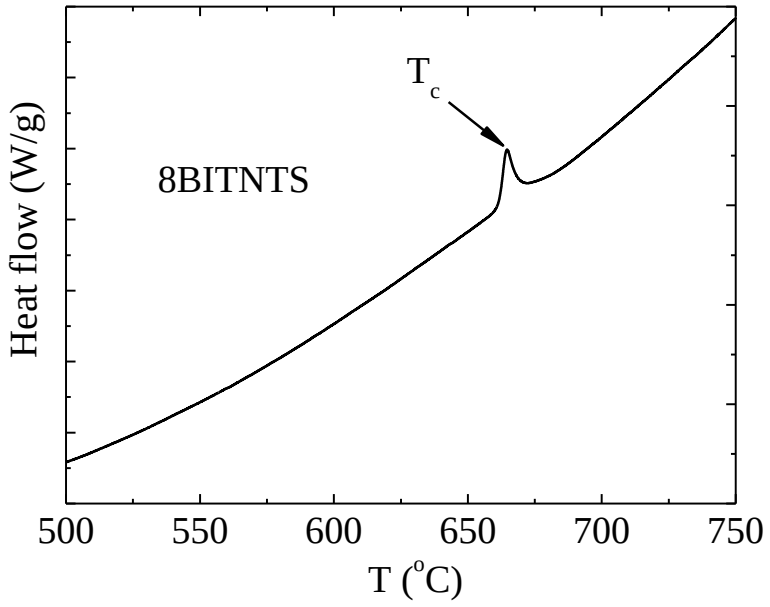

Figure 5-31 DSC trace showing an onset of phase transition in 8BITNTS. Missing peak at 600 °C, evident in permittivity data, may suggest that it was influenced by AC field rather then temperature mechanism other than phase change.

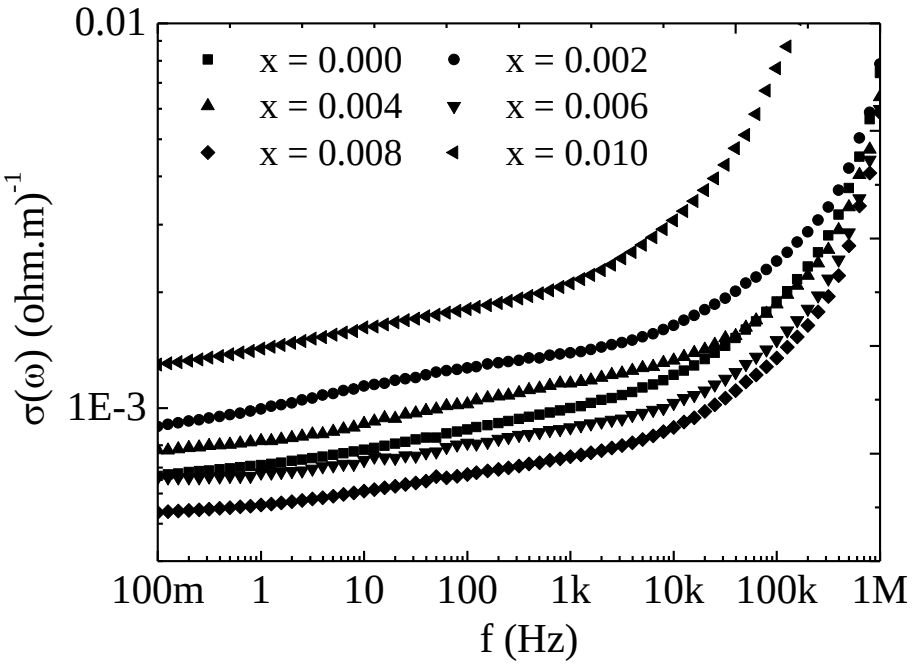

Figure 5-32 AC conductivity of modified BITNTS ceramic measured at 600 °C, from 0.1 Hz to 1 MHz at various dopant concentration.

Frequency dependant conductivity data, from 0.1 Hz to 1 MHz at 600 °C, is shown in Figure 5-32. Overall, the values are comparable to those measured in BITWC and BITNT at a given temperature and frequency range. It can be noted that AC conductivity in 8BITNTS is lowest up to ~ 500 kHz in frequency, after which the values tend to converge. The difference in values at lower frequency can be attributed to p-n conductivity type transition linked to varying dopant concentration and the arrangement of ions at the B-site. It has been shown in BITNT study that the p-type conductivity, typically observed in BIT, can be reduced by introduction of additional electrons through Nb and Ta doping. Antimony, having a +3 oxidation state in Sb_2O_3, and the ionic radius of 0.76 Å, is too large to fit into the B-site position occupied by Ti^{4+} with the ionic radius of 0.605 Å. However, previous reports show that Sb^{3+} is unstable above 500 °C [142], and can easily oxidise to Sb^{5+} in the presence of Bi_2O_3, with a better fitting 0.60 Å ionic radius.

Given the high sintering temperature of 1100 °C, it can be postulated that Sb^{5+} ions are easily accommodated at the Ti^{4+} sites, and data suggests that antimony does not impede the initial decrease in p-type conductivity in comparison to BITNT.

The increased concentration of antimony at the B-site also decreases oxygen vacancy, promoting domain wall movement and controlling the p-n type conductivity switch.

It is interesting to note the link between surface microstructure, shown in Figure 5-26, and the electrical properties of the BITNTS ceramic described above. It is evident that enhanced property 8BITNTS also has the largest grain size, and this is supported by literature [143], demonstrating that microstructure has a strong influence over electrical properties in bismuth titanate.

Decrease in electrical conductivity also produced more favourable polarisation conditions, allowing improvement in piezoelectric coefficient. This is possibly due to decrease in concentration of oxygen vacancies that can diffuse into the domain walls resulting in the lowering of the domain wall pinning and therefore increasing the number of available switching domain walls as well as the higher d_{33} value [93].

To gain further understanding of the mechanism, 8BITNTS AC conductivity measurements we obtained over temperature range between 300 and 600 °C and are shown in Figure 5-33. As would be expected, the conductivity increases with temperature due to thermal activation of conducting species in the ceramic and there is a hint of two relaxation frequencies in the plot. At the lower frequency, the conductivity can be attributed to the accumulative effect of both grains and the grain boundaries. With the increase in frequency, the grain to grain boundary contribution ratio changes and the grain contribution begin to dominate the high frequency range due to hoping of localised charge carrier. This can also explain the superior properties of 8BITNTS compared to other compositions, given the large grain size and hence lower volume of grain boundary. Dielectric and capacitive properties between grains and grain boundaries evidently contribute to AC conductivity, linked very strongly to the particular frequency range. Taking the present application into consideration and the maximum continuous operating temperature of 400 °C, it is interesting to note that the conductivity response at this temperature is relatively flat from very low frequency (almost DC), to 100 kHz. This is coincidentally the preferred frequency range for ultrasonic air transducers, due to lower losses associated with acoustic impedance of air.

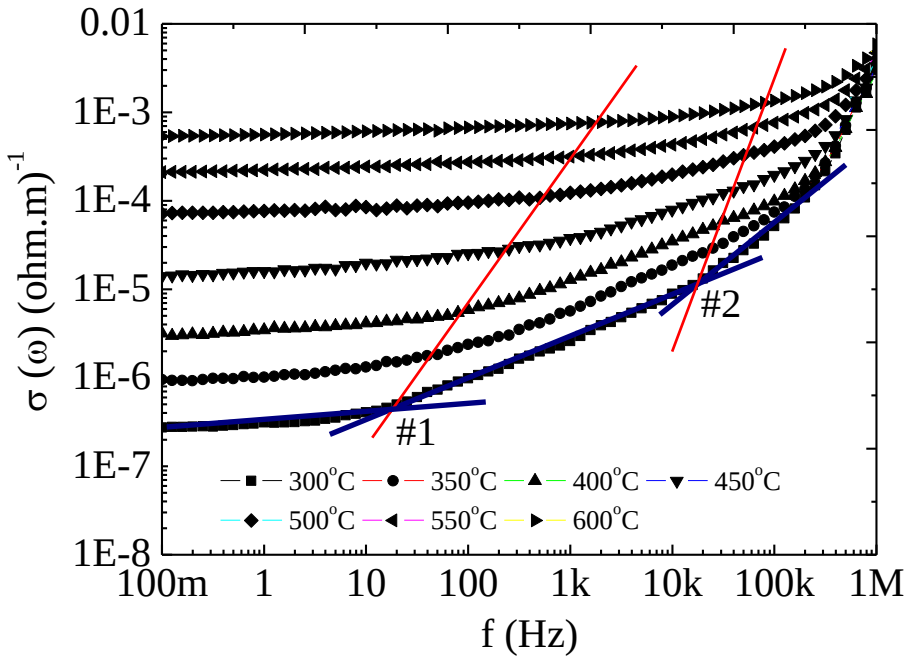

Figure 5-33 8BITNTS AC conductivity between 300 and 600 °C temperature range. Two relaxation frequencies are evident, shown as #1 and #2.

To further elucidate the electrical transport mechanism, the study of electric modulus for 8BITNTS was undertaken. This technique is useful for studying the relationship between conductivity and relaxation of ions in bulk dielectric materials.

The complex electric modulus (M^*) is generally defined as an inverse of the complex dielectric permittivity (ε^*);

$$M^* = \frac{1}{\varepsilon^*} = M' + iM'' = \frac{\varepsilon_r'}{(\varepsilon_r')^2 + (\varepsilon_r'')^2} + i\frac{\varepsilon_r''}{(\varepsilon_r')^2 + (\varepsilon_r'')^2} \qquad \textbf{Eq. 5-12 [144]}$$

where, M' and M'' and ε_r' and ε_r' are the real and imaginary parts of the electric modulus and dielectric permittivity, respectively.

The effects of electrode polarization and the electrical conductivity can be suppressed using the electric modulus formalism, where real and imaginary parts of the modulus for 8BITNTS at different temperatures are calculated using Eq. 5-12. Plots of M' and M'' are shown in Figure 5-34.

It is evident that at near DC frequencies, the real electric modulus has a negligible magnitude and this is the case for all temperatures under consideration. This suggests that the effects of electrode polarisation are suppressed.
With the increase in frequency, M' peaks in magnitude due to the relaxation process and the role of temperature appears to be in shifting the frequency response and hence decreasing the value of M'.

The imaginary part of the electric modulus is indicative of the energy loss under electric field. With the increase in temperature, the M'' peak shifts to higher frequencies, and this suggests the presence of temperature-dependent relaxation in the 8BITNTS ceramic. The peaks which are evident in M'' plots are indicative of the frequencies at which long range ion oscillation is most active. Above these frequencies, the ions are spatially confined to potential wells and free to move only within the wells themselves.

The activation energy involved in the relaxation process of ions can be obtained from the temperature dependent relaxation frequency (f_{max}) as:

$$f_{\max} = f_o \exp\left(-\frac{E_R}{kT}\right) \qquad \textbf{Eq. 5-13}$$

where E_R is the activation energy associated with the relaxation process, f_o is the pre-exponential factor, k is the Boltzmann constant and T is the absolute temperature.
Figure 5-35 shows the $\ln(f_{max})$ versus $1000/T$ plot with a theoretical fit to Eq. 5-13, and the value ascribed to the motion of oxygen ions is calculated at E_R = 1.0 eV.
The value of activation energy for 8BITNTS ceramics is higher than that of activation energy for pure BIT, and this is an indication of the reduction of oxygen vacancies, due to the fact that the hole compensation of bismuth vacancies promotes p-type electronic conductivity.

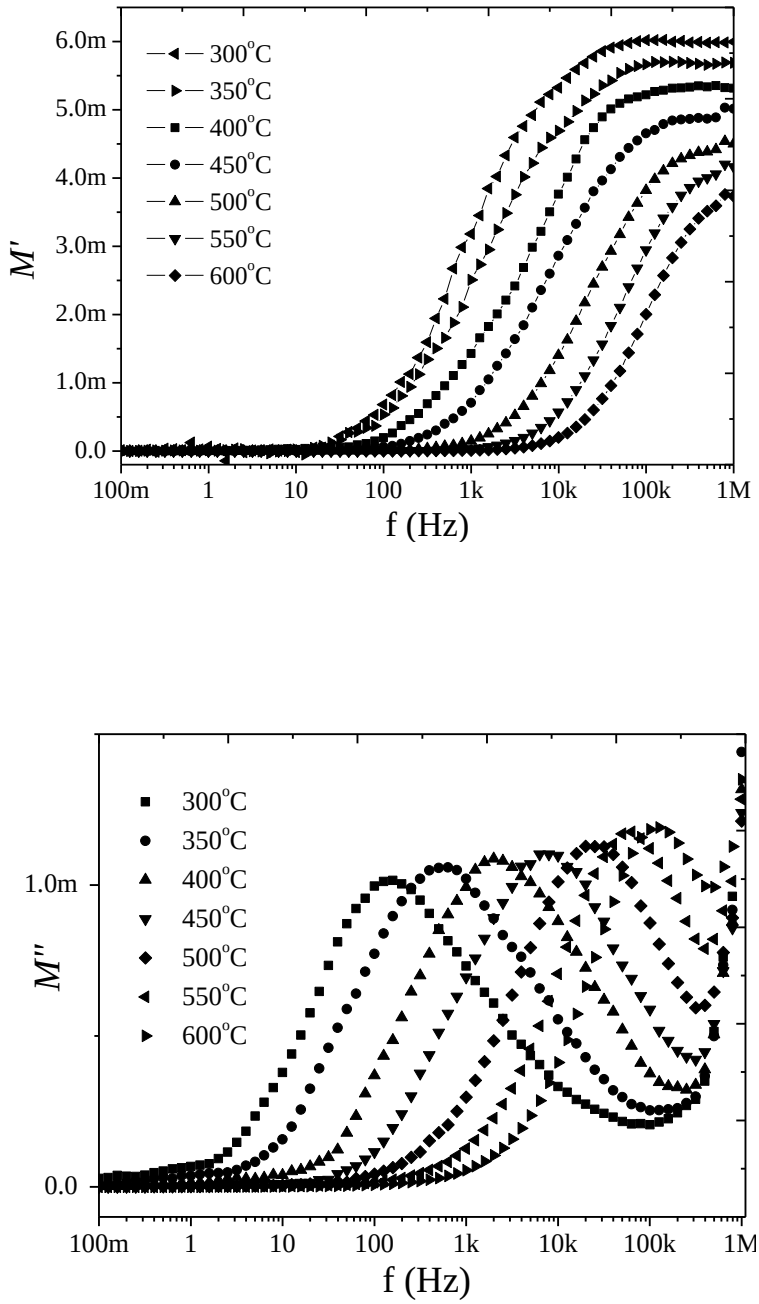

Figure 5-34 Real (***M'***) and imaginary (***M''***) parts of the 8BITNTS electric modulus as a function of frequency and at different temperatures.

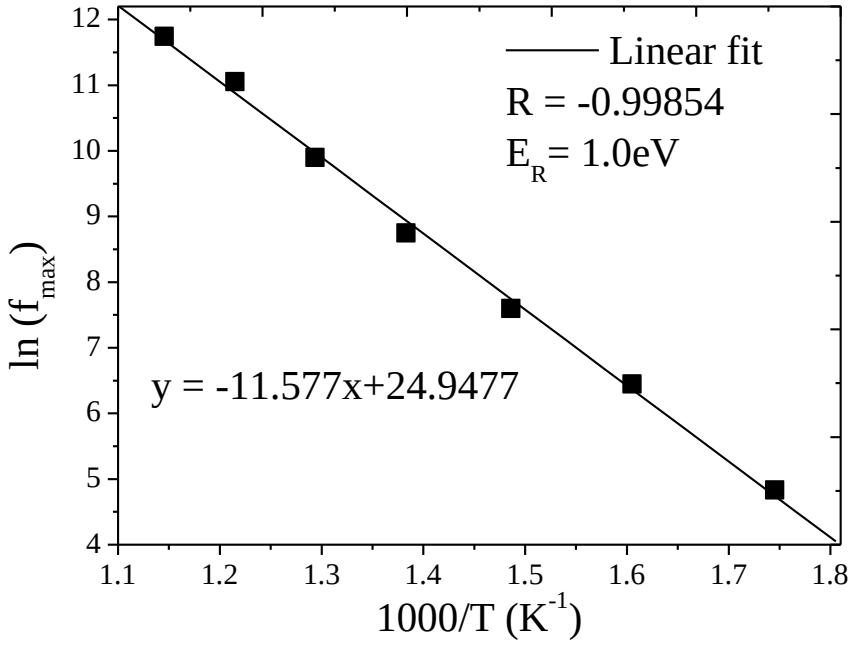

Figure 5-35 $\ln(f_{max})$ versus $1000/T$ for 8BTNTS ceramic.

The electric modulus can also be expressed as the Fourier transform of a relaxation function $\phi(t)$:

$$M^* = M_\infty \left[1 - \int_0^\infty \exp(-\omega t) \left(-\frac{d\phi}{dt} \right) dt \right] \qquad \textbf{Eq. 5-14}$$

where the function $\phi(t)$ is the time evolution of the electric field within the materials and is usually taken as the Kohlrausch-Williams-Watts (KWW) function [145, 146]:

$$\phi(t) = \exp\left[-\left(\frac{t}{\tau_m}\right)^{\beta}\right] \qquad \textbf{Eq. 5-15}$$

where τ_m is the conductivity relaxation time and the exponent β ($0 < \beta < 1$) indicates the deviation from Debye type relaxation. The lower β indicate larger deviation from Debye-type relaxation and when β is close to zero, there is a strong correlation between the hopping ions and their neighbouring ions. The β was calculated for different temperatures using the electric modulus formalism. For the ideal Debye type relaxation, the full-width half maximum (FWHM) of imaginary part of electric modulus is 1.14 decades. Therefore, β can be defined as 1.14/FWHM. One can estimate DC conductivity at different temperatures using the electrical relaxation data and it can be expressed as;

$$\sigma_{DC}(T) = \frac{\varepsilon_o}{M_\infty(T) \times \tau_m(T)}\left[\frac{\beta}{\Gamma\left(\frac{1}{\beta}\right)}\right] \qquad \textbf{Eq. 5-16 [147]}$$

where ε_o is the dielectric permittivity of vacuum, $M_\infty(T)$ is the reciprocal of high frequency dielectric permittivity and $\tau_m(T)$ is the temperature dependent relaxation time. This equation is applicable to a variety of materials with low concentrations of charge carriers [148, 149].

Figure 5-36 shows the DC conductivity obtained by the expression given in Eq. 5-16 for selected temperatures and the plot $\ln(\sigma_{DC})$ versus $1000/T$ for 8BITNTS.
The linear conductivity response in temperature domain is evident and is fitted using the following Arrhenius equation:

$$\sigma_{DC}(T) = B\exp\left(-\frac{E_{DC}}{kT}\right) \qquad \textbf{Eq. 5-17}$$

where B is the pre-exponential factor and E_{DC} is the activation energy for the DC conduction.

The activation energy is calculated from the slope of the fitted line and found to be 1.08 ± 0.02 eV. This value for activation energy is in close agreement with the activation energy for electrical relaxation.

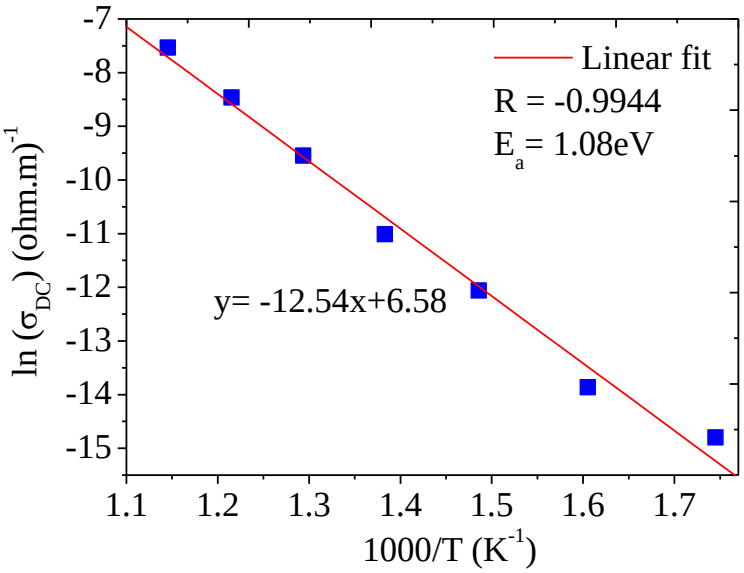

Figure 5-36 $\ln(\sigma_{DC})$ versus 1000/*T* for 8BITNTS ceramics

Figure 5-37 shows the normalized plots of electric modulus M''/M''_{max} versus frequency, where the frequency is scaled by the peak frequency, f/f_{max}.

A perfect overlap of all the curves on a single master curve is not found, indicating that the conduction mechanism is changing with temperature, which is in good agreement with literature reports [123]. Takahashi et al. [123] reported that BIT exhibits mixed (ionic-p-type) conduction at high temperature and ionic conductivity was larger than hole conductivity in Curie temperature range above 600 °C.

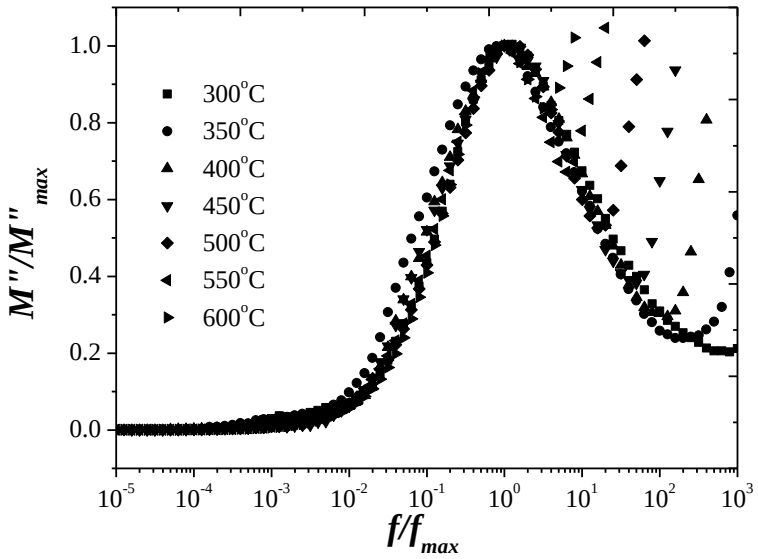

Figure 5-37 Normalized plots of electric modulus against normalized frequency at various temperatures for 8BTNTS ceramic

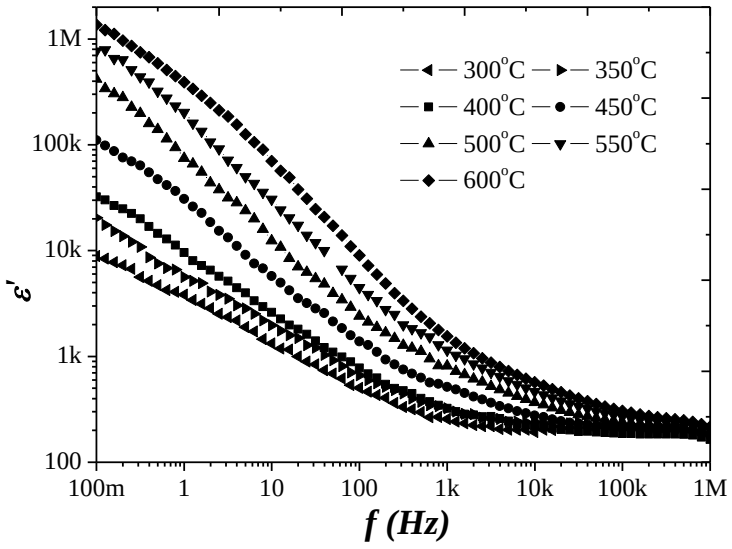

Figure 5-38 Frequency response of the dielectric permittivity for 8BITNTS

Figure 5-38 shows the frequency dependence of dielectric permittivity (ε′) at various temperatures for 8BITNTS. Evidently, the value of ε' is decreasing in with frequency and eventually converges for all temperatures under consideration above 100 kHz. Increased magnitude of ε′ at low frequencies is an extrinsic phenomenon which arises due to the presence of metallic electrodes, which do not permit the mobile ions to transfer into the external circuit. As a result, mobile ions concentrate near the electrodes and give a large bulk polarisation at grain boundaries. When the temperature rises, the dispersion region shifts towards higher frequencies and the nature of the dispersion changes at low frequencies due to the electrode polarization along with grain boundary effects.

The variation in the tan δ with the temperature at various frequencies (Figure 5-39) is consistent with that of the dielectric behaviour. The dielectric loss consistently decreases with the increase in frequency, and increases with the increase in temperature, which can be attributed to increased conductivity of the ceramic due to thermal activation of conducting species. Due to high DC conduction losses at low frequencies, a strong relaxation peak could not be identified.

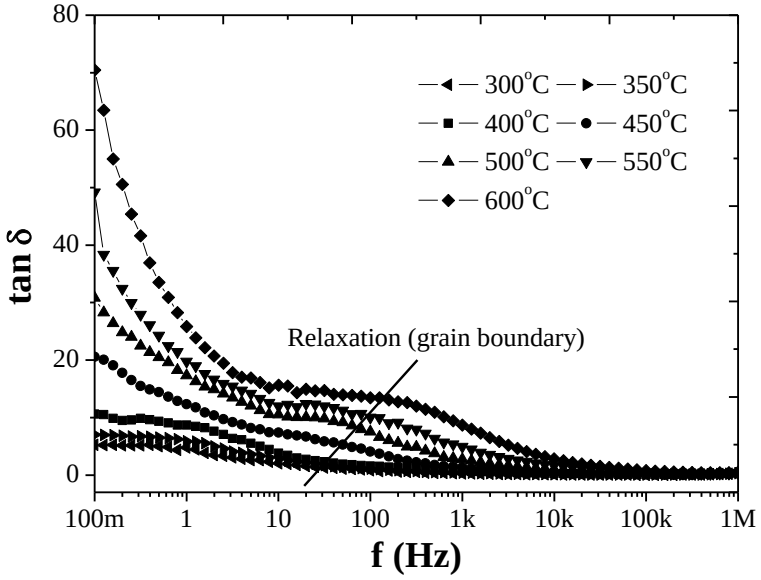

Figure 5-39 Dielectric loss versus frequency at selected temperature for 8BITNTS.

Chapter 6 High Temperature Ultrasonic Transducer

6.1. Introduction

In the following section, a number of key aspects of high temperature transducer design for gas flow sensors are characterised based on laboratory and field experiments, in order to provide the foundation for further development of a practical ultrasonic transceiver device suitable for operating at high temperature.

The aims of this chapter are to:

- Characterise some key properties of commercial ultrasonic air transducers based on PZT piezoelectric materials and evaluate the effects of contamination and high temperature on commercial ultrasonic transducers.
- Discuss the development of a high integrity ceramic-steel bond for ultrasonic transducer assemblies that can incorporate doped BIT piezoelectric material.

6.2. Dynamic Transducer Behaviour and the Factors Affecting Stability

An ultrasound transducer is by definition an electro-mechanical oscillating device, converting electronic stimuli into mechanical vibration, which in turn forms periodic pressure waves in air or another medium. The efficiency of such a conversion is never unity, and varies widely with frequency and other thermo-mechanical factors. The frequency at which the transducer is most efficient is called the resonant frequency, f_r, and transducers are generally designed to operate at a specific frequency which best suits the application.

An ultrasonic transducer which is operating at its resonant frequency can be schematically represented by the equivalent circuit shown in Figure 6-1 **Equivalent circuit of an ultrasound transducer operating at or near its resonant frequency and the definition of relevant terms [150].**

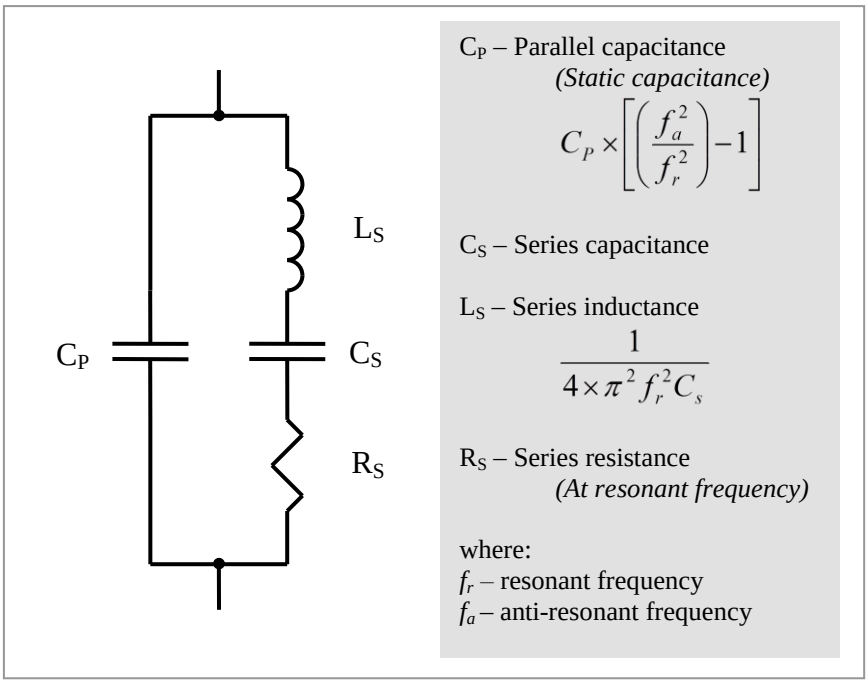

Figure 6-1 Equivalent circuit of an ultrasound transducer operating at or near its resonant frequency and the definition of relevant terms [150].

The resonant frequency of a transducer can be predicted by;

$$f_r = \frac{1}{2\pi}\sqrt{\frac{1}{L_S C_S}} \quad \text{[Hz]} \qquad \textbf{Eq. 6-1}$$

f_r is therefore the frequency at which the series impedance of the transducer is at a minimum and equal to the value of R_s.

To achieve this state, the inductive and capacitive reactances have to be of equal magnitude but opposite in sign. The resonant state is approached from low frequency with the current phase angle leading the voltage, $(-X_C) > X_L$. As the frequency approaches the resonant point, the absolute magnitude of the reactances equalise, and the series impedance ($Z_S = Z_C + Z_L$) achieves the minimum value. When the frequency increases beyond f_r, the phase angle passes through zero and the current begins to lag the voltage, $(-X_C) < X_L$, making the circuit more inductive in nature. This of course is the case for the fundamental resonant frequency as well as for all overtones at higher frequencies.

In certain applications such as automotive parking sensors, the shift in the characteristic resonant frequency due to temperature variations for example, can be monitored and appropriate adjustments can be made in excitation frequency in order to compensate for any change in environmental conditions and to achieve the maximum device efficiency. For the present application however, it is necessary for two or more transducers to interface from physically different locations, in an aggressive environment and to closely maintain matching of their resonant frequencies. To characterise the ultrasound transducer and further define the factors influencing the resonance, an impedance study was carried out on a commercial transducer, having closed construction and a nominal resonant frequency of 32.8 kHz.

6.2.1. Impedance Measurements

Room temperature impedance measurements were carried out on a Prowave 328ET250 transducer, having an aluminium body and a PZT based actuator, using a Solartron SI 1287 impedance spectrometer. The transducer was suspended via its electrodes in such a way that no stress or strain was exerted on the sample and measurements were taken between 23 kHz and 43 kHz using a 1 V(rms) source.

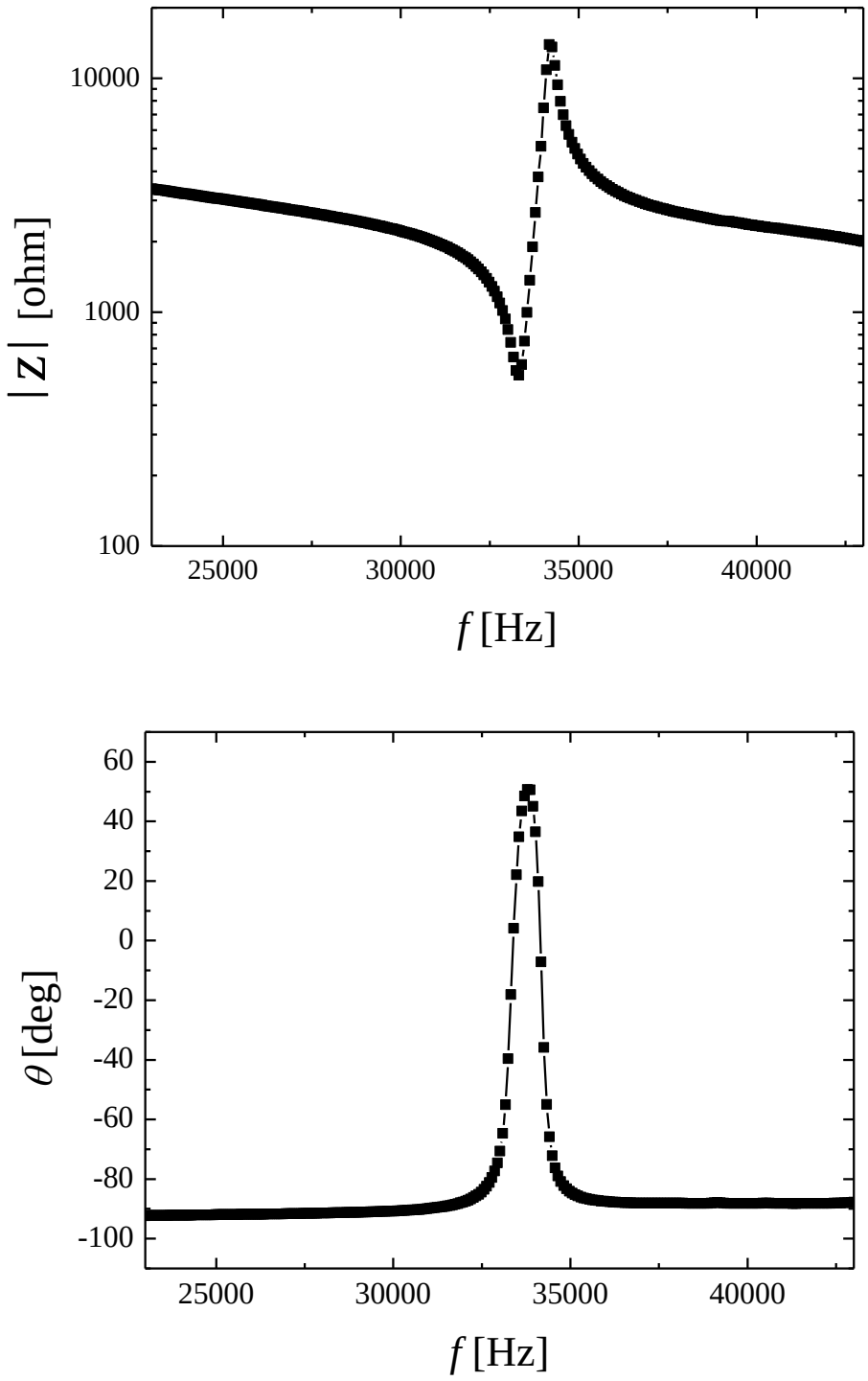

Figure 6-2 Figures showing absolute impedance, |Z|, response over the frequency range encompassing the fundamental resonant frequency (top) and the phase angle, θ, (bottom) for a PZT based transducer.

The impedance response of the transducer through its fundamental resonant frequency is shown in Figure 6-2 and the phase angle trace clearly demonstrates the transition between capacitive and inductive circuit response. This data is in general agreement with published performance of such commercial devices [151] having closed construction.

The steepness of the edges of both the impedance and the phase angle curves indicates a very narrow response bandwidth, making the transducer intolerant to shifts in excitation frequency or characteristic resonant frequency. This type of response is appropriate for applications where the operating conditions are relatively stable and low particulate concentration is guaranteed, yielding very efficient power conversion and hence low impedance values at resonance. For applications with increased particulate concentration and operating conditions where number of parameters can change simultaneously, a broad bandwidth device is more appropriate. This is typically achieved using damping loads and materials, but in practice accumulation of solids on the surfaces of the transducer can have a significant influence on the dynamic behaviour. The parameter used to quantify this behaviour is the mechanical quality factor (Q_m) and is given by;

$$Q_m = \frac{f_a^2}{2 \times \pi \times f_r \times |Z| \times C \times \left(f_a^2 - f_r^2\right)} \qquad \textbf{Eq. 6-2}$$

Where f_a and f_r are resonant and anti-resonant frequencies respectively, |Z| is the absolute impedance and C is the static capacitance. Generally, the higher the value of Q_m the narrower the bandwidth of the transducer. Higher bandwidth devices generally have an open construction where the piezoelectric actuator is partially exposed to the environment. However, for obvious reasons, this type of device is not appropriate for industrial application sought in this project and a suitable compromise on a closed construction device needs to be investigated.

It is well known that a major contributor to changes in the resonant behaviour of such a transducer is a shift in the mechanical boundaries, applied dynamically during the lifecycle of the device. Considering the present application, solid particulate

contamination is the main expected contributor of resonance shifts and some analysis of device immunity and resilience to such operational threats is appropriate. To analyse the effects of contamination build up on a closed construction device, two tests were carried out in the laboratory on a Prowave 328ET250 device. Initially, the device was mechanically loaded in order to simulate the contamination whilst monitoring the shift in resonance frequency, followed by an investigation of the self cleaning properties of the device under extreme particulate concentration.

6.2.2. Resonance Shift with Contamination

To evaluate the effects of contamination build up on the face of an ultrasonic transducer, the transmitting face of the transducer was loaded with artificial loads representing solid contamination. Figure 6-3 shows the impedance and phase angle traces representing *a*) no load, *b*) a 50 μm nylon film over the face of the transducer, *c*) 55 g of putty over one side of the transducer face and *d*) 55 g of putty spread from the centre of the transducer face. Trace *a* is the reference and represents the clean transducer. Magnitudes are comparable to those published in manufacturers data sheets [151], giving a transducer bandwidth of 1 kHz. With the nylon film placed over the face of the transducer in order to simulate fly ash caking, commonly found in large combustion plants, it is evident that the magnitude of |Z| is reduced both at resonant and at anti-resonant frequencies, whilst the resonant frequency itself has shifted to a value approximately 450 Hz lower than the reference. Although the impedance curves are slightly broader, the transducer response still has a narrow band response. In applications with a moderate presence of liquid water combined with fine solid particles, common with wet type scrubber based filtration systems; the contamination tends to have more clay type consistency and agglomerates in thick globules which depending on the presence of turbulent flow can either produce a uniform or patterned spread. A 55 g load of clay putty was used as an artificial load and traces *c* and *d* show the transducer response under these conditions. In both instances the magnitude of |Z| is considerably reduced and there is a significant shift in resonant frequency, particularly for trace *d*. The resonant frequency of the reference (*a*) is measured at 33.398 kHz and |Z| = 166 Ω. Taking the nominal transducer bandwidth of 1 kHz into consideration, and the resonant frequency shift of

the *c* sample down to 31.675 kHz and |Z| = 1763 Ω, it suggests that there is a tenfold decrease in signal magnitude from a transducer having this type of contamination on it. This is particularly relevant for operation on large diameter stacks.

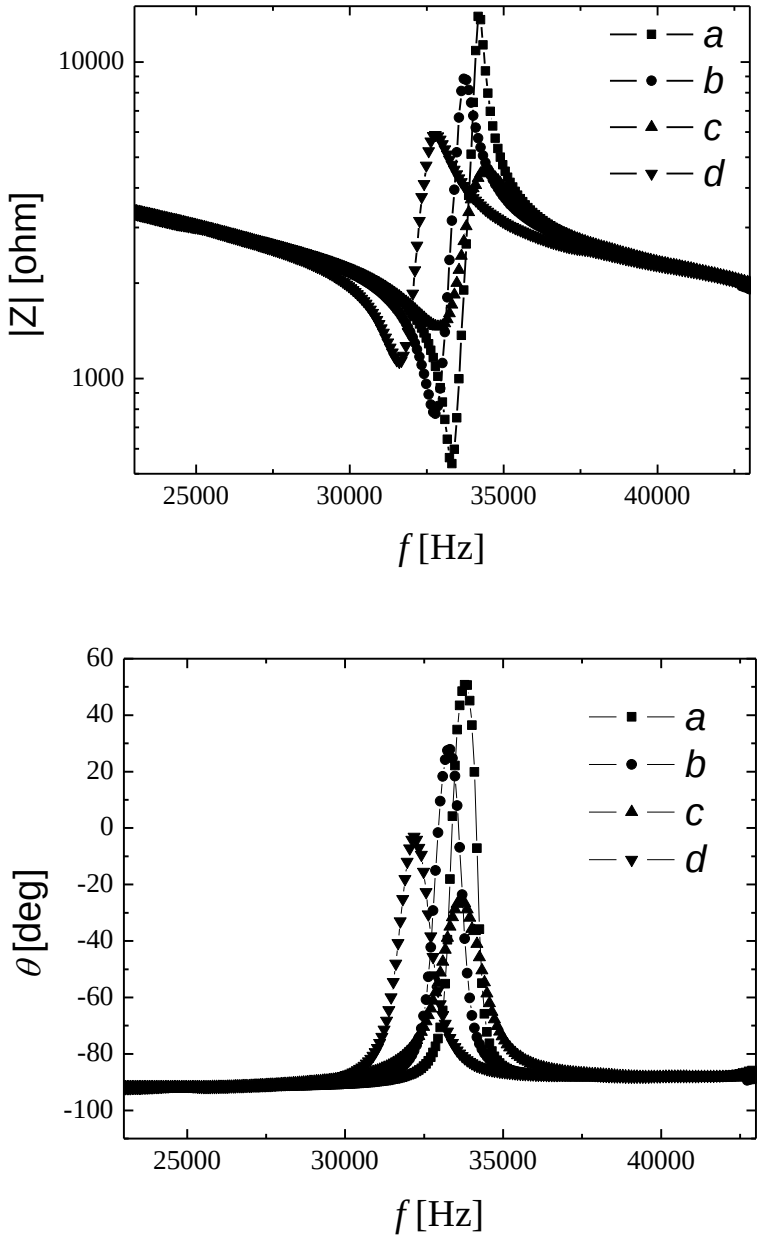

Figure 6-3 Impedance (|Z|) and phase angle (θ) shift of a transducer with:

a No load
b 50 μm nylon film over the face of the transducer
c 55 g of putty loaded on one half of the transducer face
d 55g of putty loaded in the centre of the transducer

6.2.3. Self Cleaning Properties of Ultrasound Transducers

The main objective of this experiment was to analyse the effect that presence of dust within the flue gas will have on the long term reliability of an ultrasonic transducer installed as a part of the gas velocity monitor in an industrial smokestack. As discussed in the previous sub-chapter, dust accretion on the transducer face is of particular concern as this could make non-purged instruments not viable for applications where high levels of particulate contamination were present. Ultimately, a full field trial would benefit this study, but to further the understanding of the contamination mechanism, a controlled laboratory experiment was pursued. Based on previous field experience, an experiment was set up where the commercial Prowave 328ET250 ultrasound transducer was exposed to a gas stream, having a velocity of around 20 m s^{-1} and fine alumina particles suspended in the flow. Gas flow and velocity were controlled using a pressure and flow gauge shown in the figure below.

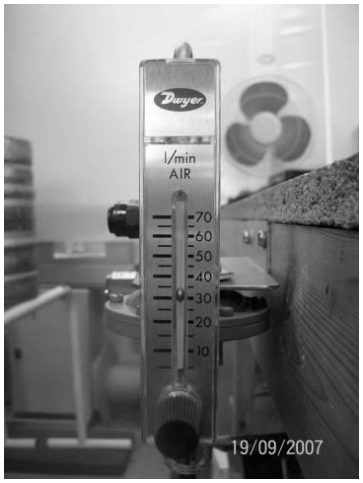

Regulator Setting [bar]	Resulting Flow [l/min]	Resulting Gas Velocity [m/s]
0.0	0	0.0
0.2	11	9.3
0.4	18	15.3
0.6	24	20.4
0.8	30	25.5
1.0	35	29.7
1.2	40	33.0
1.4	42	35.7
1.6	43	36.5
1.8	45	38.2
2.0	45	38.2

Figure 6-4 Tube flow metre with a pressure regulator shown behind it. Values for flow and velocity are shown and were experimentally determined in order to gain better control of particulate concentration.

Figure 6-5 The Palas dust feeder is a dosing instrument which allows for precise feed rate of solid particles, aided by a compressed air supply, shown on the right.

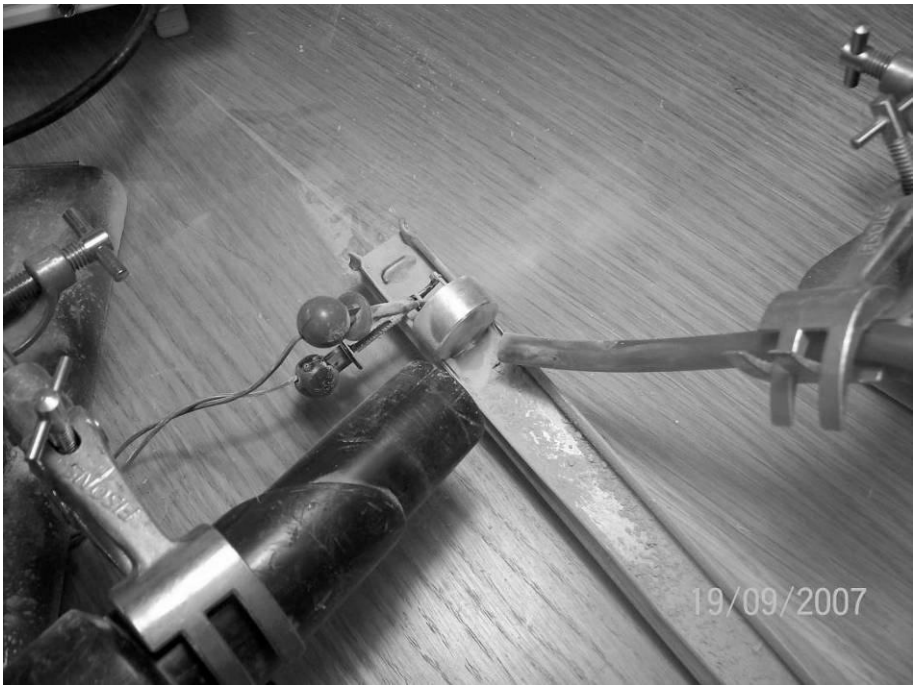

Figure 6-6 Experimental setup showing the transducer in the centre, extraction hose to the left and the gas and particulate feed on the right (via the tube).

The Palas feeder, shown in Figure 6-5, was loaded with F1200 Al_2O_3 particles with a nominal diameter range between 3 and 4.5 µm. Other types of particulates were experimentally evaluated and F1200 was found to adhere to all surfaces easily and was representative of typical fly ash characteristics. The concentration of F1200 during the experiment was adjusted to 400 mg/m^3, ± 5 %, and the supply of air and dust was kept on constantly throughout the test. As shown in Figure 6-6, the gas/particulate mixture was directed at the face of the transducer. The excess particulate was safely extracted with the hose (shown on the left in the image).

The 328EP250 ultrasonic transducer was driven with an excitation signal of 32.8 kHz and 20 V p-p (sine wave) using a TTI TG4001 function generator. The transducer was evaluated by simulating the typical pulsed operation, but with exaggerated cycle times which were fixed at 15 seconds. The transducer was switched off for 10 seconds, during which period a large amount of particulate build up on the face of the transducer. This was followed by a 5 second active period during which the ultrasonic vibration would firstly break down and then disperse all of the particulate built up on the transducer. Contamination was observed to be more prevalent in areas with sharp corners and machining grooves as the transducer surfaces were not polished.

After 30 minutes of operation, the experiment was stopped and the transducer was visually examined. It was noted that aluminium body of the transducer was clearly deformed and eroded due to abrasive properties of alumina particles. Prolonged exposure to this type of dust would lead to ultimate transducer failure.

This emphasises the requirement for a transducer with steel construction.

6.3. High Temperature Bonding and Assembly of Ultrasonic Transducers

In this section, work conducted on the development of a suitably high temperature bonding method that could be used to form an electrically and thermally stable joining layer between stainless steel and BIT piezo-ceramic is discussed.

Conventional bonding techniques using commercially available, conductive adhesives were highlighted in chapter 2 as not suitable for high temperature continuous use for reliability reasons, such as delamination. Similarly, previous reports on brazing methods did not cover long term and field reliability at high temperatures or thermal cycling.

In the present work, two avenues are explored in order to address this issue. Initially, experiments were carried out to evaluate the suitability of the brazing method for producing a thermally stable and highly ductile conductive bond between the alumina ceramic and steel, which is capable of continuous operation above 400 °C.

An alternative and novel method for transducer assembly, using liquid gallium trapping is also evaluated.

6.3.1. Metallic Foam Brazing

Shirzadi *et al.* [34] reported a successful brazing method for joining stainless steel and the alumina ceramic using filler metals and metallic foams. The filler is chosen to provide good adhesion to both substrates, whilst the foam acts as a buffer, taking out differential of thermal expansion between the two materials. The resulting joint exhibits improved resilience against delamination due to thermal gradients.

The thermal instability of ferroelectric materials is most pronounced during the sintering process where, as could be expected, densification-induced shrinkage has a significant influence on the size and shape of the sample. Sintering experiments conducted on a dilatometer and using calcinated green powder, based on the pellet preparation procedure described previously, show that up to 15 % volume shrinkage occurs upon sintering. This of course is greatly dependant on the pressure used to form the pellet and volume content of volatile impurities. Figure 6-7 shows the BIT behaviour during and after sintering.

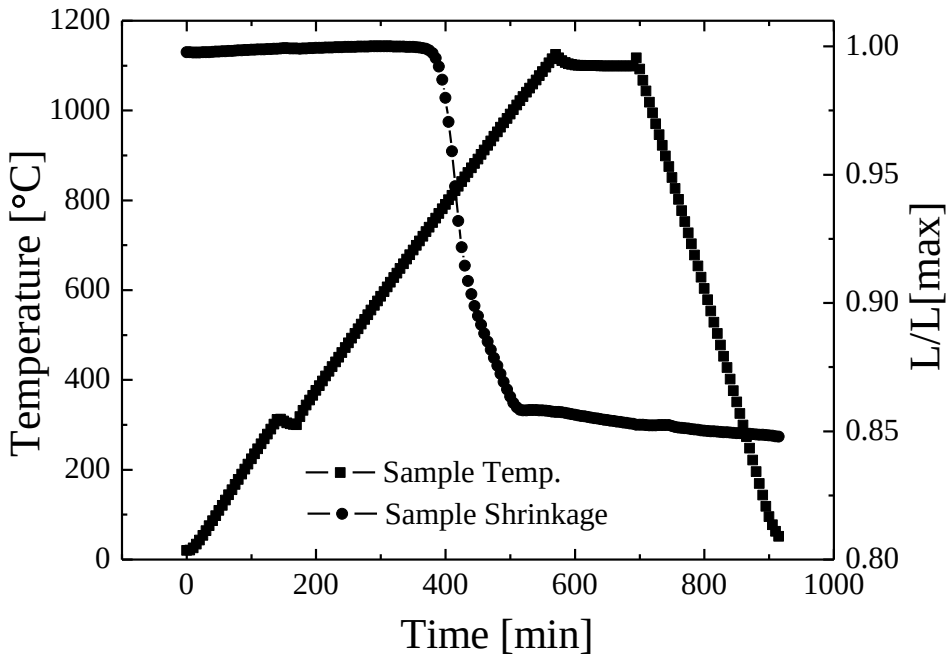

Figure 6-7 Thermal instability of BIT ferroelectric during and after sintering. Densification which occurs between 800 and 1000 °C results in most of the shrinkage of the sample under test, whilst the cooling period after densification exhibits < 1 %.

The important parameter for the present application is the post-densification behaviour of BIT and the influence it may have on the bond formed with stainless steel. The thermal linear expansion coefficient of BIT during the cool down period was measured at 13.96 [10^{-6} K^{-1}], close to the previously reported figure of 14.11 [10^{-6} K^{-1}] [152]. This is slightly less than the coefficient of stainless steel (316L) at 16.5 [10^{-6} K^{-1}] [153].

Brazing filler was selected with a coefficient of 18.5 [10^{-6} K^{-1}], based on titanium (4.5 %), copper (26.7 %) and silver (68.8 %) alloy. Given the relatively comparable values of thermal expansion coefficient for all three materials, experiments were conducted without the metallic foam to assess the bond strength and chemical compatibility between the different materials. Figure 6-8 shows the experimental setup for the brazing of stainless steel and BIT.

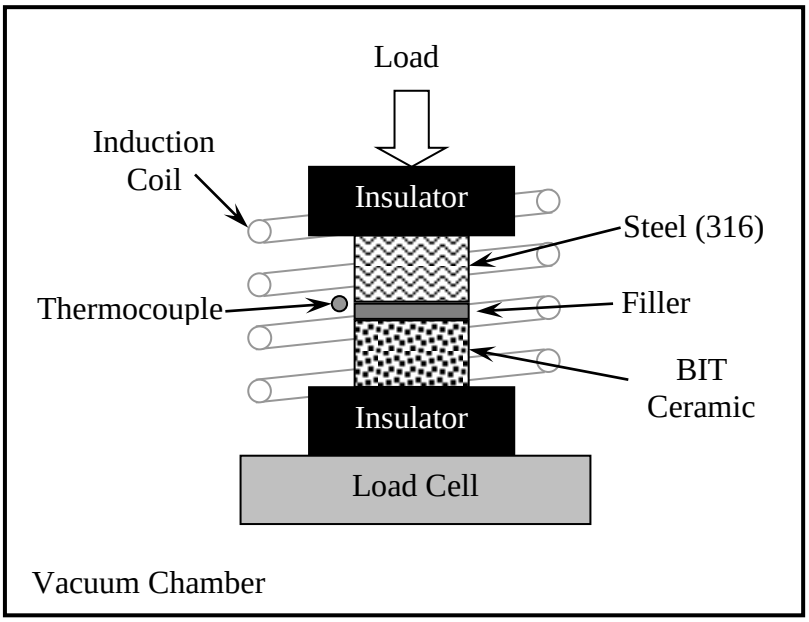

Figure 6-8 Experimental setup for brazing stainless steel and BIT ceramic in the vacuum, pressure assisted furnace. The filler was Ticusil®, manufactured by Wesgo.

Brazing filler (< 100 μm foil) was placed on top of the BIT cylinder, having a diameter of 10 mm and a length of 4 mm. It was then topped with a 10 mm stainless steel stainless stub and the assembly was placed inside an induction heated vacuum furnace. A small load was placed on the top of the assembly to ensure an intimate interface between all components. The sample was then heated up under vacuum to 950°C, slightly above the melting point of the filler, at a ramp rate of 200°C/min. After a 1 minute dwell time, the sample was then rapidly cooled at a rate of 200°C/min. Fast heating and cooling rates are necessary to reduce the reaction times between different sample constituents.

On visual inspection, the filler appeared to have wetted well to both steel and the BIT, with notably smooth fillets around the edges. Black staining on some areas of the interface was also noted. To further investigate the integrity of the whole steel/BIT interface, the sample was sawn in half using a diamond blade and SEM images were taken. Figure 6-9 shows the SEM images of the steel/BIT interface.

All four images demonstrate good wetting with the filler, forming smooth fillet interfaces at the edges of the assembly. However, the areas on the outer edges appear porous and inconsistent in width, with the BIT eroded in appearance. The narrow width of the filler layer in the middle of the sample, shown in c, suggest a large thermal gradient across the sample during heating with the outer edges being exposed to a considerably higher temperature. This effect is common with induction heating processes, where the outer surfaces are heated by the magnetic field, whist the inner body is heated mainly by conduction. In the experimental setup, the stainless steel cylinder is heated inside an induction field, causing a thermal gradient to develop from the outside towards the centre. Heat is transferred through the filler and into the BIT ceramic. The apparent erosion of BIT could be ascribed to diffusion of the bismuth oxide layer from BIT into the titanium-rich filler alloy, changing the composition at the interfaces. The presence of black stains around the filler material also suggests the formation of additional phases.

Although an electrically conductive and mechanically strong bond has been successfully established between steel and BIT, the reaction induced porosity at the interface does not facilitate the intimate contact required for the present application.

Subsequent experiments based on different ramp rates and filler compositions did not yield desirable improvements to this method.

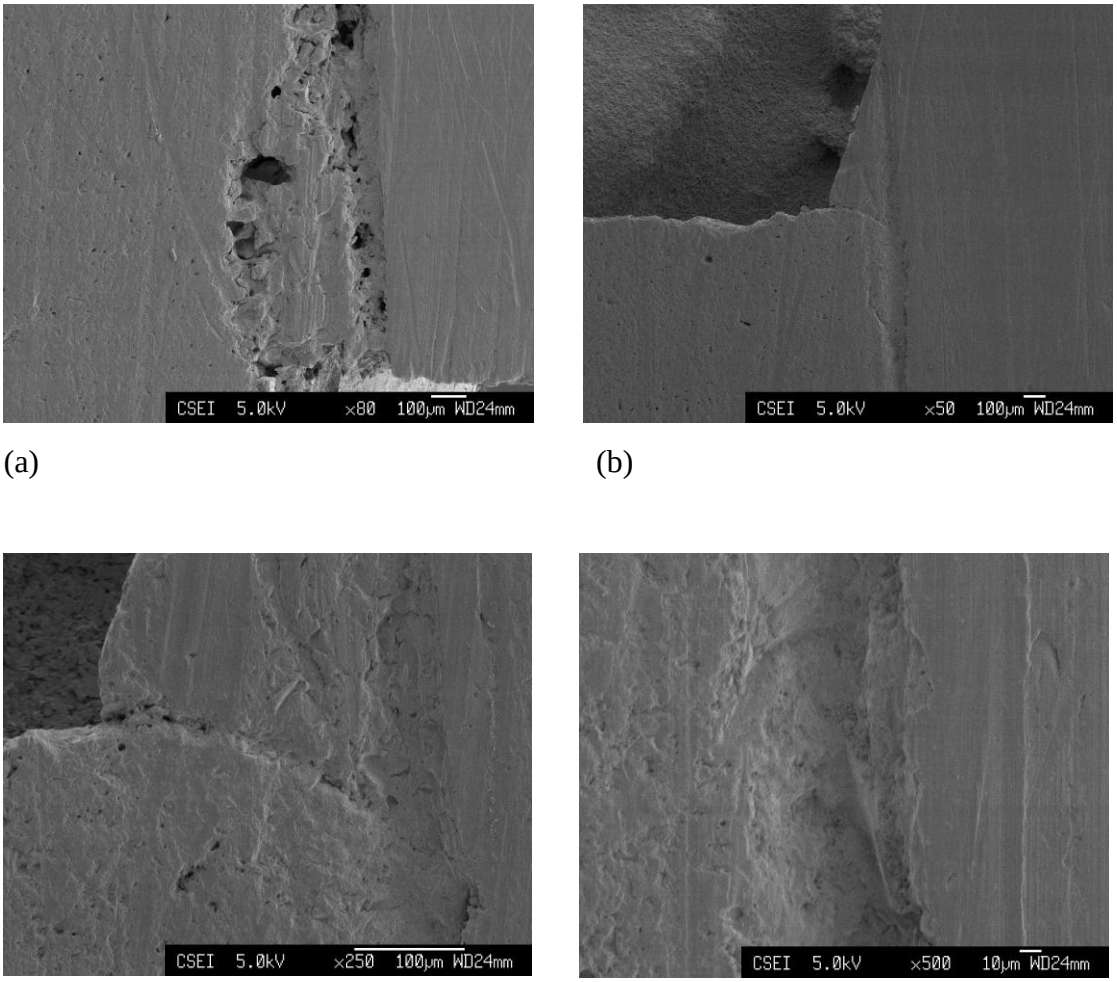

(a) (b)

(c) (d)

Figure 6-9 SEM Images of the braze joint between the BIT ceramic and the stainless steel stub. Images a, b and c show the edges, whilst d is the central section of the sample.

6.3.2. Gallium Trapping Assembly Method

An alternative method for the assembly of transducers using liquid gallium [UK Patent application 1016490.3 - Cambridge Joining Technology Ltd.] as a conductivity path between the ceramic and the stainless steel with mechanical entrapment of the piezoelectric actuator is evaluated in terms of mechanical integrity, capacitance (C) and absolute impedance (|Z|).

6.3.2.1. Experimental Setup

In the present method, liquid phase Ga is used to maintain the electro-conductive bond between the Ag electrode printed on the actuator and the steel substrate, allowing for stress free thermal expansion between different members of the assembly. Presently, no published work has been found describing the use of liquid Ga for the purposes of assembling the ultrasonic air transducer, which is developed by Cambridge Joining Technology Limited, pending International Patent (PCT) application.

Since the steel/BIT bond only concerns the faceplate areas of the transducer (acoustic emitter face), faceplates were designed as interchangeable parts of the transducer assembly. Initially, two transducer faceplates were fabricated. Small faceplate (X1) was fabricated to evaluate the electrical properties of the assembly and to verify the condition of the Ga after the high temperature tests. A large faceplate (X2) was fabricated for electrical evaluation, but also to assess the acoustic performance when mounted inside a prototype transducer.

In both cases, a modified BIT actuator, having a diameter of 11 mm and a thickness of 0.5 mm, was furnished with Ag electrodes. The diameter of the electrodes was 10 mm and they were printed on both sides of the actuator.

For construction of the first sample (X1), a small amount of gallium was deposited into the middle of the stainless steel (SS316L) disk. The BIT actuator was then placed on top of the Ga pool, squeezing out the excess to the edges so it could be removed. A ‘belleville’ style mild steel washer was then used to clamp the BIT actuator in place, as shown in Figure 6-10, and was subsequently spot welded to the substrate. Figure 6-10 shows the schematic diagram of the X1 sample assembly.

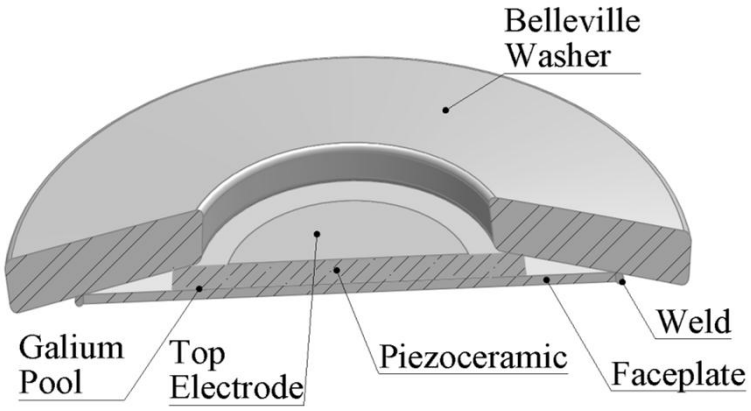

Figure 6-10 Diagram showing the cross section of the X1 faceplate assembly. The faceplate, which is made out of stainless steel 316L and the piezo-ceramic element, sandwiching the gallium pool and the silver electrode. A mild steel belleville washer welded to the substrate holds the assembly together under compression, with the hole in the washer exposing the top electrode.

A second sample (X2) was also fabricated as shown in Figure 6-11. A semi-shear circular recess was formed in the centre of a 200 μm thick stainless steel disk. A small amount of Ga was deposited in the bottom of the recess and the BIT actuator was then placed on top of it. A flexible washer was then spot welded to the stainless steel faceplate in such a way that the top electrode was left exposed. The depth of the semi-shear was slightly less than the thickness of the actuator, so that the actuator was held under slight compression.

For qualitative comparison, a third sample was also evaluated in the form of a plain BIT actuator, as used in the fabrication of the X1 and X2 samples, but without any steel envelope.

During electrical characterisation, both samples were mounted on an electronically controlled hotplate, having a temperature range up to 450°C. Absolute impedance and capacitance were measured at a fixed frequency of 10 kHz, using the Thurlby Thandar LCR400 precision LCR bridge, from room temperature up to 400 °C. Temperature was monitored using a k-type thermocouple and a Digitron thermometer (2000 series).

Samples were placed on top of the hot plate with the actuator electrode exposed and accessible from the top. The analyser probe was mounted in a vertical position with one tip in contact with the actuator electrode and the other in contact with the steel envelope. For the actuator-only test, a small amount of silver wire was placed under the actuator in order to make a reliable electrical contact with the bottom electrode.
The thermocouple was placed next to the sample and the assembly was covered with a small amount of high temperature insulation.

The temperature was increased from 50 °C through to 400 °C in 50 °C increments, allowing 30 minutes stabilisation temperature at each data point. The measurements of the selected parameters were taken manually.

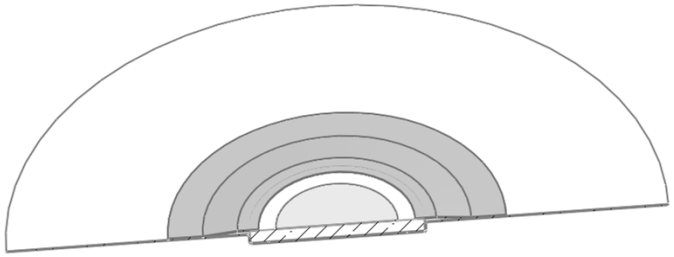

(a)

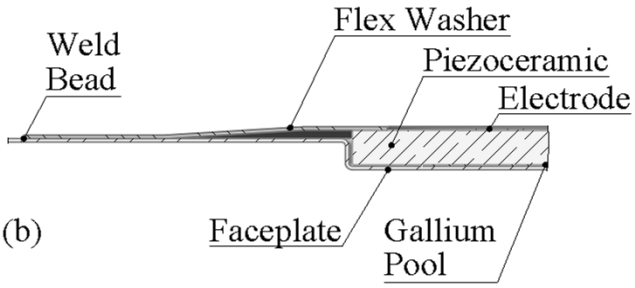

(b)

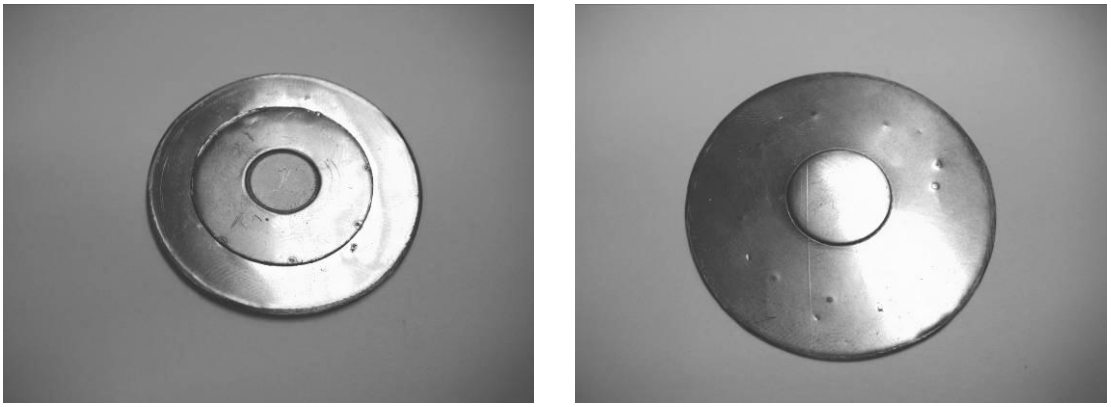

(c)

Figure 6-11 Diagram identifying individual X2 faceplate assembly components, (a and b), and the fabricated prototype (c). The construction is lighter than X1 and there is a better control over containment of gallium. The gap below the flex washer is filled with fine alumina powder to ensure no gallium leaves the pool.

6.3.2.2. Results and Discussion

The qualitative comparison of the X1 and X2 faceplate performance against the BIT actuator pellet, BITA, of the same geometry as used in the construction of the faceplate, was conducted using the same procedure as described previously. Figure 6-12 shows the capacitance and impedance data for the piezoelectric actuator (C_a, $|Z_a|$), and for the X1 (C_b, $|Z_b|$) and X2 (C_c, $|Z_c|$) samples plotted against various temperatures.

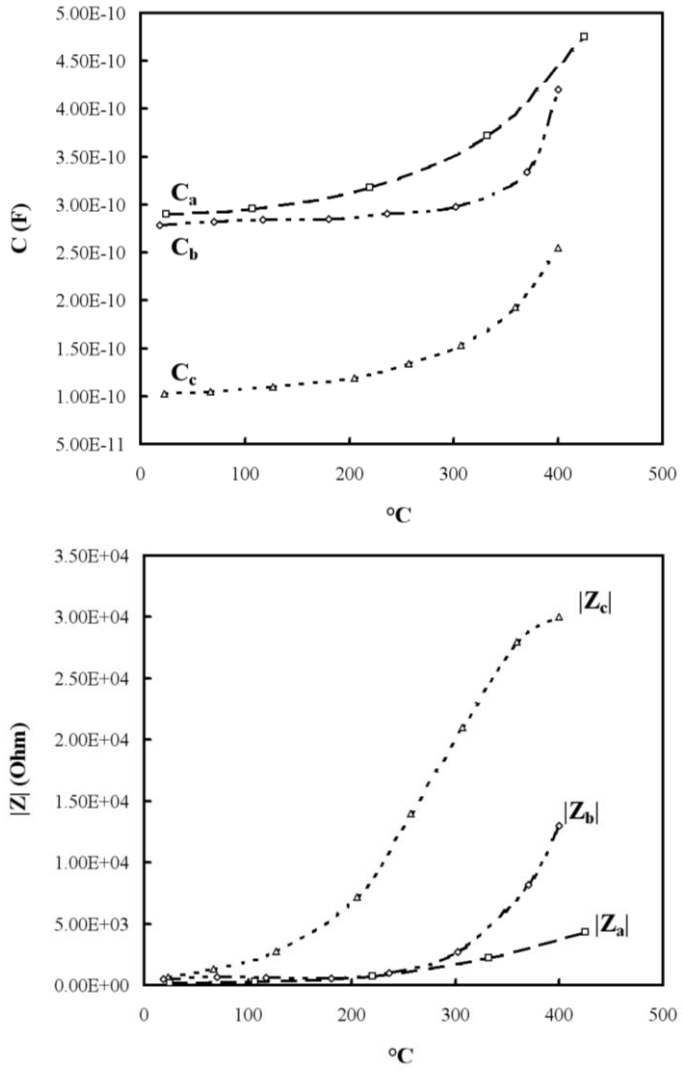

Figure 6-12 Capacitance (above) and impedance (below) plots for the piezoelectric actuator (C_a, $|Z_a|$), and for the X1 (C_b, $|Z_b|$) and X2 (C_c, $|Z_c|$) samples at different temperatures.

The capacitance of a parallel plate capacitor is given by

$$C = \varepsilon_r \times \varepsilon_o \frac{A}{d} \qquad \text{Eq. 6-3}$$

where ε_r is the dielectric permittivity of the material, ε_o is the dielectric permittivity of a vacuum (8.854×10^{-12}), A is the overlapping surface area of the electrode and d is the electrode spacing. The room temperature static capacitance of the BIT actuator prior to fitting into faceplates was measured as 248 pF giving ε_r according to Eq. 6-3 of 178.31. This is in agreement with dielectric measurements made on 8BITNTS previously. Figure 6-13 shows permittivity data for all three samples at 10 kHz for varying temperatures up to 400 °C.

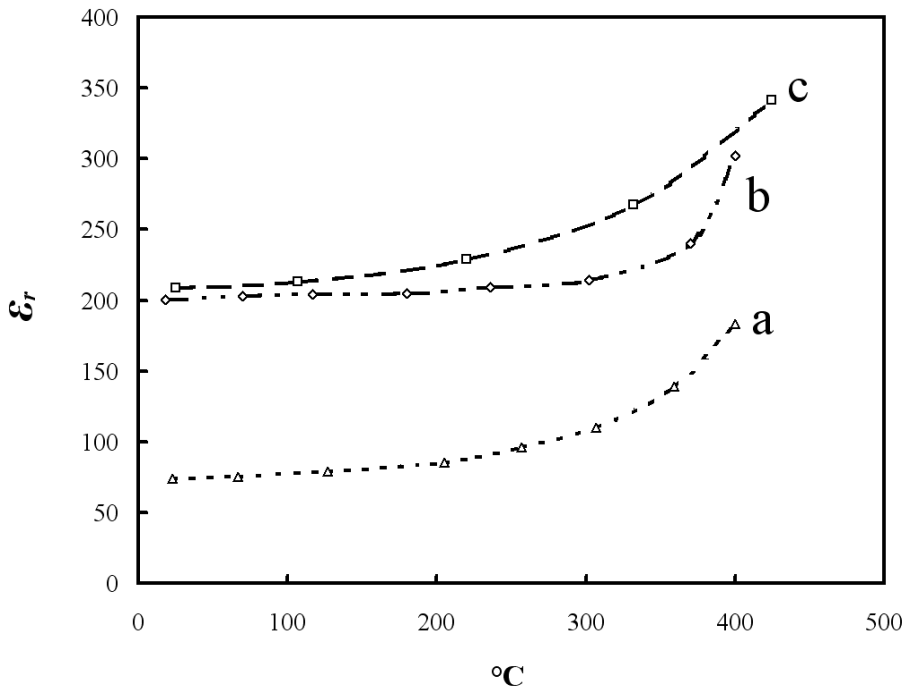

Figure 6-13 Characteristic permittivity of X2 (a), X1 (b) and BITA (c) samples measured at 10 kHz and at various temperatures up to 400 °C

It is noted that both capacitance and permittivity for all three samples increase with temperature, and the traces suggest that the values have not peaked at 400 °C.

Interestingly the X1 sample is comparable in value to the BITA sample, although X1 has a relatively flat response up to 300 °C with a strong increase evident above this point. The sharp increase in permittivity above this temperature can be attributed to oxidisation of the mild steel washer which was observed through changes in its appearance at temperatures > 300 °C. Reasonable agreement below 300 °C with the BITA suggests good consistency in electrode adhesion and only a mild influence of the faceplate envelope in reducing permittivity and capacitance, possibly due to a reduction in gaps between two conductive poles of the device.

Another possible cause of a change in the properties of the X1 sample is the evident loss of Ga from the assembly at higher temperatures, which was leaking out at the interface between the stainless steel base and the mild steel washer. Figure 6-14 shows the X1 sample after the experiment with released Ga on the hotplate.

Figure 6-14 Image showing traces of gallium leaked from the test assembly during electrical tests on a hotplate. Ga first appeared at just above 120°C. The image also shows the very dark appearance of the mild steel washer, indicating a heavy, non-conductive oxide layer

Subsequent disassembly and examination of the X1 sample has shown that even with the substantial Ga losses during the experiment, a significant quantity of Ga was still available, and able to maintain an adequate conductive path between the substrate and the washer.

As could be expected with the washer in its oxidised state, the conductivity of the X1 sample also decreases, albeit in a manner less pronounced than in the case of capacitance and permittivity.

Peritectic transformation between Ag and Ga is another possible cause of the reduction in conductivity, due to formation of solid phase at the interface between the Ag electrode and the liquid Ga. The phase diagram by Baren [154] is shown in Figure 6-15, which indicates that the Ag electrode will dissolve in Ga and structural transformation is suggested by the author at 300 °C. Examination of the electrode after the experiment did not produce conclusive indication of the change in electrode thickness. One way to reduce the effects of Peritectic transformation is to load the liquid Ga with fine grain silver powder.

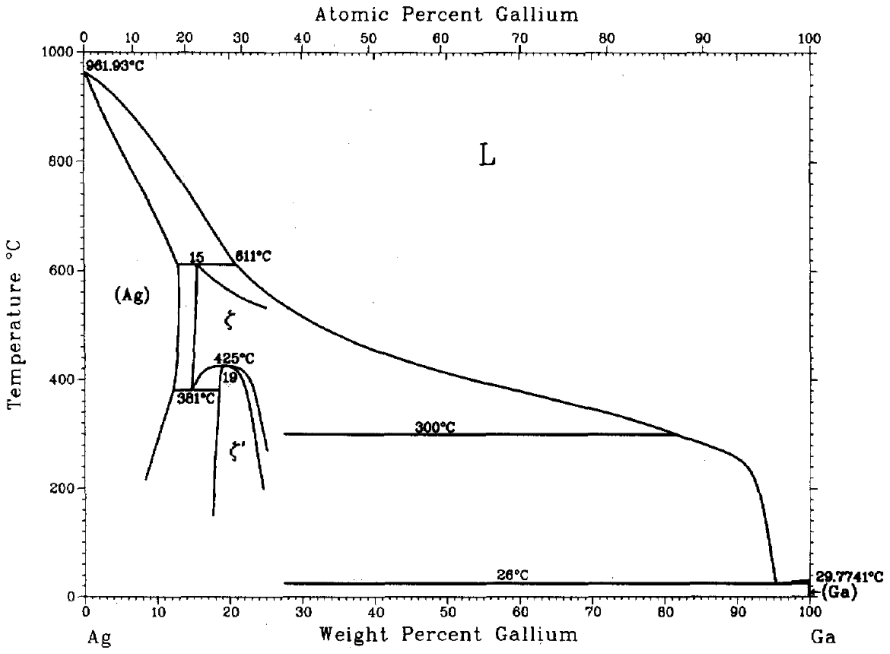

Figure 6-15 Ag - Ga phase diagram **[154]**

The Ga leakage was addressed in the X2 sample and no loss of gallium was observed during any of the tests. The X2 sample exhibited properties which were distinctly different from those for the BITA and X1 samples. The lower capacitance reflects the changes in the assembly and the narrower gaps between two poles of the device. The impedance is shown to increase significantly more than other samples and there is an indication that the response was flattening above 400 °C.

6.3.3. Acoustic Properties of the X2 Faceplate

In order to evaluate the acoustic properties of the high temperature transducer, an experimental setup was constructed as shown in Figure 6-16. The excitation signal is provided by the TG4001 function generator (Thurlby Thandar Instruments), with a sinusoidal output of up to 20 V (peak to peak), connected directly to the transducer. To reduce the effects of interference from ambient, the transducer was fitted into one end of a plastic tube about 300 mm long. At the other end of the tube, a Bruel and Kjaer microphone and an amplifier (4939 and 2670 respectively) were positioned perpendicular to the faceplate of the transducer. This microphone was chosen due to its relatively flat frequency response from 4 Hz up to 100 kHz. The microphone required 200 Vdc polarisation voltage and a suitable power supply was constructed for this function. The output from the amplifier was fed directly to the TDS2024 digital oscilloscope (Tektronix) and the signal could be analysed in the time domain or in frequency domain using FFT function of the instrument.

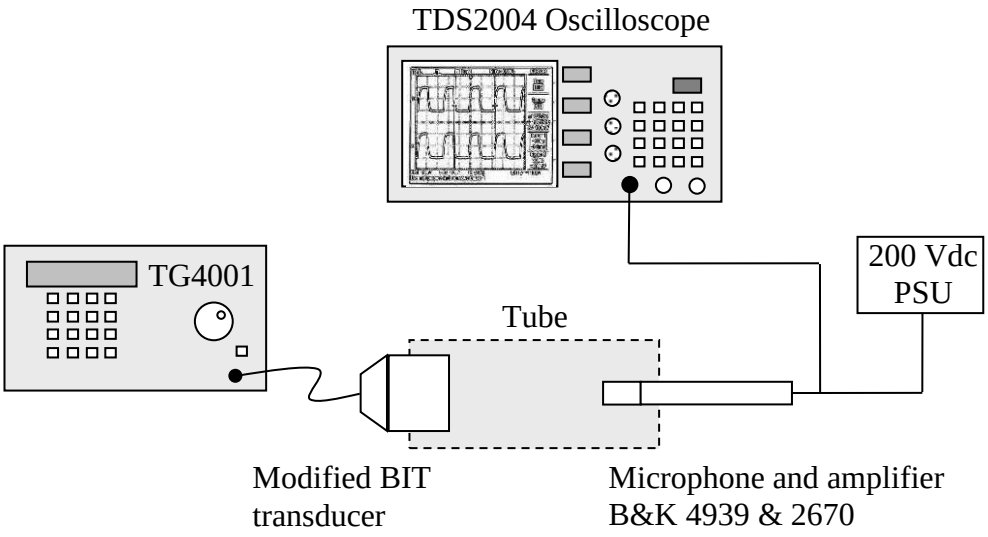

Figure 6-16 Experimental setup for the evaluation of the high temperature ultrasonic transducer and its acoustic response

The X2 sample was mounted into a specially designed transducer body as shown in Figure 6-17. For room temperature tests, the connection between the actuator and the BNC socket was made by soldering fine wire to the Ag electrode and the central pin of the socket.

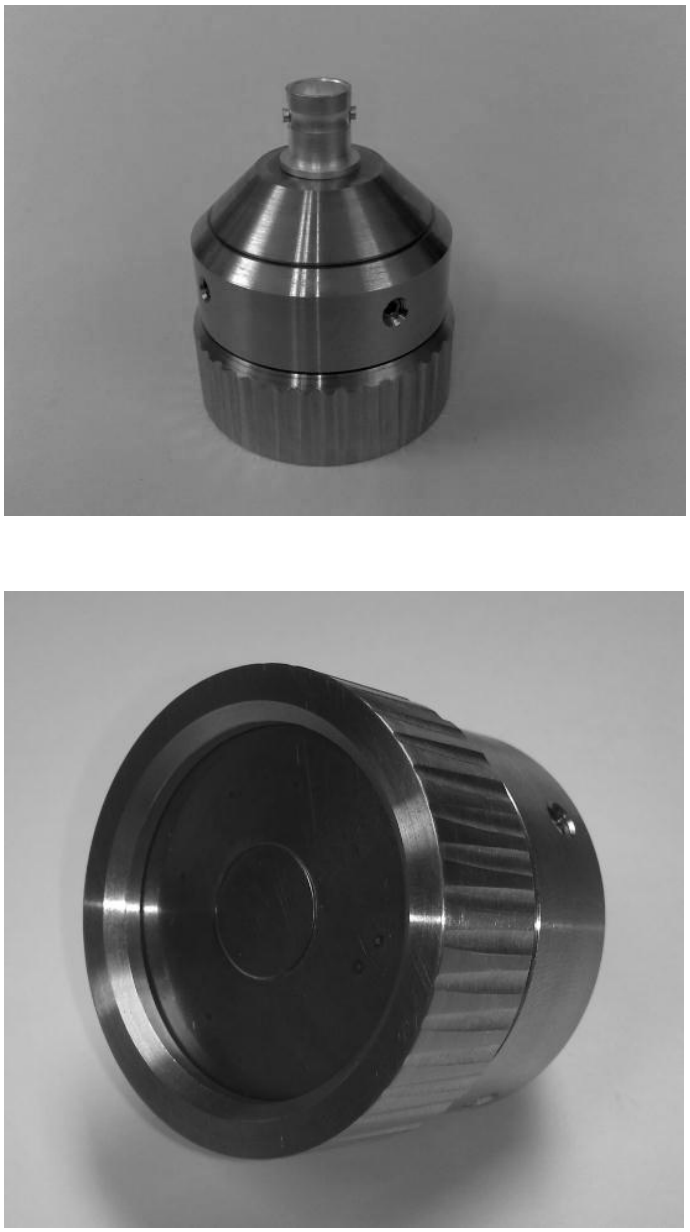

Figure 6-17 Prototype transducer body designed to accept the X2 sample faceplate. It is manufactured out of SS316L and the BNC connector is used as an interface to the excitation and receiver electronics.

This experimental setup allows for evaluation of the transmitting sound pressure level (SPL) from the transducer.

During the final stages of the transducer assembly procedure, shown in Figure 6-18, the faceplate assembly was damaged in that the soldered wire connection was detached from the surface of the actuator removing a large proportion of the electrode itself. Due to the welded construction of the faceplate, it was not possible to recover this assembly and due to time constraints, it was not practical to fabricate another faceplate assembly.

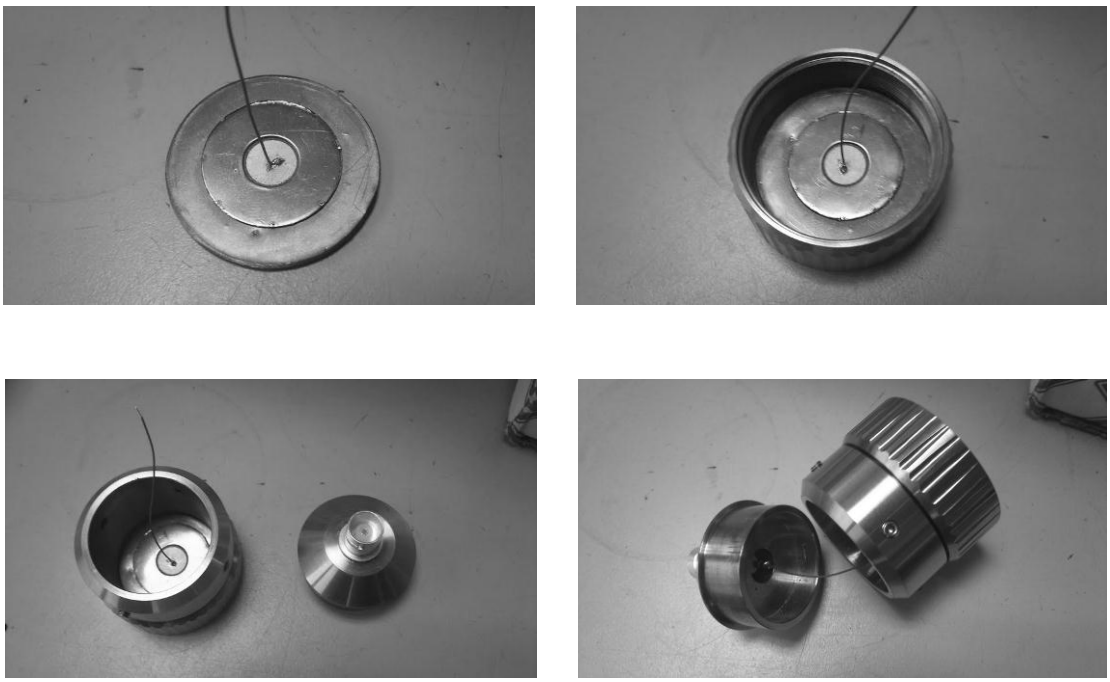

Figure 6-18 Transducer assembly process showing the fine wire soldered to the piezoelectric actuator.

This highlights the mechanical fragility of the electrical interface between the piezoelectric actuator and the outside world. One possible improvement would be to use a spring-loaded contact crimped to the BNC connector

Chapter 7 Conclusion and Further Work

7.1. Conclusion

The present work has resulted in development of enhanced bismuth titanate piezoelectric material suitable for use in high temperature ultrasound transducer applications for measurement of gas velocity. Incremental improvements in piezoelectric properties, depicted in Figure 7-1, were achieved through multi-doping, resulting in best piezoelectric coefficient of 35 pC N^{-1}, which is the highest reported value for a bismuth titanate compound.

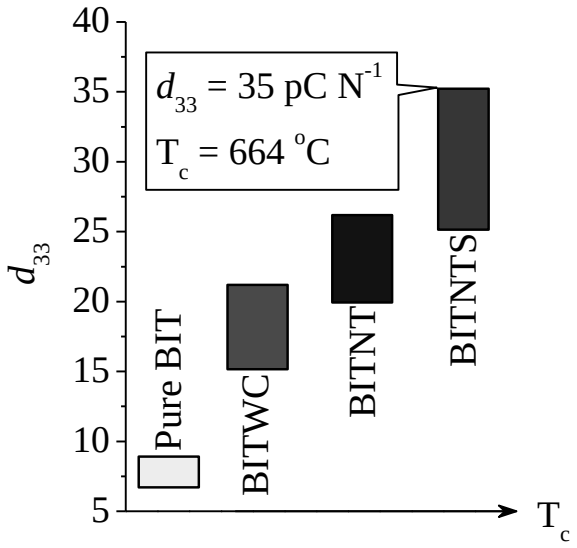

Figure 7-1 Evolution of modified bismuth titanate d_{33} properties under different doping regimes.

In line with the objectives of present work prototype concepts for fabrication of a high temperature ultrasound transducer have been discussed and evaluated. Areas of contamination, acoustic impedance and assembly methods have been addressed in present work.

7.1.1. BITWC

Pure bismuth titanate was doped with tungsten at the titanium site and 0.2 wt% of chromium was added to form $Bi_4Ti_{2.975}W_{0.025}O_{12.025}$ + 0.2 wt% Cr_2O_3 composition. Grain morphology was investigated using SEM and it was found that chromium added in small concentrations acts as a grain growth inhibitor. Phase study using XRD confirmed BLSF like lattice structure conforming to $Bi_4Ti_3O_{12}$ patterns and that smaller ionic size of tungsten at the titanium site caused structural defects at $x < 0.1$ and formed secondary phases at $x >= 0.1$ dopant concentration.

Assessment of AC conductivity has shown that there is a significant reduction in value for $x = 0.025$ composition, which contributed to significantly improved polarisation conditions and in turn producing high d_{33} value of 22 pC N^{-1}. Dielectric loss and permittivity are also decreased for this composition accompanied with a moderate reduction in Curie temperature at 658 °C.

7.1.2. BITNT

Further improvements in piezoelectric properties of BIT were sought through donor co-doping with niobium and tantalum, which have previously been shown to reduce conductivity in pure bismuth titanate and improve poling conditions.

$Bi_4Ti_{2.98}Nb_{0.01}Ta_{0.01}O_{12.0.01}$ (BITNT1) ceramic was produced using conventional mixed oxide sintering method. XRD investigation confirmed that Nb/Ta doped composition did not form secondary phases and surface morphology studied using SEM has shown that increasing dopant concentration reduces the grain growth in BITNT.

AC conductivity has been shown to be comparable with that BITWC and the effect of Nb/Ta concentration is to control p-type to n-type transition. High d_{33} value of 26 is achieved for BITNT1 composition accompanied with a slight reduction in Curie temperature to 670 °C.

7.1.3. BITNTS

The B-site substituted $Bi_4Ti_{2.98}Nb_{0.01}Ta_{0.002}Sb_{0.008}O_{12.002}$ ceramics were synthesized via the conventional mixed oxide reaction route and the high value of the piezoelectric coefficient is found to be 35 pC N^{-1} for 8BTNTS ceramics at room temperature.
The incorporation of antimony into the BITNT ceramic has been shown to reduce the ionic and electronic conductivity and make a significant contribution on enhanced microstructure of the BITNTS ceramic. XRD study has shown that green powder calcinated at 800 °C for 4 hours is consistent with the general bismuth titanate layered structure and no secondary phases were noted.

Morphology study using SEM indicates strong grain growth for 8BITNTS composition, which is put down to formation of liquid $Bi_{12}TiO_{20}$ phase at lower calcination temperatures, which delays formation of primary phase and hence promotes grain growth.
The increase in Sb concentration is accompanied with a decrease in Curie temperature reaching 664 °C for 8BITNTS and a d_{33} value of 35 pC N^{-1}. The significant increase in piezoelectric coefficient is attributed to reduced conductivity and hence improved poling conditions. Thermal annealing properties of 8BITNTS have shown that the material is stable up to 500 °C, demonstrating its suitability for high temperature sensor applications described in present work.

7.1.4. Contamination Effects in High Temperature Gas Flow Applications

Complex impedance studies on commercial, PZT based transducer have shown that the dynamic properties of such device are significantly affected by the agglomeration of solid particles on its surfaces. The resulting shift in resonant frequency where two or more transducers are used is a threat to successful product deployment and it is shown that for efficient, narrow band devices allowable tolerance is relatively small at around 3 to 5 %. This suggests that the use of broad band transducers is more appropriate and the experimentally determined compromise would have to be reached for the final design.

Further study into contamination mechanism using aluminium oxide combined with typical flow conditions in an industrial stack have highlighted that the emitting face of the transducer exhibits certain self-cleaning properties due to vibration and the compression wave being emitted periodically. Taking into account the findings from contamination studies, a prototype transducer was then developed, having extremely rigid body and a replaceable faceplate.

7.1.5. High Temperature Conductive Bonding

Brazing filler based on Ti, Cu and Ag have shown that titanium readily reacts with bismuth titanate ceramic during brazing reducing the surface area of the electrode and increasing the porosity at the interface between the steel substrate and the bismuth titanate ceramic. It is also shown that necessary high ramp rates and the induction heating method used during the brazing experiment do not give an even temperature distribution through the sample, resulting in strong and uniform bond in the centre but porous interface on the outside edges of the sample.

A novel assembly method using liquid gallium to maintain high conductivity path between Ag electrode on the piezoelectric actuator and the stainless steel substrate throughout the temperature range has been evaluated. It is shown that by placing Ga at the interface between piezoceramic and the steel substrate, and keeping the assembly under compression can make a reliable transducer for high temperature applications.

7.2. Further Work

Present work, which is part of an industrial case PhD project, has addressed a number of areas where materials science can make a significant contribution to successful development of a high temperature ultrasonic transducer for gas velocity measurement in industrial smoke stacks. Recognising the contribution that this technology would make to environmental compliance applications, the EPSRC PhD Plus funding has been awarded to further present research and implement a working

high temperature ultrasound transducer. Following areas of research are identified for possible further investigation.

1. Spark Plasma Sintering

Further optimisation in properties of modified bismuth titanate could be achieved through pressure assisted sintering such as spark plasma sintering or SPS. Increased densities and controlled grain growth would be expected to contribute to the increase in piezoelectric coefficient whilst maintaining the high Curie temperature. Grain texturing is another technique successfully performed on SPS equipment to achieve very high piezoelectric properties theoretically producing $d_{33} > 100$ pC N^{-1}.

This work will be done in collaboration with Queen Mary University London and Prof. M. Reece and his team.

2. Prototype transducer characterisation

Acoustic impedance characterisation of the prototype transducer fitted with an X2 style faceplate is the key to confirm the suitability of the transducer for use in high temperature gas velocity applications.

Initially, the qualitative assessments against commercial, PZT based devices at room temperature, followed by high temperature laboratory and field trials. Resonance shift with temperature is an important property that needs to be analysed in the future.

Safe excitation voltages that will not cause premature de-polarisation need to be defined and proved in the field.

3. Metallic foam brazing

Present research has shown that strong bonds between piezoelectric ceramic and stainless steel with good resilience to thermal cycling can be achieved. Further investigation could be carried out to further investigate alternative heating methods and brazing fillers to produce a more consistent and reliable bond suitable for present application. Sample heating using mainly conduction, rather than radiation mechanism could produce more even heating and better controlled reaction.

Present research has also identified that bismuth titanate family of materials exhibits important photocatalytic properties, which were investigated and published in present work but not considered as part of this PhD. However, this has opened up further avenues of research.

References

1. Down, R.D. and J.H. Lehr, eds. *Environmental Instrumentation and Ananlysis Handbook*. 2004, John Wiley and Sons Inc.: Hoboken, New Jersey.

2. Act of Parliament, *Clean Air Act 1993*. 1993, London: HMSO: London.

3. *Product Selection Page*. [Website] 2011 [cited 2011 08th of March]; Available from: http://www.pcme.com/.

4. Wade, G., *Human uses of ultrasound: ancient and modern.* Ultrasonics, 2000. **38**(1-8): p. 1-5.

5. Lindsay, R.B., *The Story of Acoustics.* The Journal of the Acoustical Society of America, 1966. **39**(4): p. 629-644.

6. Kalmus, H.P., *APPARATUS FOR MEASURING FLOW*, U.S.P. Office, Editor. 1955: United States of America.

7. Blocher, O.G., *APPARATUS FOR MEASUREMENT OF FLUID FLOW*, U.S.P. Office, Editor. 1955: United States of America.

8. Kritz, J., *ELECTROACOUSTIC FLOWMETER*, U.S.P. Office, Editor. 1959: United States of America.

9. Lynnworth, L.C. and Y. Liu, *Ultrasonic flowmeters: Half-century progress report, 1955-2005.* Ultrasonics, 2006. **44**(Supplement 1): p. e1371-e1378.

10. Miller, R.W., *Flow Measurement Engineering Handbook.* 3 ed. 1996, Boston: McGraw Hill.

11. Baker, R.C., *Flow Measurement Handbook.* 2000, Cambridge: Cambridge University Press.

12. Hawksley, P.G.W., S. Badzioch, and J.H. Blackett, *Measurement of Solids in Flue Gases*. 2 ed. 1977, London: The Institute of Fuel.

13. Lipták, B.G., *Flow Measurement*. 1993, Radnor: Chilton Book Company.

14. Spitzglass, J.M., *Pitot Tube*, U.S.P. Office, Editor. 1917: USA.

15. Guowei, L., M. Qianmin, X. Dailiang, L. Changwu, and W. Fang. *Development of the Multi-point Thermal Gas-mass Flowmeter*. in *Instrumentation and Measurement Technology Conference, 2006. IMTC 2006. Proceedings of the IEEE*. 2006.

16. Yoder, J. (2004) *Gas Measurement Trends*. Flow Control.

17. Yoder, J. (2008) *The Ultrasonic Boom*.

18. Yamamoto, M. and K. Ito, *Ultrasonic Flowmeter System*, U.S.P. Office, Editor. 1966, Keiki Seizosho Company: USA.

19. Lynnworth, L.C. and E.P. Papadakis, *Ultrasonic Measurements for Process Control: Theory, Techniques, Applications.* The Journal of the Acoustical Society of America, 1990. **88**(1): p. 589-589.

20. Carson, P.L. and R. Banjavic, *The evaluation and calibration of ultrasonic transducers. Edited by M. G. Silk, Surrey, England, IPC Science and Technology Press Ltd, 1978, 200 pages, $41.60.* Journal of Clinical Ultrasound, 1980. **8**(5): p. A21.

21. Kocis, S. and Z. Figura, *Ultrasonic Measurements and Technologies*. 1996, London: Chapman & Hall.

22. Ao, X.S., J. Matson, P. Kucmas, O. Khrakovsky, and X.S. Li (NA) *UR-268; Ultrasonic Clamp-On Flow Measurement of Natural Gas, Steam and Compressed Air*.

23. Matson, J., C.F. Mariano, O. Khrakovski, and L. Lynnworth (2002) *Ultrasonic Mass Flowmeters Using Clamp-On or Wetted Transducers*.

24. Lynnworth, L.C., *Ultrasonic Measurements for Process Control: Theory, Techniques, Applications*. 1989, San Diego: Academic Press Inc.

25. McNab, A., K.J. Kirk, and A. Cochran, *Ultrasonic transducers for high temperature applications.* Science, Measurement and Technology, IEE Proceedings -, 1998. **145**(5): p. 229-236.

26. Kobayashi, M., C.K. Jen, J.F. Bussiere, and K.T. Wu, *High-temperature integrated and flexible ultrasonic transducers for nondestructive testing.* NDT & E International, 2009. **42**(2): p. 157-161.

27. Butler, B., S.B. Palmer, and G.J. Primavesi, *Techniques for the generation of ultrasound for extended periods at high temperatures.* Ultrasonics, 1979. **17**(6): p. 249-254.

28. R. Kazis, A. Voleisis, and B. Voleisiene, *High Temperature Ultrasonic Transducers: Review.* Ultragarsas, 2008. **63**(2).

29. Turner, R.C., P.A. Fuierer, R.E. Newnham, and T.R. Shrout, *Materials for high temperature acoustic and vibration sensors: A review.* Applied Acoustics, 1994. **41**(4): p. 299-324.

30. Tokarev, E.F., G.S. Pado, V.I. Ivannikov, I.A. Dan'kov, G.S. Kudryashov, and F.S. Khattamov, *High-temperature acoustic receivers for the temperature range 20–500°c.* Measurement Techniques, 1992. **35**(4): p. 499-501.

31. Jen, C.K., J.G. Legoux, and L. Parent, *Experimental evaluation of clad metallic buffer rods for high temperature ultrasonic measurements.* NDT & E International, 2000. **33**(3): p. 145-153.

32. Lynnworth, L.C., *Ultrasonic Transducer for High Temperature Applications*, U.S.P. Office, Editor. 1988, Panametric Inc.: USA.

33. Muto, K. and Y. Atsuta, *Applications of Brazed-Type Ultrasonic Probes for High and Low Temperature uses.* Nondestructive Testing and Evaluation, 1992. **7**(1): p. 263 - 272.

34. Shirzadi, A.A., Y. Zhu, and H.K.D.H. Bhadeshia, *Joining ceramics to metals using metallic foam.* Materials Science and Engineering: A, 2008. **496**(1-2): p. 501-506.

35. Krause, J.T., *Gold-Indium Bond for Measurement of Ultrasonic Properties in Solids at High Temperatures.* Journal of Applied Physics, 1968. **39**(11): p. 5334-5335.

36. Asher, R.C., *Ultrasonic Sensors for Chemical and Process Plant*. Sensors, ed. B.E. Jones. 1997, London: IOP Publishing Ltd.

37. Blitz, J., *Ultrasonic: Methods and Applications*. 1971, London: Butterworth & Co (Publishers) Ltd.

38. Jaffe, B., W.R. Cook, and H. Jaffe, *Piezoelectric Ceramics*. 1971, Marietta, Ohio: CBLS Publisher.

39. Ristic, V.M., *Principles of Acoustic Devices*. 1983, Toronto: John Wiley & Sons.

40. Desilets, C.S., J.D. Fraser, and G.S. Kino, *The Design of Efficient Broad-Band Piezoelectric Transducers.* Sonics and Ultrasonics, IEEE Transactions on, 1978. **25**(3): p. 115-125.

41. Silk, M.G., *Ultrasonic Transducers for Nondestructive Testing*. 1984, Bristol: Adam Hilger Ltd.

42. Lynnworth, L.C., D.R. Patch, and W.C. Mellish, *Impedance-Matched Metallurgically Sealed Transducers.* Sonics and Ultrasonics, IEEE Transactions on, 1984. **31**(2): p. 101-104.

43. Papadakis, E.P., *Nonuniform Pressure Device for Bonding Thin Slabs to Substrates.* The Journal of Adhesion, 1972. **3**(3): p. 181 - 194.

44. Technologies, P. *Piezo Technologies Material Specification Sheet*. 2010 07.02.2010]; Available from: http://www.piezotechnologies.com/materialssheet.htm.

45. Pampuch, R., *Ceramic Materials: an introduction to their properties*. 1976, Amsterdam: Elsevier Scientific Pub. Co.

46. Megaw, H.D., *Ferroelectricity in Crystals*. 1957, London: Methuen & Co Ltd.

47. Caddy, W.G., *Piezoelectricity*. 1st ed. 1946, New York: McGraw-Hill Book Company Inc.

48. Moseley, P.T. and A.J. Crocker, *Sensor Materials*. 1996: CRC Press.

49. Burfoot, J.C., *Ferroelectrics*. 1967, London: D. Van Nostrand Company Ltd.

50. Herbert, J.M., *Ferroelectric Transducers and Sensors*. Vol. 3. 1982, London: Gordon and Breach Science Publishers Ltd.

51. Hammond, C., *The Basics of Crystallography and Diffraction*. 1997, Oxford: Oxford University Press.

52. Moulson, A.J. and J.M. Herbert, *Electroceramics*. 2 ed. 2003, Chichester: John Wiley & Sons Ltd.

53. Valasek, J., *Piezoelectric and Allied Phenomena in Rochelle salt.* Physical Review, 1921. **17**(4): p. 475.

54. Henderson, I.R., *Piezoelectric Ceramics; Principles and Applications*. 2002, Mackeyville, USA: APC International, Ltd.

55. Randeraat, J.V. and R.E. Setterington, *Piezoelectric Ceramic*. 1968, London: Mullard Limited.

56. Rödel, J., W. Jo, K.T.P. Seifert, E.M. Anton, T. Granzow, and D. Damjanovic, *Perspective on the Development of Lead-free Piezoceramics.* Journal of the American Ceramic Society, 2009. **92**(6): p. 1153-1177.

57. Maeder, M.D., D. Damjanovic, and N. Setter, *Lead Free Piezoelectric Materials.* Journal of Electroceramics, 2004. **13**(1): p. 385-392.

58. Yan, H., H. Ning, Y. Kan, P. Wang, and M.J. Reece, *Piezoelectric Ceramics with Super-High Curie Points.* Journal of the American Ceramic Society, 2009. **92**(10): p. 2270-2275.

59. Zhang, X., H. Yan, and M.J. Reece, *Effect of A Site Substitution on the Properties of $CaBi_2Nb_2O_9$ Ferroelectric Ceramics.* Journal of the American Ceramic Society, 2008. **91**(9): p. 2928-2932.

60. Zhou, C.-R. and X.-Y. Liu, *Piezoelectric properties and dielectric behavior of Bi1/2Na1/2[Ti1− x (Sb1/2Nb1/2) x]O3 lead-free piezoelectric ceramics.* Journal of Electroceramics, 2007. **19**(2): p. 237-240.

61. Yang, Z., R. Zhang, L. Yang, and Y. Chang, *Effects of Cr2O3 doping on the electrical properties and the temperature stabilities of PNW-PMN-PZT ceramics.* Materials Research Bulletin, 2007. **42**(12): p. 2156-2162.

62. Zeng, T., H. Yan, H. Ning, J. Zeng, and M.J. Reece, *Piezoelectric and Ferroelectric Properties of Bismuth Tungstate Ceramics Fabricated by Spark Plasma Sintering.* Journal of the American Ceramic Society, 2009. **92**(12): p. 3108-3110.

63. Wang, K., B.-P. Zhang, J.-F. Li, and L.-M. Zhang, *Lead-free Na0.5K0.5NbO3 piezoelectric ceramics fabricated by spark plasma sintering: Annealing effect on electrical properties.* Journal of Electroceramics, 2008. **21**(1): p. 251-254.

64. Stojanovic, B.D., C.O. Paiva-Santos, M. Cilense, C. Jovalekic, and Z.Z. Lazarevic, *Structure study of Bi4Ti3O12 produced via mechanochemically assisted synthesis.* Materials Research Bulletin, 2008. **43**(7): p. 1743-1753.

65. Takenaka, T. and K. Sakata, *Grain Orienteation and Electrical Properties of Hot-Forged $Bi_4Ti_3O_{12}$ Ceramic.* Japanese Journal of Applied Physics, 1980. **19**(1): p. 31-39.

66. Kimura, T., T. Yoshimoto, N. Lida, Y. Fujita, and T. Yamaguchi, *Mechanism of Grain Orienteation During Hot-Pressing of Bismuth Titanate.* Journal of American Ceramic Society, 1989. **72**(1): p. 85-89.

67. Patwardhan, J.S. and M.N. Rahaman, *Compositional effects on densification and microstructural evolution of bismuth titanate.* Journal of Materials Science, 2004. **39**(1): p. 133-139.

68. Yan, H., M.J. Reece, J. Liu, Z. Shen, Y. Kan, and P. Wang, *Effect of texture on dielectric properties and thermal depoling of Bi[sub 4]Ti[sub 3]O[sub 12] ferroelectric ceramics.* Journal of Applied Physics, 2006. **100**(7): p. 076103-3.

69. M.H. Sim, J.M.X., J. Wang, *Layer Structured calcium bismuth titanate by mechanical activation.* Materials Letters, 2004(58): p. 2032-2036.

70. Yan, H., H. Zhang, R. Ubic, M.J. Reece, J. Liu, Z. Shen, and Z. Zhang, *A Lead-Free High-Curie-Point Ferroelectric Ceramic, CaBi2Nb2O9.* Advanced Materials, 2005(17): p. 1261-1265.

71. Xu, Y., *Ferroelectric Materials and Their Applications*. 1991, Amsterdam: North-Holland.

72. Shulman, H.S., *Piezoelectric Bismuth Titanate Ceramics for High Temperature Applications*, in *Département des matériaux*. 1997, Ecoles Polytechniques fédérale de Lausanne: Lausanne.

73. Machura, D., J. Rymarczyk, and J. Ilczuk, *Ceramic bismuth titanate for high – temperature electro-acoustic transducers.* The European Physical Journal - Special Topics, 2008. **154**(1): p. 131-134.

74. Shulman, H.S., D. Damjanovic, and N. Setter, *Niobium Doping and Dielectric Anomalies in Bismuth Titanate.* Journal of the American Ceramic Society, 2000. **83**(3): p. 528-532.

75. Hong, S.-H., S. Trolier-McKinstry, and G.L. Messing, *Dielectric and Electromechanical Properties of Textured Niobium-Doped Bismuth Titanate Ceramics.* Journal of the American Ceramic Society, 2000. **83**(1): p. 113-118.

76. Hong, S.H., J.A. Horn, S. Trolier-McKinstry, and G.L. Messing, *Dielectric and ferroelectric properties of Ta-doped bismuth titanate.* Journal of Materials Science Letters, 2000. **19**(18): p. 1661-1664.

77. Villegas, M., A.C. Caballero, C. Moure, P. Durán, and J.F. Fernández, *Factors Affecting the Electrical Conductivity of Donor-Doped $Bi_4Ti_3O_{12}$ Piezoelectric Ceramics.* Journal of the American Ceramic Society, 1999. **82**(9): p. 2411-2416.

78. Voisard, C., D. Damjanovic, and N. Setter, *Electrical conductivity of strontium bismuth titanate under controlled oxygen partial pressure.* Journal of the European Ceramic Society, 1999. **19**(6-7): p. 1251-1254.

79. Goldschmidt, V.M., *Die Gesetze der Krystallochemie.* Naturwissenschaften, 1926. **14**(21): p. 477-485.

80. William D. Callister, J., *Material Science and Engineering, An Introduction*. 3rd ed. 1994: John Whiley and Sons, Inc.

81. Aurivillius, B., *Mixed bismuth oxides with layer lattices, II. Structure of Bi4Ti3O12.* Arkiv foer Kemi, 1950(1): p. 499-512.

82. Subbarao, E.C., *Ferroelectricity in Bi4Ti3O12and Its Solid Solutions.* Physical Review, 1961. **122**(3): p. 804.

83. Subbarao, E.C., *A family of ferroelectric bismuth compounds.* Journal of Physics and Chemistry of Solids, 1962. **23**(6): p. 665-676.

84. Jardiel, T., A. Caballero Cuesta, and M. Villegas, *Aurivillius ceramics: Bi4Ti3O12-based piezoelectrics.* Journal of the Ceramic Society of Japan, 2008. **116**(4): p. 511-518.

85. Dorrian, J.F., R.E. Newnham, D.K. Smith, and M.I. Kay, *Crystal structure of $B_4Ti_3O_{12}$.* Ferroelectrics, 1971. **3**(1): p. 17 - 27.

86. Newnham, R.E., R.W. Wolfe, and J.F. Dorrian, *Structural basis of ferroelectricity in the bismuth titanate family.* Materials Research Bulletin, 1971. **6**(10): p. 1029-1039.

87. Rae, A.D., J.G. Thompson, R.L. Withers, and A.C. Willis, *Structure Refinement of Commensurately Modulated Bismuth Titanate, $Bi_4Ti_3O_{12}$.* Acta crystallographica. Section B, 1990. **46**.

88. Bruna, M., *Piezoelectric Ceramic Devices*, in *Department of Materials Science and Metallurgy*. 2004, University of Cambridge: Cambridge.

89. Gautschi, G., *Piezoelectric sensorics: force, strain, pressure, acceleration and acoustic*. 2002, Berlin: Springer-Varlag.

90. Shimazu, M., J. Tanaka, K. Muramatsu, and M. Tsukioka, *Phase transition in the family LaxBi4-xTi3O12: In relation to lattice symmetry and distortion.* Journal of Solid State Chemistry, 1980. **35**(3): p. 402-406.

91. Shulman, H.S., M. Testorf, D. Damjanovic, and N. Setter, *Microstructure, Electrical Conductivity, and Piezoelectric Properties of Bismuth Titanate.* Journal of the American Ceramic Society, 1996. **79**(12): p. 3124-3128.

92. Villegas, M., T. Jardiel, and G. Farías, *Sintering and electrical properties of Bi4Ti2.95WxO11.9+3x piezoelectric ceramics.* Journal of the European Ceramic Society, 2004. **24**(6): p. 1025-1029.

93. Zhang, L., R. Chu, S. Zhao, G. Li, and Q. Yin, *Microstructure and electrical properties of niobium doped Bi4Ti3O12 layer-structured piezoelectric ceramics.* Materials Science and Engineering B, 2005. **116**(1): p. 99-103.

94. Stojanovic, B.D., A.Z. Simoes, C.O. Paiva-Santos, C. Quinelato, E. Longo, and J.A. Varela, *Effect of processing route on the phase formation and properties of Bi4Ti3O12 ceramics.* Ceramics International, 2006(32): p. 707 - 712.

95. Hou, J., R. Kumar, Y. Qu, and D. Krsmanovic, *Controlled synthesis of photoluminescent Bi4Ti3O12 nanoparticles from metal-organic polymeric precursor.* Journal of Nanoparticle Research, 2009.

96. Du, X., Y. Xu, H. Ma, J. Wang, and X. Li, *Synthesis and Characterization of Bismuth Titanate by an Aqueous Sol-Gel Method.* Journal of the American Ceramic Society, 2007. **90**(5): p. 1382-1385.

97. Pookmanee, P., P. Boonphayak, and S. Phanichphant, *Chemical synthesis of bismuth titanate microparticles.* Ceramics International, 2004(30): p. 1917 - 1919.

98. Xiang, P.-H., Y. Kinemuchi, T. Nagaoka, and K. Watari, *Sintering behaviors of bismuth titanate synthesized by a coprecipitation method.* Materials Letters, 2005. **59**(28): p. 3590-3594.

99. Yang, Q., Y. Li, Q. Yin, P. Wang, and Y.B. Cheng, *Bi4Ti3O12 nanoparticles prepared by hydrothermal synthesis.* Journal of the European Ceramic Society, 2003. **23**(1): p. 161 - 166.

100. Speranskaya, E.I., I.S. Rez, L.V. Kozlova, V.M. Skorikov, and V.N. Slavov, *The Bismuth Oxide - Titanium Dioxide System.* Izv. AN SSSR, Noergan. matem., 1965.

101. Bruton, T.M., *Study of the liquidus in the system Bi2O3---TiO2.* Journal of Solid State Chemistry, 1974. **9**(2): p. 173-175.

102. Rahaman, M.N., *Ceramic processing and sintering*. Materials Engineering. 2003, New York: Marcel Dekker.

103. Barsoum, M.W., *Fundamentals of Ceramics*. Series in Material Science and Engineering, ed. B. Cantor and M.J. Goringe. 2003, London: IOP Publishing Ltd.

104. Holdsworth, M.R., *METHOD OF MANUFACTURING HOT PRESSED CERAMIC MATERIAL BASED ON SILICON NITRIDE*. 1973, Joseph Lucas (Industries) Limited: United States of America.

105. Kan, Y., P. Wang, T. Xu, G. Zhang, D. Yan, Z. Shen, and Y.B. Cheng, *Spark Plasma Sintering of Bismuth Titanate Ceramics.* Journal of the American Ceramic Society, 2005. **88**(6): p. 1631-1633.

106. Orrù, R., R. Licheri, A.M. Locci, A. Cincotti, and G. Cao, *Consolidation/synthesis of materials by electric current activated/assisted sintering.* Materials Science and Engineering: R: Reports, 2009. **63**(4-6): p. 127-287.

107. Rochow, T.G. and P.A. Tucker, *Introduction to Microscopy by Light, Electrons, X Rays, or Acoustics*. 2nd ed. 1994, New York: Plenum Press.

108. (2008) *TA Thermal Analysis Brochure*.

109. Singer, F. and S.S. Singer, *Industrial Ceramics*. 1963, London: Chapman and Hall.

110. Vlack, L.H.v., *Physical Ceramics for Engineers*. 1964, Reading, MA: Addison-Wesley.

111. German, R.M., *Sintering theory and practice*. 1996, New York: Wiley.

112. Skoog, D.A., D.M. West, and F.J. Holler, *Fundamentals of Analytical Chemistry*. 7th ed. 1996, Forth Worth: Saunders College Publishing.

113. *IEEE Standard on Piezoelectricity.* ANSI/IEEE Std 176-1987, 1988: p. 0_1.

114. *IEEE Standard Definitions and Methods of Measurement for Piezoelectric Vibrators.* IEEE Std No.177, 1966: p. 1.

115. Erhart, J. and L. Burianová, *What is really measured on a d33-meter?* Journal of the European Ceramic Society, 2001. **21**(10-11): p. 1413-1415.

116. Bauerle, J.E., *Study of solid electrolyte polarization by a complex admittance method.* Journal of Physics and Chemistry of Solids, 1969. **30**(12): p. 2657-2670.

117. Kao, K.C., *Dielectric phenomena in solids*. 2004, San Diego: Elsevier Academic Press.

118. Takahashi, M., Y. Noguchi, and M. Miyayama, *Electrical conduction properties of La-substituted bismuth titanate single crystals.* Journal of Ceramic Processing Research, 2005. **6**(4).

119. Kim, J.K., T.K. Song, S.S. Kim, and J. Kim, *Ferroelectric properties of tungsten-doped bismuth titanate thin film prepared by sol-gel route.* Materials Letters, 2002. **57**(4): p. 964-968.

120. Takahashi, S., *Effects of impurity doping in lead zirconate-titanate ceramics.* Ferroelectrics, 1982. **41**(1): p. 143 - 156.

121. Smolenskii, G.A., V.A. Bokov, V.A. Isupov, N.N. Krainik, R.E. Pasynkov, and A.I. Sokolov, *Ferroelectrics and Related Materials*. Ferroelectricity and Related Phenomena, ed. G.A. Smolenskii. Vol. 3. 1984, Amsterdam: Gordon and Breach Science Publishers.

122. Angadi, B., P. Victor, V.M. Jali, M.T. Lagare, R. Kumar, and S.B. Krupanidhi, *Ac conductivity studies on the Li irradiated PZT and SBT ferroelectric thin films.* Materials Science and Engineering B, 2003. **100**(1): p. 93-101.

123. Takahashi, M., Y. Noguchi, and M. Miyayama, *Estimation of ionic and hole conductivity in bismuth titanate polycrystals at high temperatures.* Solid State Ionics, 2004. **172**(1-4): p. 325-329.

124. Hou, Y.D., P.X. Lu, M.K. Zhu, X.M. Song, J.L. Tang, B. Wang, and H. Yan, *Effect of Cr2O3 addition on the structure and electrical properties of Pb((Zn1/3Nb2/3)0.20(Zr0.50Ti0.50)0.80)O3 ceramics.* Materials Science and Engineering B, 2005. **116**(1): p. 104-108.

125. Li, J. and Q. Sun, *Effects of Cr2O3 doping on the electrical properties and the temperature stabilities of PZT binary piezoelectric ceramics.* Rare Metals, 2008. **27**(4): p. 362-366.

126. Megriche, A., L. Lebrun, and M. Troccaz, *Materials of Bi4Ti3O12 type for high temperature acoustic piezo-sensors.* Sensors and Actuators A: Physical, 1999. **78**(2-3): p. 88-91.

127. Jardiel, T., M. Villegas, A. Caballero, D. Suvorov, and A.C. Caballero, *Solid-State Compatibility in the System Bi_2O_3-TiO_2-Bi_2WO_6.* Journal of the American Ceramic Society, 2008. **91**(1): p. 278-282.

128. Luo, S., Y. Noguchi, M. Miyayama, and T. Kudo, *Rietveld analysis and dielectric properties of Bi2WO6-Bi4Ti3O12 ferroelectric system.* Materials Research Bulletin, 2001. **36**(3-4): p. 531-540.

129. Takahashi, M., *Space Charge Effect in Lead Zirconate Titanate Ceramics Caused by the Addition of Impurities.* Japanese Journal of Applied Physics, 1970. **9**(10).

130. Coondoo, I., A.K. Jha, and S.K. Agarwal, *Enhancement of dielectric characteristics in donor doped Aurivillius SrBi2Ta2O9 ferroelectric ceramics.* Journal of the European Ceramic Society, 2007. **27**(1): p. 253-260.

131. Takenaka, T. and K. Sakata, *Electrical properties of grain-oriented ferroelectric ceramics in some lanthanum modified layer-structure oxides.* Ferroelectrics, 1981. **38**(1): p. 769 - 772.

132. Kan, Y., X. Jin, G. Zhang, P. Wang, Y.-B. Cheng, and D. Yan, *Lanthanum modified bismuth titanate prepared by a hydrolysis method.* Journal of Materials Chemistry, 2004. **14**.

133. Hyatt, N.C., I.M. Reaney, and K.S. Knight, *Ferroelectric-paraelectric phase transition in the n=2 Aurivillius phase Bi3 Ti1.5 W0.5 O9 : A neutron powder diffraction study.* Physical Review B, 2005. **71**(2): p. 024119.

134. Jonscher, A.K., *The "universal" dielectric response.* Nature, 1977. **267**(5613): p. 673-679.

135. Fouskova, A. and L.E. Cross, *Dielectric Properties of Bismuth Titanate.* Journal of Applied Physics, 1970. **41**(7): p. 2834-2838.

136. Armstrong, R.A. and R.E. Newnham, *Bismuth titanate solid solutions.* Materials Research Bulletin, 1972. **7**(10): p. 1025-1034.

137. Zhao, P., B.-P. Zhang, R. Tu, and T. Goto, *High Piezoelectric d33 Coefficient in Li/Ta/Sb-Codoped Lead-Free (Na,K)NbO3 Ceramics Sintered at Optimal Temperature.* Journal of the American Ceramic Society, 2008. **91**(11): p. 3824-3824.

138. Zhang, Q., B.-P. Zhang, H.-T. Li, and P.-P. Shang, *Effects of Sb content on electrical properties of lead-free piezoelectric [(Na0.535K0.480)0.942Li0.058](Nb1-xSbx)O3 ceramics.* Journal of Alloys and Compounds. **490**(1-2): p. 260-263.

139. Saito, Y., H. Takao, T. Tani, T. Nonoyama, K. Takatori, T. Homma, T. Nagaya, and M. Nakamura, *Lead-free piezoceramics.* Nature, 2004. **432**(7013): p. 84-87.

140. Navarro-Rojero, M.G., J.J. Romero, F. Rubio-Marcos, and J.F. Fernandez, *Intermediate phases formation during the synthesis of Bi4Ti3O12 by solid state reaction.* Ceramics International. **36**(4): p. 1319-1325.

141. Miyazawa, S. and T. Tabata, *Bi2O3-TiO2 binary phase diagram study for TSSG pulling of Bi12TiO20 single crystals.* Journal of Crystal Growth, 1998. **191**(3): p. 512-516.

142. *Thermal evolution of ZnO-Bi2O3-Sb2O3 system in the region of interest for varistors.* Journal of Materials Science, 2006. **41**: p. 2319-2325.

143. Jardiel, T., M.A. De La Rubia, and M. Peiteado, *Control of Functional Microstructure in WO3-Doped Bi4Ti3O12 Ceramics.* Journal of the American Ceramic Society, 2008. **91**(4): p. 1083-1087.

144. Migahed, M.D., M. Ishra, T. Fahmy, and A. Barakat, *Electric modulus and AC conductivity studies in conducting PPy composite films at low temperature.* Journal of Physics and Chemistry of Solids, 2004. **65**(6): p. 1121-1125.

145. Williams, G. and D.C. Watts, *Non-symmetrical dielectric relaxation behaviour arising from a simple empirical decay function.* Transactions of the Faraday Society, 1970. **66**: p. 80-85.

146. Kohlrausch, R., *Theorie des elektrischen Rückstandes in der Leidener Flasche.* Annalen der Physik, 1854. **167**(2): p. 179-214.

147. Ngai, K.L., R.W. Rendell, and H. Jain, *Anomalous isotope-mass effect in lithium borate glasses: Comparison with a unified relaxation model.* Physical Review B, 1984. **30**(4): p. 2133.

148. Vaish, R. and K. Varma, *Dielectric properties of Li2O-3B2O3 glasses.* Journal of Applied Physics, 2009. **106**(6): p. 4106.

149. Vaish, R. and K. Varma, *Low loss and frequency (1 kHz–1 MHz) independent dielectric characteristics of 3BaO–3TiO2B2O3 glasses.* Journal of Applied Physics, 2009. **106**(11): p. 114109.

150. *Equivalent Circuit of Ultrasonic Transducers*, in *Application Note 050913*. 2005, Prowave Electronics Corporation.

151. *Air Ultrasonic Ceramic Transducers 328ET/R250*, in *Datasheet*. 2005, Prowave Electronics Corporation.

152. Gospodinov, M., S. Haussühl, P. Sveshtarov, S. Dobreva, and A. Sampil, *Growth and physical properties of bismuth titanate crystals.* Materials Research Bulletin, 1992. **27**(12): p. 1415-1421.

153. Euroinox, *Stainless Steel: Tables of Technical Properties*, in *Physical Properties of Stainless Steels*. 2005, Euro Inox: Luxemburg.

154. Baren, M., *The Ag-Ga (Silver-Gallium) system.* Journal of Phase Equilibria, 1990. **11**(4): p. 334-339.